UNIVERSITY OF THE
WITWATERSRAND,
JOHANNESBURG

Interfacial Microstructure and Mechanical Properties of WC-Co Oxyacetylene Brazed Joints Using Ag-Based Filler Alloy

Nthape Percyval Mphasha

A dissertation submitted to the Faculty of Engineering and Built Environment, University of the Witwatersrand, Johannesburg, in fulfilment for the degree of Masters of Science in Engineering.

Johannesburg, 2021

DECLARATION

I declare that this dissertation is my own, unaided work. It is being submitted for the Degree of Masters of Science in Engineering in the University of the Witwatersrand, Johannesburg. It has not been submitted before for any degree or examination in any other University.

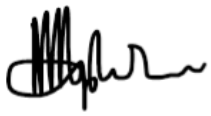

(Signature of candidate)

_19th_ day of _April__ 2021_

ABSTRACT

An attempt was made to understand the brazeability of different WC-Co grades (6 and 10 wt% Co) and the impact of brazing parameters on the mechanical properties of the brazed joint, while considering potential possibilities for using brazing as a refurbishing technology. The influence of surface oxide formation and interfacial microstructural evolution on the brazeability of WC-Co at common interfaces was investigated. Thermal oxidation was carried out in a muffle furnace at different oxidation times in the temperature range 400 - 750°C, in air. Oxidation of the WC-Co samples increased significantly with temperatures above 600°C. At higher oxidation times, mass gain increased with decreasing Co content. As a result of early and increased preferential formation of a protective oxide scale, WC-10wt%Co experienced less surface oxidation than WC-6wt%Co at higher oxidation times. The oxide scales contained mainly the dense $CoWO_4$, mixed with the porous WO_3.

WC-Co samples were oxyacetylene brazed at common interfaces using a B-Ag49CuZnMnNi filler alloy under atmospheric conditions at 710°C for 30 seconds. The braze interlayers, for both 8 and 24 µm thicknesses, consisted mainly of light α-Ag(s.s) and dark α-Cu(s.s) phases. There was no evidence of an interfacial oxide layer formation, instead the diffusion of Co into the interlayer was observed. Increasing the interlayer thickness promoted the formation of Ag-Cu-Zn eutectic phases in the interlayer, in addition to α-Ag(s.s) and dark α-Cu(s.s) phases. Changes in interlayer microstructure indicated the synergistic effect of inter-diffusion and Co content.

Joints with an interlayer thickness of 24 µm achieved higher shear strength than 8 µm joints. Shear strength largely depended on the dispersion strengthening effect of α-Cu(s.s) and Ag-Cu-Zn eutectic phases, which increased with increasing Co content. WC-6wt%Co showed a ductile fracture mode while WC-10wt%Co showed a mixture of ductile and brittle fracture modes.

I dedicate this work to God and my ancestors, without whom all this would not have been possible,

and to

My mother: Mosebudi 'a mmaTshwane Mphasha

Your love and prayers kept me

ACKNOWLEDGEMENTS

First of all, I would like to thank my supervisor, Dr David Whitefield, for giving me the opportunity to learn and contribute to the fascinating world of cemented carbides.

The DST (Department of Science and Technology)/NRF (National Research Foundation), Center of Excellence (CoE) in Strong Materials is acknowledged for their financial support.

I would like to also thank ULTRAMAT SA (Pty) Ltd. and Umicore Marketing Services South Africa (Pty) Ltd. for, respectively, supplying the WC-Co cemented carbide samples and the braze filler alloy used in this research project.

As far as experiments are concerned, I would like to thank the following for their assistance: Workshop staff, Mr Brayner Nelelwani and Dr Nthabiseng Ntholeng of the School of Chemical and Metallurgical Engineering of Wits University; and Prof. Esther Akinlabi of the School of Mechanical Engineering of the University of Johannesburg.

To all my postgraduate colleagues, friends and comrades, and the University staff, thank you for your support and friendship. A special one to Dr Michael Bodunrin, your support and mentorship are greatly appreciated.

Finally, to my siblings: Maropene Mphasha and Pheladi Madimabe and nieces: Moyahabo, Difakwana, Lerato and Kamogelo, thank you for your constant support through this journey.

RESEARCH OUTPUTS

1. N.P Mphasha and D.J Whitefield, The effect of Co content and WC grain size on the thermal oxidation behaviour of WC-Co cemented carbides, 36th Global Conference on Smart Materials and Nanotechnology 2019, (Book of) Abstracts of papers presented at the conference, Journal of Powder Metallurgy & Mining, Vol. 08, Rome, Italy, 18th - 19th November 2019.

2. N.P Mphasha and D.J Whitefield, Interfacial microstructure of WC-6wt%Co torch brazed joints using Ag-based filler alloy, Proceedings of Microscopy Society of Southern Africa (MSSA), Vol. 48, pp. 27, Club Mykonos, Western Cape, South Africa, 1st - 5th December 2019.

.

CONTENTS

LIST OF FIGURES

LIST OF TABLES

1. INTRODUCTION

1.1. Background and motivation

Cemented carbides or hardmetals are powder metallurgy products that consist of carbide (WC) grains embedded in a ductile metallic (Co, Ni and/or Fe) binder matrix. Powder metallurgy processes include mixing, wet milling, drying, pressing and sintering [1]. This allows the potential to vary composition and carbide grain size depending on the application. The WC-Co system is the common type of cemented carbide in industrial applications. The WC phase provides the high hardness and wear resistance while the Co phase provides the toughness and impact strength [2]. WC-Co alloys have extensive use in various engineering applications such as rock drilling, cutting tools and dies for wire drawing because of their excellent combination of mechanical, physical and chemical properties [2, 3]. However, their widespread use has been limited by their high brittleness and high fabrication costs. Measures such as reduction in the starting WC particle size, manipulation of the sintering time and temperature, and alteration of composition may be employed to produce cemented carbides with high performance and long service life [4].

Cobalt has been the preferred binder for WC, due to its low temperature carbide solubility and high wettability with WC [5]. However, the 2015 world minerals statistics provided by the British Geological Survey have ranked tungsten and cobalt eighth and tenth, respectively, as risk elements of economic value [6]. In addition, China and the Democratic Republic of Congo are the leading producers and top reserve holders of tungsten and cobalt, respectively [6]. The main implication of this is that the world could soon be confronted with constrained supply of these minerals given the monopoly around ownership. This would increase the cost of producing these engineering parts. Hence, there is a need to sustainably use the available resources and recover used materials.

Cemented carbides are brittle and show poor resistance to impact and thermal shock [2, 3] hence they are rarely used unsupported. In most applications, WC-Co hardmetals are used as secured inserts which require either mechanical or metallurgical joining method. It is common practice to attach these cemented carbide inserts to a more resilient tool support, which is normally made of steel. Several joining techniques such as mounting, brazing, welding, diffusion and pressure bonding have been used to assemble cemented carbides with steel or other structural alloys [7]. Owing to the widely differing physical and mechanical properties of cemented carbides and steels, the joining of WC-Co to steel is restricted by a series of difficulties. The integrity of the WC-Co/steel joint has thus been of great interest. Defects such as dislocation, cracks and porosities easily occurred in the joints due to the considerable difference in coefficients of linear expansion between the two base metals [7]. Hence, the current study has a particular interest in joining WC-Co cemented carbides at common interfaces with the aim of minimising the occurrence of metallurgical defects.

The evolution of cemented carbide joining methods had milestone significance in the history of development of cemented carbides. Metallurgical bonding is of high technological importance especially in applications where cemented carbide inserts should be permanently secured during operation. Of particular interest has been the study of joining cemented tungsten carbide alloys to steel with various metallurgical processes such as brazing, welding, diffusion bonding and transient liquid-phase bonding. Currently, brazing and diffusion bonding are the preferred methods to join WC-Co cemented carbide and steel due to their simplicity, reliability, perfect adaptability of part size and shape, high joint strength and low cost [7 - 11]. Brazing can thus be used to achieve successful bonding whilst maintaining the economies of scale at a minimum, which is one of the aims of this study.

Factors such as the selection of optimal filler alloy and process parameters (brazing atmosphere, flux, temperature and time) are essential towards achieving the required joint properties. Generally, braze interlayers with good plastic

properties are applied in the joining of dissimilar metals to improve the braze microstructure and decrease the residual stress [10, 11, 12]. Nickel and Ag-based filler alloys are thus recommended to ensure the oxidation and corrosion resistance of brazed joints [13]. Ag-based filler alloys have been reported to result in excellent wettability of WC-Co cemented carbides, and good bonding as the Co is dissolved in the Ag-based filler metals [12, 14, 15]. Jiang et al. [15] successfully bonded WC-Co to carbon steel using Ag-based filler alloy (Ag-16Cu-23Zn-7.5Mn-4.5Ni, wt%) by high-frequency induction brazing. Maximum joint shear strength of 366 MPa was achieved when brazing at 770°C for 30 s. The current study will explore oxyacetylene brazing at a common interface using a similar Ag-based filler alloy.

Whilst there is sufficient research on WC-Co/steel brazing, there is limited data on the characterisation of WC-Co/WC-Co brazed joints and their microstructure-mechanical property relations. Hence, there appears an opportunity to investigate the brazeability of different WC-Co grades at common interfaces. This type of joints present the potential to be used for refurbishment purposes. The high temperatures associated with brazing may result in component oxidation which may negatively affect the lifespan of the joints. Hence, the current study will use slightly lower temperatures than in [15]. The study will also make an attempt at understanding the mechanistic science behind brazing the different WC-Co grades by analysing the microstructural evolution over a range of brazing temperatures and the impact of oxidation on the mechanical properties.

1.2. Aims and objectives of research study

The aim of this work was to develop and monitor the brazeability of different WC-Co alloy grades using oxyacetylene brazing at a common interface while monitoring oxidation behaviour. The aim was achieved through the following objectives:

- To determine the oxidation behaviour of WC-Co cemented carbides with the same WC grain size and different Co binder contents.

- To characterise the brazeability of WC-Co alloys by brazing with Ag-based filler alloy at two interlayer thicknesses.
- To establish the relationship between the interfacial microstructure and mechanical properties of the brazed joints.

1.3. Hypothesis

WC-Co microstructure with high cobalt binder amount can improve the metallurgical bonding through enhanced inter-diffusion of elements and minimal oxidation, resulting in higher shear strength at the brazed joints.

1.4. Overview of study

In this study, the brazeability of different WC-Co cemented carbides was compared on the basis of their Co binder amount through brazing with a Ag-based filler alloy. Heat was applied for a short time to melt the filler alloy with the aim of minimising WC-Co oxidation. An attempt was also made to improve the joint properties by understanding the oxidation phenomena at the brazing temperature. An understanding of the mechanistic science behind brazing was sought in order to solve some of the problems associated with torch brazing of WC-Co alloys. Mechanical properties of the joints such as hardness, and shear strength were studied.

1.5. Structure of dissertation

The dissertation has the following structure. The motivation for this research is presented in this chapter. Chapter 2 reviews studies on the high-temperature properties, and the brazing techniques used to join cemented carbides. Chapter 3 describes the brazing technique and experimental conditions used. In Chapters 4 and 5, the results and the discussions are respectively presented followed by the conclusions of the investigations.

2. LITERATURE REVIEW

2.1. History of sintered WC-Co alloys

The history of cemented carbides began in Germany in the 1920's with the successful production of drawing dies manufactured from tungsten carbide cobalt [3, 16, 17]. The first patent in the field of sintered cemented carbides was only issued in 1923 [16]. Cemented carbides are among the most critical materials in the engineering industry due to their excellent combination of wear resistance, fracture toughness and hardness [17 - 19]. The WC-Co sintered alloys are mainly used for cutting tools, drilling tools and wear parts [3, 20].

2.2. Production of WC-Co sintered alloy

Commercially available cemented carbides are produced using powder metallurgy techniques [3, 16, 17]. The cost effectiveness desired in mass production and complex parts geometry makes this technique attractive. The powder metallurgy technique is relatively quick and wasted material is limited. Powder metallurgy processes used to manufacture WC-Co cemented carbides have three basic steps, i.e., milling and mixing, compaction, and sintering. Figure 2.1 shows a schematic flow diagram of the process used to produce sintered WC-Co cemented carbide alloys [19]. The final product is an alloy of hard and abrasion resistant particles of tungsten carbide cemented in cobalt. Tungsten carbide (WC) powder is produced by mixing tungsten metal and carbon black, which are then carburized at temperatures between 1400 and 2650°C [16, 21]. Cobalt (Co) powder, which forms the binder phase, is mixed/milled with the WC powder. The mixed powders are then pressed and sintered at high temperatures, in the range 1350 - 1650°C, to produce virtually pore-free sintered compacts [16, 22]. During sintering the Co binder phase wets and dissolves some of the WC grains. The dissolution of the WC grains takes place by solid state diffusion [20, 22], and as the temperature

increases these dissolved grains start to re-precipitate on the undissolved WC grains resulting in WC grain growth [19]. Sintering conditions should always be set so as to eliminate porosity without overheating the compact and causing cobalt migration to the surface where it can form a vapour. If the starting powders are of high quality, the compacts may be sintered under vacuum with practically no porosity present after sintering. Porosity adversely affects the final mechanical and physical properties of the sintered alloy [12]. A typical microstructure of a WC-Co sintered alloy is shown in Figure 2.2.

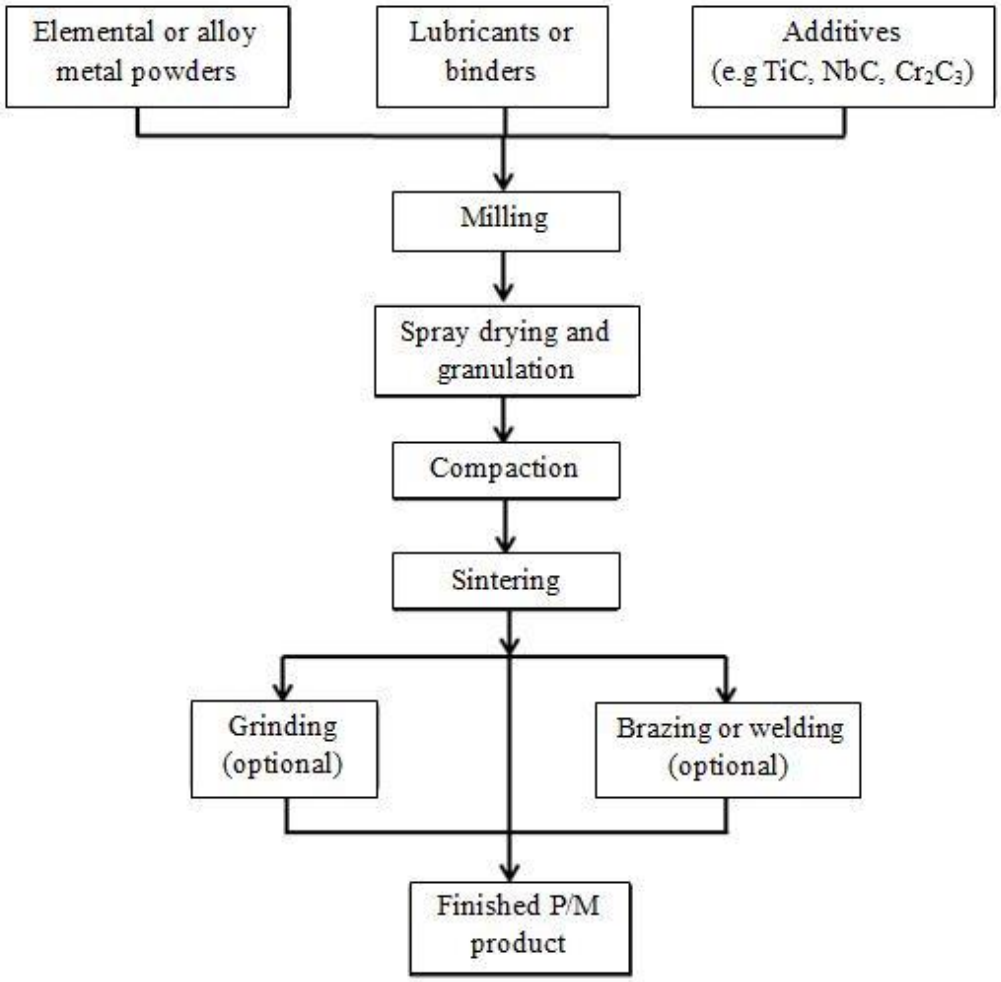

Figure 2.1: Adapted flow diagram of the powder metallurgy production process [19].

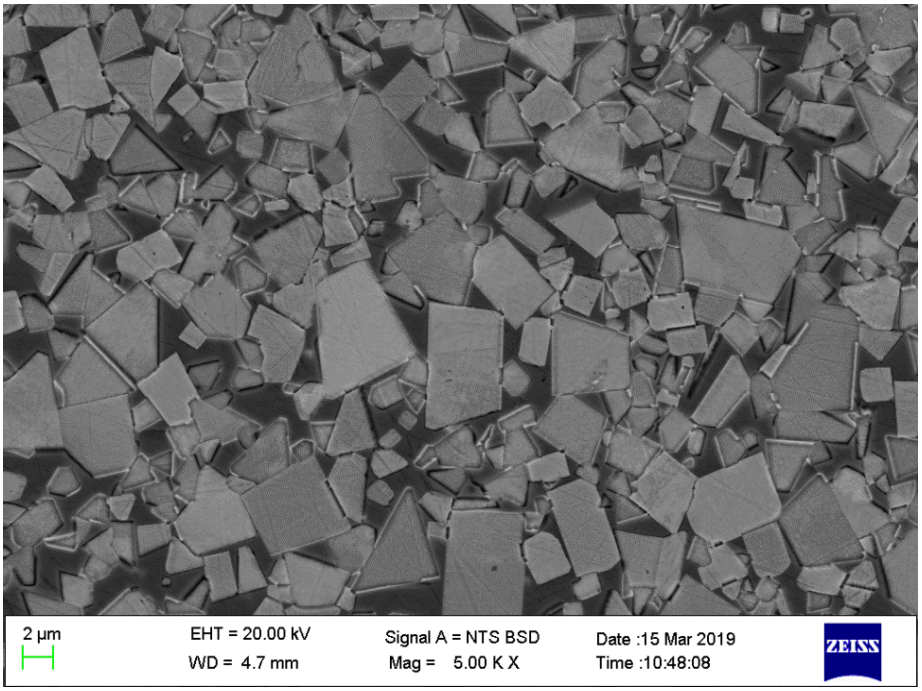

Figure 2.2: Typical microstructure of a WC-Co sintered alloy. The grey angular particles are WC grains and the dark material between the WC grains is Co.

2.3. Properties of sintered WC-Co alloys

The properties of WC-Co sintered alloys depend primarily on the WC grain size, cobalt content and the ability of Co to wet the WC grains [23]. Once an inhomogeneity is incorporated into the manufacturing process it is difficult to rectify in the subsequent processing steps. Hence there is a strict control of raw material quality, milling, and sintering parameters in WC-Co alloy production. According to Luyckx [22], the presence of impurities and trace elements may lead to serious defects in the sintered tungsten carbide alloys. This section summarizes the properties of WC-Co sintered alloys and how they are affected by composition and microstructure.

2.3.1. Hardness

Hardness is defined as the resistance to plastic deformation or resistance to indentation and abrasion [24, 25]. A number of factors affect the hardness of WC-Co sintered alloys. The hardness of WC-Co alloys can be varied from around 800HV to above 2300HV [22, 26], and depends mainly on the WC grain size and the cobalt content. WC grains are the hard phase with a high Young's modulus whilst cobalt is the ductile phase that binds the material together [3, 27]. Figure 2.3 shows the relationship between abrasion resistance and cobalt content of WC-Co alloys with varying WC grain sizes [24]. Abrasion resistance decreases with increasing cobalt content and increases with decreasing WC grain size. The finer the WC grains, the harder the WC-Co alloy. Increasing the cobalt content across all WC grain sizes decreases the hardness of WC-Co alloys [20]. Figure 2.4 shows the relationship between abrasion resistance and hardness of WC-Co alloys with various WC grain sizes [24]. Abrasion resistance increases with increasing hardness.

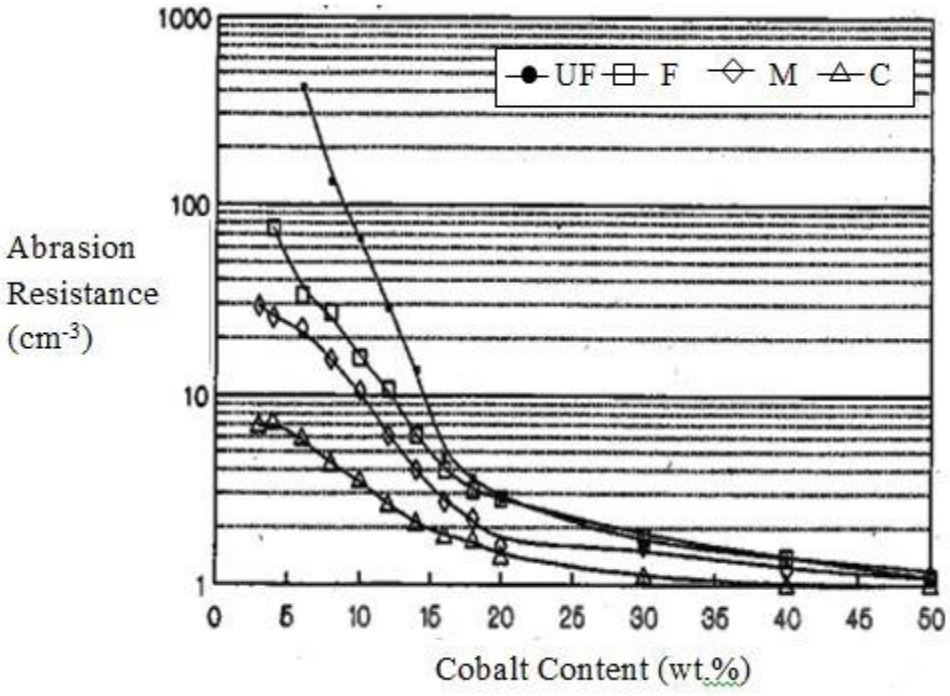

Figure 2.3: The relationship between abrasion resistance and cobalt content of WC-Co alloys with various WC grain sizes. WC grain sizes are designated by UF (0.6μm), F (1.1μm), M (3μm) and C (5.1μm) [24].

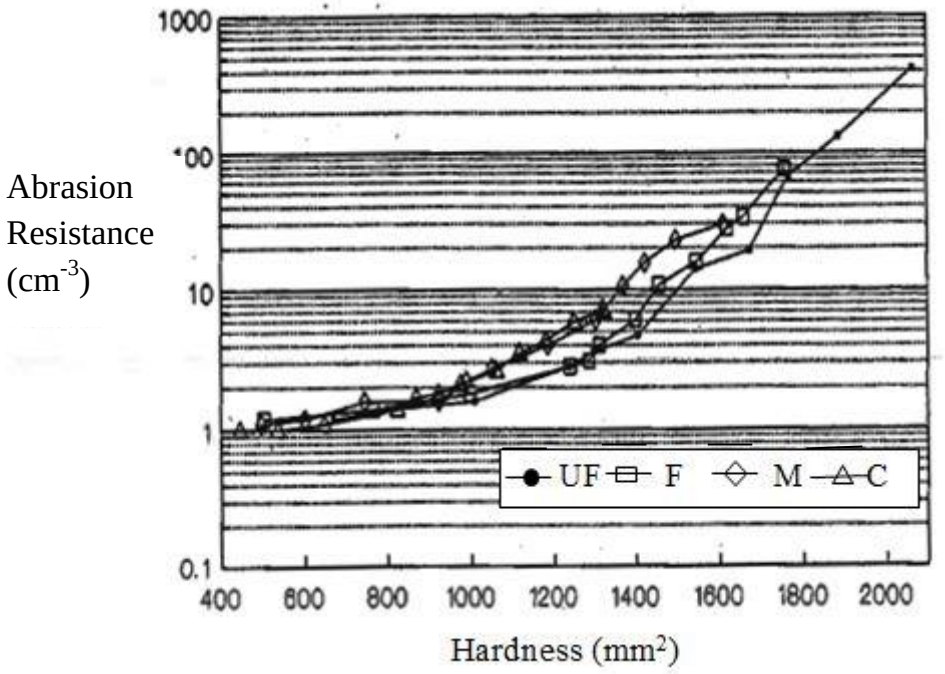

Figure 2.4: The relationship between abrasion resistance and hardness of WC-Co alloys with various WC grain sizes. WC grain sizes are designated by UF (0.6μm), F (1.1μm), M (3μm) and C (5.1μm) [24].

2.3.2. Strength and Toughness

Strength and toughness are important properties of a material which depend on the microstructure. "Strength" is defined as the fracture stress that a material can sustain in bending or tension. Toughness, on the other hand, is defined as the amount of energy absorbed before fracture [27]. The fracture toughness of WC-Co alloys increases with increasing cobalt content and WC grain size [24]. The cobalt binder contributes to the toughness of the sintered WC-Co alloys. The edge strength and toughness of the sintered carbides decrease with increasing levels of residual porosity [28, 29]. Pores may act as crack initiation points and hence adversely affect the performance of the component in application. At high levels of residual porosity, the wear resistance of the sintered carbide may also be adversely affected [29]. Sintered WC-Co alloys generally exhibit transverse rupture strength (TRS) from 1500MPa to 4000MPa and a toughness range from 7MPa to 25MPa [30]. According to Gurland [28], when the tungsten carbide grain

size was constant the transverse rupture strength increases with increasing cobalt content and peaks at a maximum value. This maximum, however, depends on the WC grain size.

2.3.3. Thermal properties

Cemented WC-Co alloys have good thermal conductivity. Thermal properties of WC-Co alloys depend on their composition and microstructure. Increasing the Co content, at constant WC grain size, increases the thermal properties of the alloys given that cobalt is the more significant thermally conductive component [3, 18]. Decreasing the WC grain size increases the surface area for the available cobalt binder and thus increases the thermal properties of W-Co alloys [30]. In general the Co content and WC grain size determine the thermal properties of WC-Co alloys.

Thermal conductivity is a measure of the material's rate of heat conduction [31], and it is influenced by the WC grain size and Co content of WC-Co alloys. Typical thermal conductivity data of WC and Co is shown in Table 2.1. Wang et al. [32] attributed the difference in the thermal conductivity data to sample defects such as porosity and grain boundaries, which decrease the overall thermal conductivity of the material. The variation in the thermal conductivity of cobalt was also ascribed to the highly variable nature of the binder phase composition due to the formation of tungsten and carbon solid solutions. The high thermal conductivity of the cobalt binder phase observed by Gray [33] indicated that lower amounts of tungsten and carbon were alloyed into the cobalt phase. Pierson [34] measured low thermal conductivity of tungsten carbide using practical samples with defects such as porosity and grain boundary, while Schultrich and Poeβnecker [35] presented the thermal conductivity measured from pure tungsten carbide crystals. As a result of the sintering process, the thermal conductivity of the cobalt binder phase in WC-Co cemented carbides in the current study may be taken as 69.00W/mK. However, the current study is not concerned with measuring the thermal conductivity of the cemented carbides. The current study

will explore the influence of WC grain size and cobalt content, which give rise to thermal conductivity, on the thermal oxidation of WC-Co alloys and the solidification mechanism of brazed interlayers.

Table 2.1: Thermal conductivity of cobalt and WC.

Elements or compound	Thermal conductivity (W/mK)
Cobalt [33]	100.00
Cobalt [36]	69.00
Cobalt [37]	69.04
Tungsten carbide [34]	63.00
Tungsten carbide [35]	120.00
Tungsten carbide [38]	84.20

2.3.3.1. WC-Co oxidation

WC-Co cemented carbides are extensively used as tool materials in drilling, machining, and metal forming, amongst other engineering applications. During service, some properties such as wear resistance and toughness may weaken with increasing temperature, especially in oxidising conditions. For example, with an increase in the cutting speed, friction at the tool-chip interface may lead to temperatures in excess of 1200°C [39, 40]. Hence, the effect of thermal oxidation on the brazeability and mechanical properties of WC-Co parts needs to established, in addition to the oxidation experienced when in service. Whilst in most of the below studies, the effect of WC grain size and Co binder content have been examined, limited information is available on the formation of oxides at the brazed joint interlayers. The current study will focus on the possible formation of oxides at the joint interfaces and investigate their influence on working efficiency of the brazed joints.

2.3.3.1.1. Mechanisms of early stage oxidation

The early stage oxidation mechanisms and degradation of mechanical properties are attributed to the high temperatures involved in brazing operation. These high temperatures also lead to thermal shocks given the brazing process. A number of researchers [39, 40, 43, 44] observed a linear-to-paralinear time dependence relationship between weight gain and Co contents ranging from 6wt% to 16wt% when investigating WC-Co cemented carbide oxidation in the temperature range of 400 - 750°C. For example, the weight gain per unit area versus oxidation time for WC-Co hardmetals oxidised at 700°C in air and oxygen, in a gravimetric system is shown in Figure 2.5 [45]. The WC-Co grades followed a linear oxidation trend in both atmospheres. With increasing time, the oxidation rate is slightly lower and this is attributed to the effective reduction in oxide/substrate interface area. Whilst the holding time was longer, the oxidation tests carried out in the current study are expected to mimic the oxidation results in air shown in Figure 2.5.

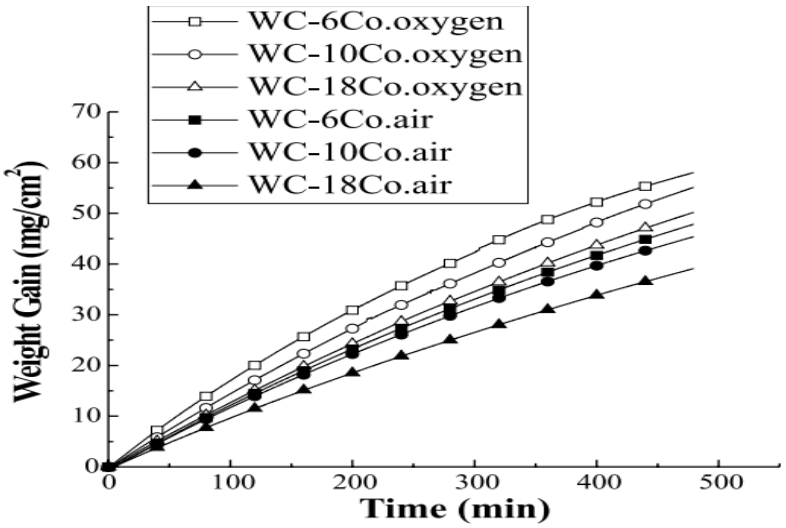

Figure 2.5: Weight gain per unit area versus oxidation time for WC-Co hardmetals oxidised at 700°C in air and oxygen [45].

Figure 2.5 shows that the Co binder content and oxidation rate are inversely proportional. WC-6wt%Co had a higher tendency to oxidise that WC-10wt%Co. This is in complete concordance with the results by Basu and Sarin [42]. The inverse relationship between Co binder content and oxidation rate is attributed to

the higher volume fractions of the dense $CoWO_4$ phase as compared to the pore-containing $CoWO_4$ phase within the oxide layer, with increasing Co content [41]. Hence, there were significant differences in the passivation properties of the oxide layers depending on the Co to carbide ratios, with WC-10wt%Co showing high passivation.

Bhaumik et al. [39] and Lofaj and Kaganovskii [43] studied the oxidation of WC-Co cemented carbide with 6 - 15wt% cobalt in air in the temperature range 650 - 800°C. It was found that WC-Co alloys with high WC content had oxide layers consisting mainly of WO_3 as a result of the oxidation of WC grains. The high WO_3 content in the oxide layers was attributed to the '*shielding effect*' of WC grain on the Co binder phase. This was later confirmed by Chen et al. [45] who categorised the oxidation of WC–Co cemented carbides into three regions, (i) very slight oxidation, (ii) selective oxidation of the Co phase and (iii) simultaneous oxidation of the Co and the WC phases, Figure 2.6. In region (i), the Co phase and the WC phase will be slightly oxidised mainly due to the adsorption of oxygen in the air [45].

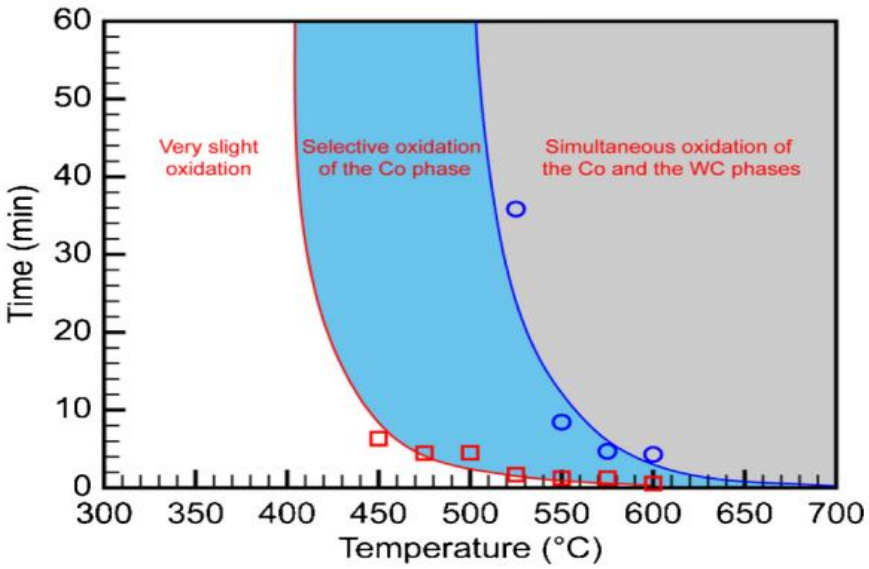

Figure 2.6: The temperature-time diagram of oxidation of WC-Co cemented carbides in air [45].

It was also shown that increasing the Co content, at constant WC grain size, the oxide layers began to be more dense (tightly compact) due to the formation of $CoWO_4$ as a result of Co phase oxidation [39, 42]. The formation of the $CoWO_4$ phase was found to lead to pronounced strength degradation of the WC-Co structure [40, 41, 45, 46]. The $CoWO_4$ phase is highly porous, contains micro-cracks, and had a low adherence to the substrate material. The occurrence of micro-cracks could be attributed to the difference in coefficients of thermal expansion between the oxide layer and the WC-Co substrate. Hence, it can be inferred that the presence of any oxide may deteriorate the quality of the resultant brazed joints, and thus the service life.

2.3.3.2. Effect of oxidation on mechanical properties

Casas et al. [41] investigated the influence of oxidation behaviour of different grades of WC-Co cemented carbides at 700°C on their room-temperature mechanical strength. With an increase in oxidation kinetics due a decrease in Co binder content, the WC-Co composites exhibited a significant strength loss after oxidation, especially at oxidation times between 10 and 60 minutes. This was attributed to the selective oxidation of the Co binder phase in the temperature range 450 - 650°C confirmed by Chen at al. [45]. Selective oxidation of the Co binder resulted in the formation of a highly porous $CoWO_4$ phase which weakened the WC-Co microstructure. Figure 2.6 also shows that decreasing the oxidation time to below 10 minutes at temperatures between with 450°C and 700°C enlarges the selective Co oxidation range. In the current study, oxyacetylene brazing of WC-Co parts will be carried out at 30s holding time in the temperature range 690 - 720°C in order to minimise the occurrence of selective Co oxidation.

Shi et al. [47] studied the oxidation resistance of ultrafine WC-10wt%Co cemented carbide based on nanocomposite powder in the temperature range of 450°C to 700°C, in air. The results showed that the mass gain, as a result of oxide formation, upon oxidation was insignificant from room temperature to 750°C. This showed that increasing the temperature in the range 400 - 750°C at 10

minutes or less minimised the selective oxidation of the Co phase. This was confirmed by the significant decrease in the Vickers hardness and TRS of the specimens decreased with increasing oxidation temperature in excess of 750°C. This was in concordance with the results found by Chen et al. [45]. Hence, it can be expected that the hardness and strength of the WC-Co alloys, especially in the vicinity of the joints, may decrease as a result of temperatures involved in brazing. Upon oxidation, the microstructure of the WC-Co alloys will become loose and porous leading to concerns around the integrity of the brazed joints.

2.4. Joining of WC-Co parts

Novel applications of WC-Co parts, with different specifications, require a combination of materials. This gives rise to the challenge of their assembly. Various joining techniques have been reported to acceptably join cemented carbides together or to join with steel assemblies. In order to acquire sound joints, joining techniques such as brazing [10, 11, 48 - 52], diffusion bonding [48, 49] and transient liquid-phase bonding [50] have been adopted to join WC-Co cemented carbides to steel. Amongst these techniques, brazing has received significant attention due to its simplicity, adaptability to shape and size, good repeatability as well as low operational cost [50, 52]. In order to acquire quality joints, the wettability of the filler alloy (composition of filler alloy and choice of flux) and the method of brazing are considered key factors.

2.4.1. Wettability of the carbide surface

Wetting of the cemented carbide is the primary function of the filler alloy, to form a sound joint. Hence wettability of cemented carbides is recognized as a critical parameter in determining the integrity of the brazed joint. During the brazing process, the filler alloy is heated above its melting point and allowed to flow into the joint by capillary action. The ability of the filler alloy to wet and bond the tungsten carbide is a function of the composition of the cemented tungsten carbide and relates to the cobalt binder content [53, 54]. Hence, it was recommended that

the filler alloy must contain elements which exhibit substantial mutual solubility with the WC-Co cemented carbides, at the brazing temperature. Equation 2.1 shows the theory of wetting of liquids on solid surfaces [55].

$$\gamma_{SV} = \gamma_{SL} + \gamma_{LV} \cos\theta \qquad \textit{Equation 2.1}$$

Where,

γ_{SV} = Solid–vapour surface energy,

γ_{SL} = Solid–liquid surface energy,

γ_{LV} = Liquid–vapour surface energy, and

θ = Contact angle between the edge of a liquid droplet and a solid surface.

Accordingly, good wetting properties of the filler alloys are defined by a contact angle (θ) of less than 90° [56]. An imbalance in surface energies, due to the melting of the filler alloy, would cause the wetting of the filler alloy across the surface of the WC-Co parts. Hence, an increase in γ_{SV} or a decrease in γ_{SL} or γ_{LV} would lead to better wetting characteristics by the filler alloy. Surface-tension forces determine the contact angle for a liquid droplet on a solid surface, as shown in Figure 2.7. Therefore, before cooling and the formation of a solid joint, the molten filler alloy should wet the surfaces of the close-fitting WC-Co parts.

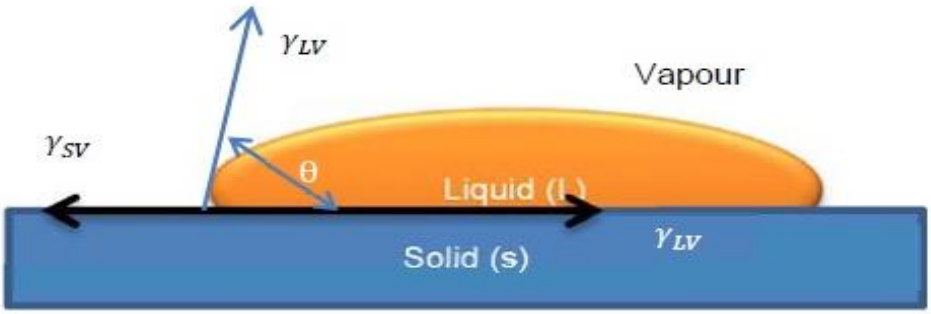

Figure 2.7: Surface-tension forces determine the contact angle (θ) for a liquid droplet on a solid surface [56].

Although brazing is mainly suitable for short-length joints, certain design principles can be developed to suit larger interface joints. Brazing processes such

as vacuum brazing, induction brazing, sintered brazing and flame brazing have been used to successfully braze WC-Co components to steel. Joining of WC-Co to steel by brazing, however, has two main drawbacks, the difficulty of filler alloys to wet cemented carbides and the difference in the coefficient of thermal expansion (CTE). This leads to deterioration in joint quality due to the occurrence of residual thermal stresses at the interfaces [57]. Several studies [53, 58 - 61] have shown that the WC-Co/steel joints failed along the WC-Co/interlayer boundary. Hence, the difference in thermal expansion and the formation of intermetallic phases at the joint interfaces should be minimised in order to achieve a sound brazed joint. The current research was concerned with oxyacetylene brazing WC-Co components together with the aim of minimising the occurrence of residual stresses at the joint interfaces.

2.4.2. Surface preparation for brazing

It is universally agreed that the surface of the metal to be brazed must be free from grease, oils and contaminants in order to obtain the best bond quality. However, no agreement has been reached on the texture of the base metal that will produce optimum wetting and bond strength. In his research, Rhyne [62] stated that cemented carbide surface can be cleaned by grinding or by shot- and sand-blasting. However, it has not been entirely established what effects grinding or shot blasting has on the strength of the brazed joints and any remaining induced residual stresses. Hinnuber and Hilbes [63] ruled out etching as a surface preparation operation as excess cobalt can be leached out from the surfaces of the WC-Co components. This may result in joint strength impairment.

The formation of oxides must also be reduced, and/or oxide formation during heating must be prevented. Hence, it is recommended that brazing should be carried out in an oxygen-free environment, e.g. in an inert gas atmosphere, or under vacuum [49, 57]. It is also important that the approaches for improving the wettability of cemented carbides include the holistic engineering of filler metal composition and the surface preparation to produce effective bonding [64].

2.4.3. Brazing flux

Brazing involves the application of a flux to drive off grease, oils and other contaminants from the metal surfaces to be brazed. The flux consists of a mixture of various metallic salts, and is applied to the joint surfaces as a high-viscosity liquid. During the brazing process, the heat drives off the carrier fluid, often water, before the salts melt and react with the oxides on the joint surfaces. These oxide products are then driven off of the joint interlayer and form an oxide scale on the surface of parent materials [63].

2.4.4. Properties of filler alloy

A number of factors affect the choice of filler alloys. The filler alloy must have high fluidity to permit capillary flow into the gap between the two metal surfaces [63]. To acquire a sound brazed joint, the filler alloy should flow along the grain boundaries of the WC-Co cemented carbide to enhance bonding. Hence the filler alloy must have good adhesion properties to the WC-Co surfaces. The properties of a sound brazed joint can be ascribed to [8]:

- Good penetration of filler alloy along the grain boundaries, and
- Superficial inter-alloying and adhesion between the brazing alloy and the cemented carbide.

The extent of metallurgical reaction and diffusion at the interface was measured by the wettability of the carbide surface. Feduska [65] and Bosch [8] stated that the extent of cemented tungsten carbide wettability defines a sound braze joint. Currently, there are a wide range of braze filler alloys available filling a specialized market, with several different chemical compositions. Of these alloys, the Ag-based braze alloys have receive most attention for the brazing of cemented carbides. Ag-based filler alloys have relatively low melting temperature, high affinity with WC particles, and can offer a uniform composition during the cooling cycle [66]. In addition, Ag-based filler alloys containing nickel (Ni) have been recommended for brazing cemented carbides due to enhanced wetting characteristics and the ability to reduce residual stresses. This was mainly due to

the similarity in physical and chemical properties between Ni and Co [67, 68]. However, the effect of Ni additions on the shear strength of the brazed joints was unclear. It has also been found that manganese (Mn) reacts with the free carbon to produce manganese carbide particles which are subsequently wetted by the molten brazing alloy [69].

2.4.5. Brazing of WC-Co cemented carbide to steel

Brazing appears to be one excellent way of obtaining a sound joint between cemented tungsten carbide and steel parts, and can be performed manually, mechanised or automated [10, 70]. Schröter and Wolff [71] patented the brazing method of producing a cemented carbide/steel joint. Hence, the history of cemented carbide development was driven by the milestone evolution of the cemented carbide joining method. Brazing techniques such as vacuum brazing [72], gas tungsten-arc (GTA) braze welding [73], induction brazing with protective argon [74], and flame brazing with flux [60, 67] can be used successfully braze WC-Co alloys. Table 2.2 summarises of relevant brazing processes and characteristic features of the various types of brazing filler metals. Since the current study is concerned with minimising the occurrence of oxidation in the vicinity of the brazed joints, using the research in section 2.3.3.1, temperatures above 750°C will be disregarded as enhanced oxidation would be experienced.

Table 2.2: Chemical composition of filler alloys and their brazing conditions.

Brazing conditions	**Filler alloy composition**	**Interlayer thickness (mm)**	**Base materials**		**Temperature (**°C)
Vacuum [10]	CuNi	0.1/0.04	WC–8Co	S45C	1050
Induction, flux [13]	AgNi/CuZn /AgNi	0.12	WC-15Co	35CrMo	710-770
GTA braze [58]	AgZnCuNiMn	-	WC-10Co	AISI1020	1300
Vacuum [70]	CuZn	0.2	WC–8Co	3Cr13	1060-1100
Vacuum [71]	AgCu	0.8/2	WC-8Co	SAE1045	1100/850
Vacuum [72]	Ag, AgCu, Cu	0.127	WC-6Co	4340	810-1100
Flame,flux [73]	AgCuP	-	WC	Steel	470-725
Flame,flux [74]	AgCuZnCd	-	W-Co-Ti	AISI4145	710-980
Vacuum [76]	AgZnCuNi	0.3	WC-10Co	90MnCrV8	850

2.4.5.1. Challenges associated with WC-Co/steel brazed joints

Residual stresses remain a major challenge in the brazing of WC-Co to steel [57]. The difference in thermal expansion coefficients of WC-Co and steel leads to inhomogeneous stress states in the components [32]. The finite element numerical simulations conducted by Pintschovius et al. [77] and Zhang et al. [78] indicated that residual stresses in the brazed joints were not uniform and had high values in the matrix near the interface, especially in the cemented carbide side. The induced stresses in the WC-Co can reach critical values, thus leading to premature joint failure on the cemented carbide side during the brazing process, within the cooling phase or even during application [57, 77].

Techniques such as compressing the brazed components, using Ni-based inserts have been recommended to reduce residual stresses in the brazed joints. Zhang et al. [78] reduced the residual stress in the joint from 375 MPa when no compressive pressure was applied to 280 MPa when a compressive pressure of 60 MPa was applied during the cooling process. Lee at al. [10] used a double-layered

Cu alloy and amorphous Ni alloy as insert metal and the oil cooling method, and was able to minimise the residual stress near the bonded zone. Chen at al. [61] developed the study further by using a functionally grade Ni electroplated interlayer to improve wettability and relax residual stresses. The (Cu, Ni)-based solid solution (s.s) which formed between filler alloy and the Ni layer led to enhanced wettability and bonding.

Another challenge which raised concerns around the integrity of WC-Co/steel brazed joints was the formation of brittle Co_3W_3C (η) phases in the joint interlayer. Numerous studies indicated that η phases formed at the interface of the WC-Co/interlayer, leading to cracking and pore formation [10 - 15]. Upon brazing, the brittle η-phases form network-like structures which weaken the joints. Lee et al. [79] recommended the addition of Cr_3C_2 into WC-Co cemented carbides to prevent the formation of η-phase and WC grains grain growth. However, the addition of 1 wt% Cr_3C_2 deteriorated the shear strength due to the formation of brittle Cr_7C_3 in the inserted metal layer. Hence, there appears a gap in knowledge on the brazing of WC-Co cemented carbides with added grain growth inhibitors. The current study seeks to contribute to the body of knowledge by brazing the basic WC-Co system at common interfaces.

2.4.5.2. WC-Co brazing with Ag-based filler alloy

Jiang et al. [15] investigated the properties of induction brazed joints of WC-20wt%Co to carbon steel using Ag-16Cu-23Zn-7.5Mn-4.5Ni (wt%) filler alloys. It was found that, for all brazing temperatures and holding times, island-like α-Cu solid solution (s.s) phases formed in the joint interlayers. Figure 2.8 shows the joints with a thickness of 120 μm obtained at 710°C and 730°C, brazed for 30 seconds. The area and number of island-like α-Cu(s.s) phases decreased with an increase in brazing temperature. It was also found that α-Cu(s.s) phases had a dispersion strengthening effect. Hence, maximum shear strength of 315±6 MPa was achieved for joints brazed at 710°C for 30 seconds.

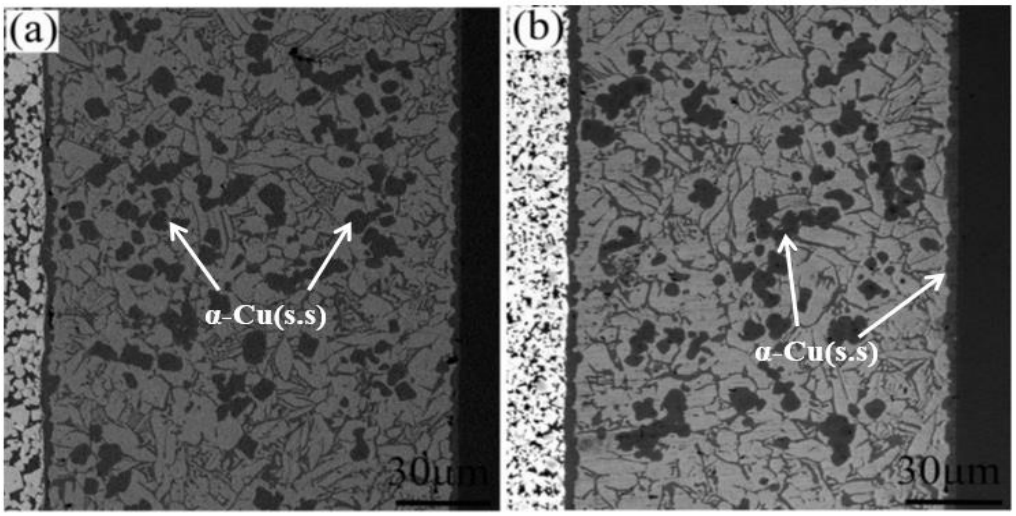

Figure 2.8: SEM-BSD images of induction brazed WC-Co/carbon steel joints for 30s at (a) 710°C and (b) 730°C [15].

Cheniti et al. [58] studied the interfacial microstructural evolution of AISI 1020/WC-10wt%Co brazed joints obtained using Tungsten Inert Gas (TIG) and oxyacetylene processes. The interlayer microstructure consisted of light Ag(s.s) phases, dark Cu(s.s) phases and eutectic phases of Ag-Cu-Zn, at all brazing currents, Figure 2.9. For the 40A current, the Cu(s.s) particles precipitated at the braze/WC-Co interface and throughout the braze interlayer. This became more pronounced with increasing current to 100A. Increasing the brazing current (i.e. increasing the brazing temperature) from 40A to 100A led to the diffusion of large amounts of Ni from the interlayer towards the base materials. This promoted the formation of the island-like Cu(s.s) phases at the interfaces. Figure 2.9d shows that increasing the brazing current also led to WC particle rearrangement at the interface. These results were similar to those found by Jiang et al. [15].

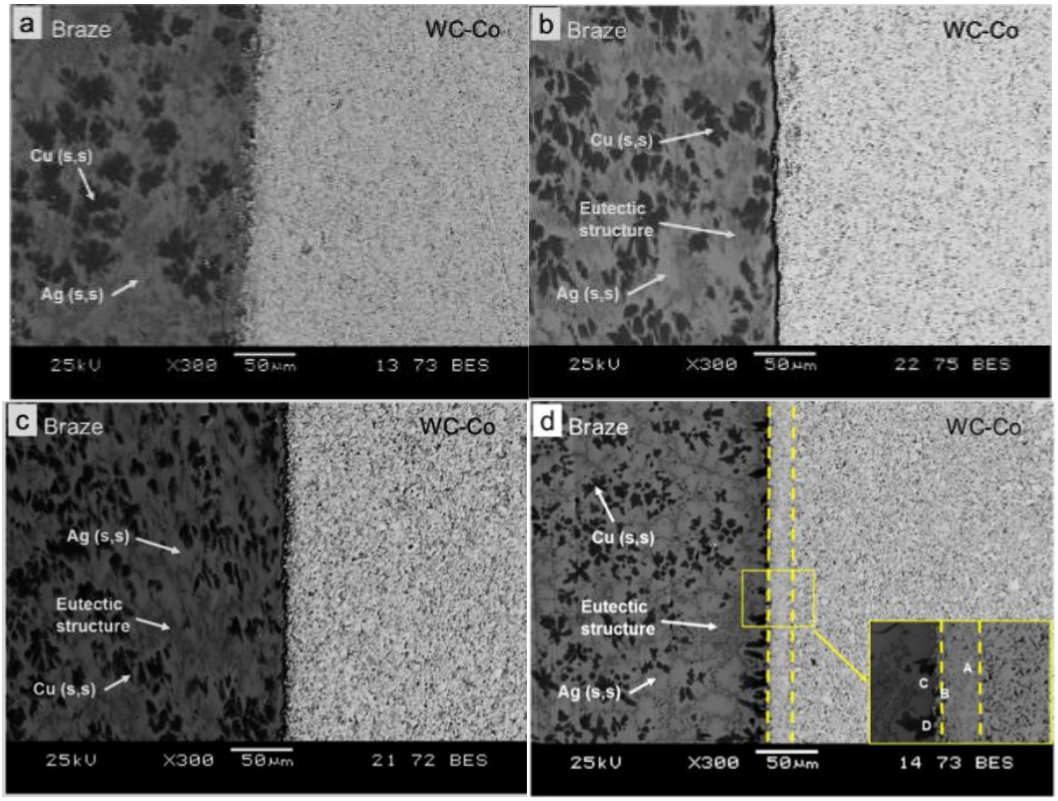

Figure 2.9: SEM micrographs of braze/WC-Co interfaces for the different currents: (a) 40A, (b) 60A, (c) 80A, (d) 100A [58].

Hasanabadi et al. [53] observed similar results when they studied the interfacial microstructure of WC-Co furnace brazed joints in high-purity argon at 730°C. Higher interlayer thicknesses, i.e. 150, 250 and 400µm, were studied at a holding time of 15 minutes. Metallic phases such as Mn_3W_3C formed in the brazed interlayers at brazing times longer than 15 minutes, resulting in decreased shear strength of joints. The current study will use a braze filler alloy with a similar chemical composition to Hasanabadi et al. [53]. Shorter brazing time and lower temperatures will be used to avoid the formation of intermetallic and/or oxide phases in the braze interlayers.

2.4.6. Ag-based filler alloys

Ag-Cu-Zn ternary filler alloys yield high fluidity, high ductility, good adhesion and excellent wetting characteristics, which make them suitable for brazing WC-Co cemented carbides [69, 80]. The ternary phase diagram of the Ag-Cu-Zn filler

alloy shown in Figure 2.10 [81] can be used to predict the phases that would form upon solidification of the interlayer. The highlighted area (red) shows the region in which the filler alloy composition falls into, prior to the addition of manganese and nickel. The compatibility of the Ag-Cu-Zn ternary filler alloys was enhanced by the high silver (Ag) content, which ensures a homogeneous compositional variation in the interlayer. Jia et al. [82] suggested the addition of 20wt% Zn to lower the eutectic temperature of the filler alloy to 675°C. This resulted in the formation of Ag–Cu–Zn eutectic phases. It is also important to note that the addition of nickel in the alloy actually increases the solubility limit of zinc in copper [83]. This will prevent the zinc from forming precipitates which may deteriorate the quality of the brazed joint. In this way, the resulting interlayer would provide the necessary mechanical and physical properties for the joint.

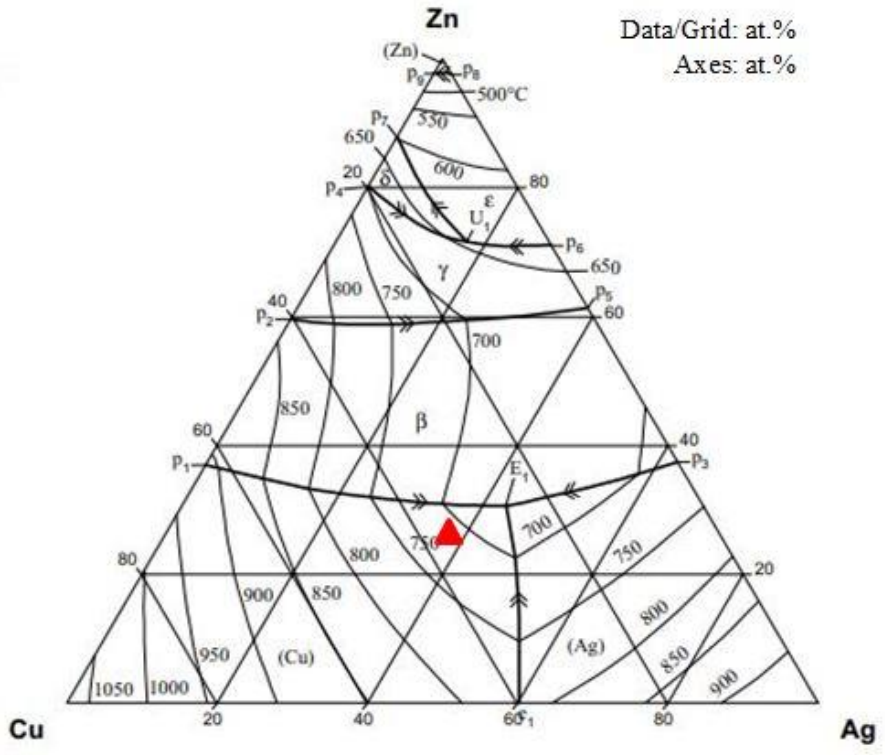

Figure 2.10: Ternary phase diagram showing the liquidus surface of the Ag-Cu-Zn alloying system [81].

2.4.7. Principles of oxyacetylene brazing

Figure 2.11 shows a schematic diagram of the oxyacetylene brazing process [84]. Oxyacetylene brazing uses a torch fed by a mixture of oxygen (O_2) and acetylene (C_2H_2) gases to heat the metal parts to be brazed as well as the braze filler alloy. The filler alloy is then allowed to flow into the gap between the two metal parts and bonds the surfaces by diffusion thus forming a strong joint.

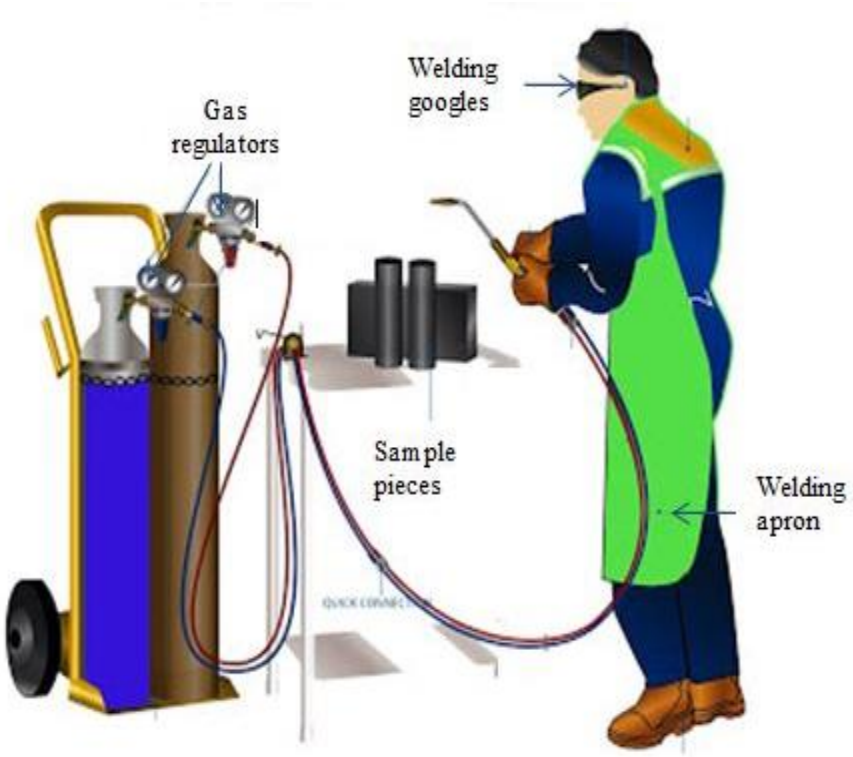

Figure 2.11: Schematic showing the oxyacetylene brazing process [84].

3. EXPERIMENTAL PROCEDURE

The experimental procedures used in this study are described in this chapter. This includes the material characterisation, the experimental procedures, conditions and the equipment used to analyse the as-received, oxidised and brazed cemented carbides.

3.1. Material characterisation

The current study used WC-Co cemented carbides with different Co contents and WC grains sizes. Ultramat (Pty) Ltd. supplied the sintered WC-Co samples. Umicore (Pty) Ltd. supplied the B-Ag49CuZnMnNi (*BrazeTec4900A*) filler alloy used for oxyacetylene brazing. These as-received samples were characterised using Light Optical Microscopy (LOM), Scanning Electron Microscopy (SEM), Vickers hardness tester and a magnetic saturation system.

3.1.1. Vickers hardness

The hardness tests were carried out using a Leco V-100-A2 Vickers hardness tester (±0.5 HV), in accordance with ISO E92-17 [85]. Prior to the hardness measurements, the samples were ground and then polished with a 1µm diamond paste to a mirror-surface finish. Five indentations were made on each sample with An applied load of 30 kgf and an indentation dwell time of 10 seconds were used, and the average results tabulated. An Agilent G200 nano-indenter machine (University of Johannesburg) was used to carry out nano-indentation tests on the oxidised samples with a maximum depth of 800 nm, and at the WC-Co/braze interfaces. A 300 gf load and 10 seconds dwell time were used. Each successive indent was displaced by 2 µm to avoid the overlapping of plastic deformation zones. The measurements were repeated 3 times for each sample per test, and the average hardness was calculated from the data obtained.

The Vickers hardness tester uses a pyramid sharp-pointed diamond indenter with an included angle of 136° between the opposite faces (Figure 3.1). The diamond indenter was forced into the material at a given indenting load for a specific indentation time. The hardness values were calculated using Equation 3.1 [86].

$$HV = \frac{1.8544 \text{ x } P}{d^2} \qquad \textit{Equation 3.1}$$

Where,

HV = Vickers hardness number,

P = Applied load (kg), and

d = Average length of the indentation diagonals (mm).

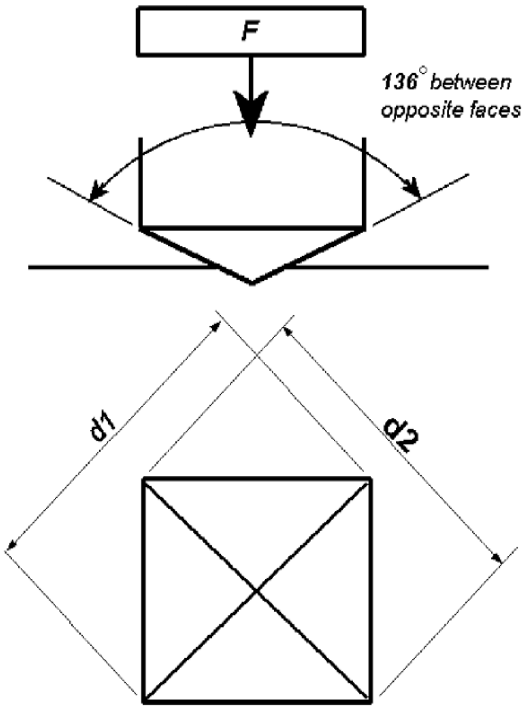

Figure 3.1: Schematic showing the geometry of the Vickers hardness diamond indenter and the measured diagonal lengths [87].

3.1.2. Density

The Archimedes principle was used to measure the density of the as-received sintered samples. The density measurements were done by first measuring the dry weight of the samples. Samples were then suspended in distilled water and weighed to give the weight in water. Three samples of each WC-Co grade (different WC grain size and Co content) were measured and the average taken as the density of that grade. The density values were determined using Equation 3.2 [88].

$$\rho = \rho_{water} \left(\frac{Wt_{dry}}{Wt_{Wet\ mass} - Wt_{susp}}\right) \qquad \textit{Equation 3.2}$$

Where,

ρ = Density of sample,

ρ_{water} = Density of water, ambient temperature dependent,

Wt_{dry} = Dry mass of the sample (g),

$Wt_{wet\text{-}mass}$ = Wet mass of the sample (g), and

Wt_{susp} = Suspended weight of the sample (g).

3.1.3. Magnetic saturation

A calibrated Reef-Lex (Type ST-24) saturation induction measuring system was used to measure the magnetic saturation of the samples. The binder magnetic saturation is a measure of the amount of the ferromagnetic material in the cemented carbide. Hence, the magnetic saturation can be used to determine the Co content of the compacts. Magnetic saturation is determined by the magnetic pull of cemented carbides in a homogeneous magnetic field to saturate the sample. A sample containing 1 wt% undissolved Co is equal to 2.02 $\mu Tm^3/kg$ [24]. The different WC-Co grades were measured five times and the average was taken as the magnetic saturation of that sample type.

3.2. Oxidation tests

WC-Co cylindrical samples with dimensions of Ø8 x 10 mm were used, Figure 3.2. Samples of the same grade (three per set) were individually placed in alumina crucibles and oxidised in an Elite BRF-18 muffle furnace (tolerance = ±2°C) at temperatures 450, 500, 550, 600, 650, 700 and 750°C respectively, in air. Heating rate of 10 °C/s was used. The oxidation times used were 30, 60, 600 and 1800 seconds at top temperatures, followed by air cooling. These oxidation times will be used as a guide for the brazing tests in Section 3.3. The samples were ground and polished before oxidation, according to metallographic sample preparation steps in section 3.5. After each temperature and time interval, the WC-Co samples were removed from the furnace and weighed on an Ohaus AX523 balance (University of Johannesburg). The depth profile of hardness on oxidised WC-Co materials was measured at room temperature.

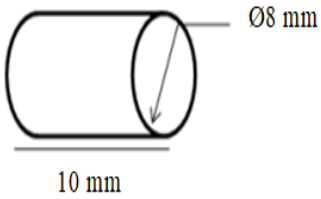

Figure 3.2: Oxidation test sample.

3.3. Brazing tests

The samples used for brazing were cemented carbides, with cylindrical dimensions of Ø8 x 20 mm. Figure 3.3 shows a schematic of the brazing assembly used for the experiments. Two WC-Co samples of the same Co grade were assembled on a heavy-duty bench vice and a fixturing pressure of about 7 MPa was applied on the assembly. Interlayer thickness was varied from 8 µm to 24 µm using a Ni630 (VitroBraze) foil with thicknesses of 10 µm and 25 µm, respectively. *BrazeTecH90* flux was applied on the WC-Co surfaces prior to the brazing process. The brazing process was performed under atmospheric conditions. The assembly was heated to 600°C using an oxyacetylene torch, creating a heating rate of approximately 10°C/s, then to the brazing temperature of

710°C. The holding time was 30 seconds at top temperature allowing time for the braze filler alloy to flow into the joint by capillary action.

A Smart Sensor B64 infrared thermometer (±2°C) was used to measure the temperature evolution at the joint seams. The temperature was measured from a distance of about 0.5 m, without contact with the workpieces. After the brazing treatment, the specimens were then allowed to cool in air. The specimens were cut along the cross-sections using a diamond cutting tool, according to Section 3.4.

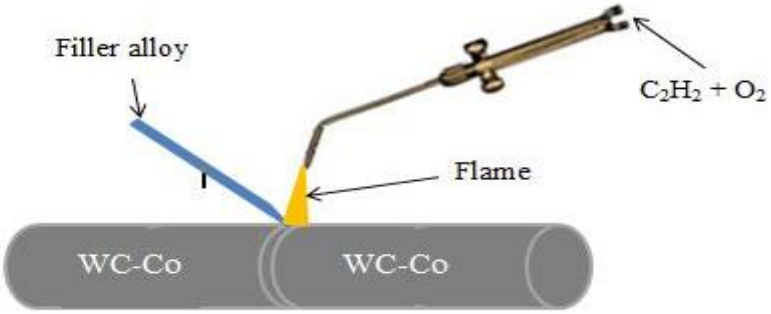

Figure 3.3: Schematic showing the assembly used for WC-Co brazing.

3.3.1. Braze filler alloy

The Ag-based *BrazeTec4900A* [89] filler alloy with a melting temperature range of 670 - 690°C was used for the brazing tests. The melting temperature of the filler alloy was lower than that of the WC-Co samples. The filler alloy had good wetting properties for the WC-Co surfaces due to the high silver (Ag) content, substantiated by the manganese (Mn) and nickel (Ni) contents. A *BrazeTecH90* flux was applied on the WC-Co surfaces prior to the brazing process.

3.4. Metallographic sample preparation

The tests described in this section were carried out after the samples were ground and polished. Samples that had to be examined by optical and/or electron microscopy were subsequently etched.

3.4.1. Cutting of the samples

The brazed samples were cut in half in order to examine the cross-section through the brazed joint. This was done using a Struers Secotom-10 precision cut-off machine, with a detachable diamond MOD13 cut-off wheel. The diamond cut-off wheel was operated at 3400 rpm and the sample feed rate was 0.015 mm/s. This ensured that the load on the cutting wheel was minimised, to avoid damaging the sample.

3.4.2. Mounting of the samples

The cut samples were mounted in PolyFast using a CitoPress-10 mounting machine. PolyFast is made up of a mixture of a carbon filler and Bakelite. The carbon filler makes the resultant mount electrically conductive and hence suitable for SEM analysis. The mounting machine uses a 1000 W heating unit, with a heating range of 80 - 200°C. A pressure of 6 MPa and mounting time of 6 minutes and 30 seconds were used. The pressure applied during the mounting process is controlled by the hydraulic system fitted in the machine. Each mounting operation took seven minutes, with three and a half minutes used for heating the PolyFast and three and a half minutes used for cooling the mounted sample.

3.4.3. Grinding and Polishing

The mounted samples were ground and polished using grinding/polishing discs to remove the scratches as a result of grinding, and to produce a mirror-like surface finish. Grinding and polishing of the samples was done using a Saphire 520 automatic machine. After each grinding and polishing stage, the samples were placed in an ultrasonic bath to remove the debris before proceeding to the next stage of grinding and/or polishing. Table 3.1 summarizes the grinding and polishing steps that were followed.

Table 3.1: A summary of the grinding and polishing steps.

Step No.	Disc	Grit size (µm)	Water	Suspension	Time (min)
1	MD-Piano	1200	Yes	-	20
2	MD-Largo	-	-	6 µm diamond	15
3	MD-Dac	-	-	3 µm diamond	15
4	MD-Nap	-	-	1 µm diamond	5

3.4.4. Etching

For LOM and SEM analyses, the specimens were etched in order to make the microstructure visible. Murakami's reagent (10% NaOH and 10% $K_3[Fe(CN)_6]$, of equal volume) was used as the chemical etchant. Chemical etching was done for about 30 seconds. After etching the samples were rinsed under running water for about a minute and then dried using compressed air.

3.5. Characterisation of the samples

3.5.1. Microstructural analysis

The microstructures of the as-received, oxidised cemented carbides were examined using a Leica DM 6000® optical microscope. The brazed cemented carbides were also examined. All the samples were examined by a high resolution Zeiss Sigma Field Emission Scanning Electron Microscope (FEG-SEM500) equipped with both back-scattered and energy dispersive X-ray (EDX) detectors. The SEMs for as-received samples, and oxidised and brazed cemented carbides were run at 15 kV and 20 kV, respectively. This was done in back-scattered electron imaging (BSD) to distinguish the phases present in the cemented carbides. EDX spot, area and line analyses were performed to determine the compositional variations.

3.5.2. Phase analysis

X-ray diffraction (XRD) was done to using a Bruker D2 Phaser® diffractometer to identify the phases present in as-received, oxidised and brazed cemented carbides. This was also used to confirm the findings from the respective SEM-EDX analyses. Measurements were taken within the range of 2θ = 10 - 110° at a step size of 0.02° - 0.2° per second. The diffractometer was operated at generator settings of 30 kV and 20 mA at a temperature of 25°C. The patterns obtained were analysed using OriginLab software.

3.6. Shear strength tests

In order to evaluate the joint shear strength, the brazed samples were cut into specimens with a length of ~20 mm and 8 mm diameter. The mechanical strength of the joints was tested using a universal test machine (UTM-SANS SHT 4106), in accordance with ISO3327:2009 [91]. Figure 3.4 shows a side view sketch of the jig that was used for the shear stress experiments.

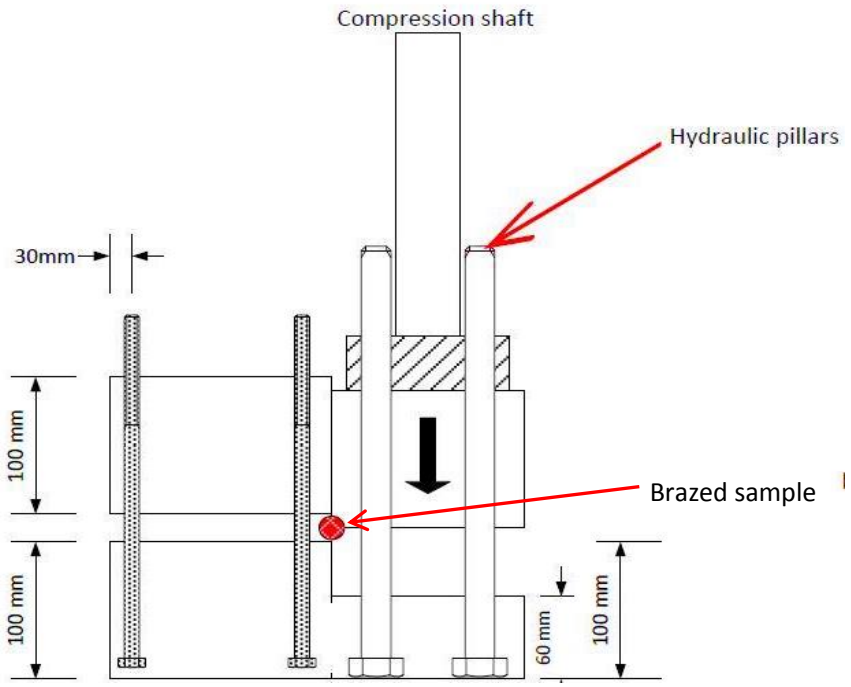

Figure 3.4: Schematic side view of the jig used for shear stress experiments.

4. RESULTS

This chapter describes the results of the experimental work carried out on the WC-Co materials. This includes the physical, mechanical, as well as the microstructural properties of the as-received, oxidised and the brazed WC-Co samples and the filler alloy.

4.1. Material characterisation

The WC-Co cemented carbides and the filler alloy supplied by Ultramat (Pty) Ltd. and Umicore (Pty) Ltd, respectively, were characterised according to their chemical, physical and mechanical properties. This section reports on the chemical and phase compositions, hardness, density and porosity of the as-received materials, in order to detect and characterise any manufacturing defects and factors that could affect the results from the brazing tests.

4.1.1. WC-Co hardmetals

4.1.1.1. Microstructural analysis of as-received materials

Figures 4.1 and 4.2 show the SEM-BSD micrographs of the WC-Co cemented carbides, with 6 wt% and 10 wt% cobalt contents, respectively. The microstructures consisted of typical angular WC grains (light) and the Co phase (dark) between the WC grains. All microstructures were found to contain a mixture of coarse and fine WC grains. The apparent WC grain sizes of the WC-Co materials were estimated using ASTM B390-92 [91].

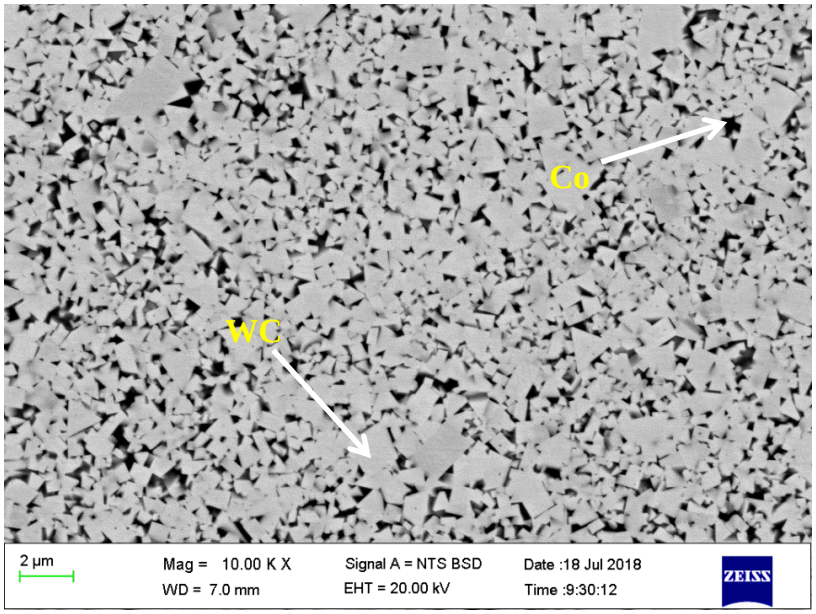

Figure 4.1: SEM-BSD image showing the WC-6wt%Co microstructure. Coarse and fine WC grains are randomly arranged in the Co matrix.

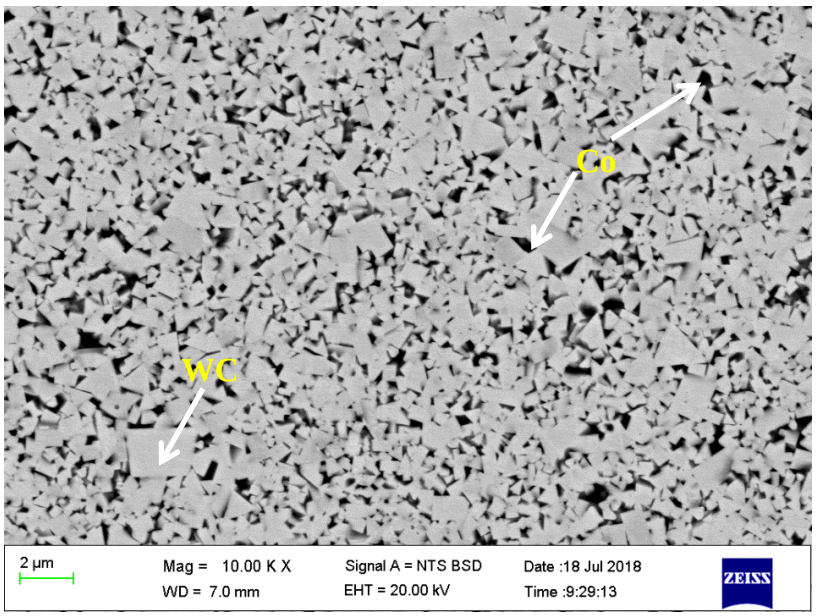

Figure 4.2: SEM-BSD image showing the WC-10wt%Co cemented carbide microstructure. A mixture of fine and coarse WC grains is cemented in the Co matrix.

4.1.1.2. Phase analysis and chemical compositions

Figure 4.3 shows the XRD patterns of the WC-Co cemented carbide materials, with cobalt binder contents of 6 wt% and 10 wt%, respectively. XRD measurements were conducted using a Bruker D2 Phaser fitted with a LynxEye detector. The XRD patterns for both WC-Co samples were collected over a 2θ range of 20° to 100° for 10 minutes. The XRD patterns show the presence of WC and Co phases. The cobalt peaks had low intensity due to the shielding effect of WC grains. There was no evidence of detrimental phases such as eta phases or other impurities in any of the cemented carbides. This was also verified by SEM-EDX analysis.

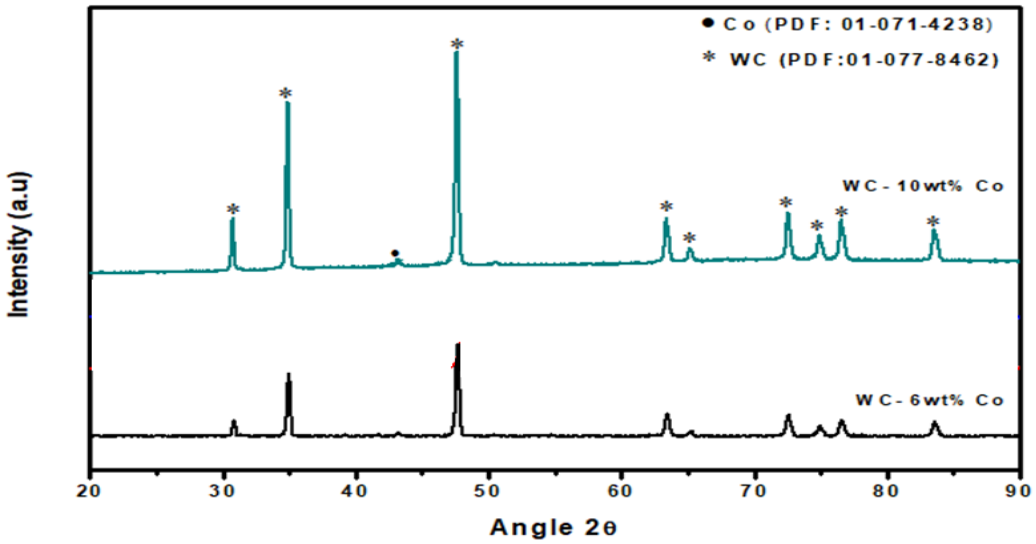

Figure 4.3: XRD patterns of the WC-Co cemented carbides in the as-received condition.

4.1.1.3. Chemical compositions

The *SEM-EDX* analyses maps of the WC-Co cemented carbides with cobalt contents of 6 wt% and 10 wt% are respectively shown in Figures 4.4 and 4.5. *SEM-EDX* maps are typical of WC-Co cemented carbides, and the respective elemental compositions are reported in Table 4.1. Three measurements were carried out on selected areas, and the average chemical composition is reported in Table 4.1. The elemental EDX maps were generated from these. Figures 4.4 and 4.5, and Table 4.1 confirmed the supplier specifications that the WC-Co cemented

carbide rods contained cobalt binder contents amounting to 6 wt% and 10 wt%, respectively.

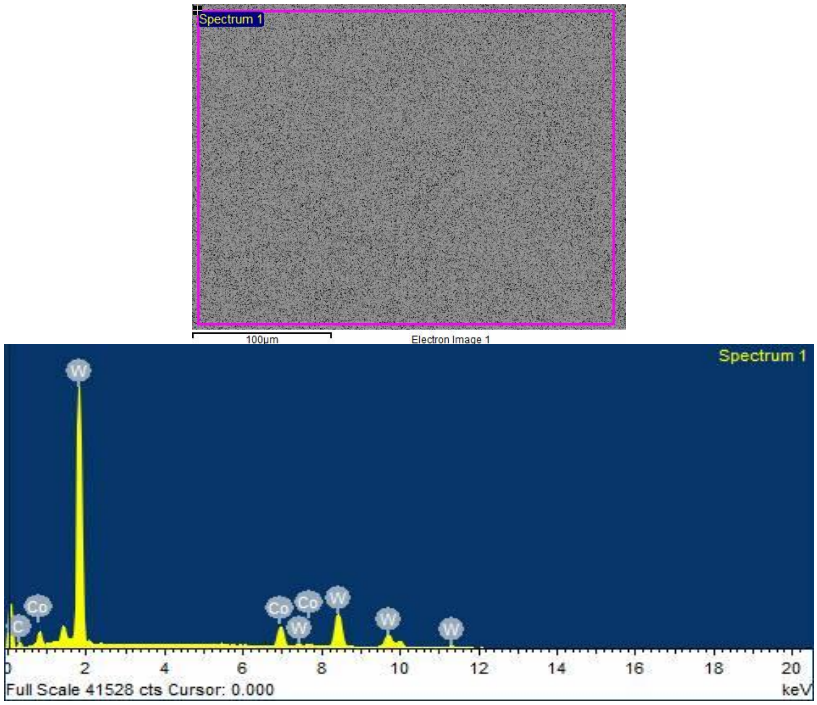

Figure 4.4: EDX spectrum of WC-6wt%Co in as-received condition.

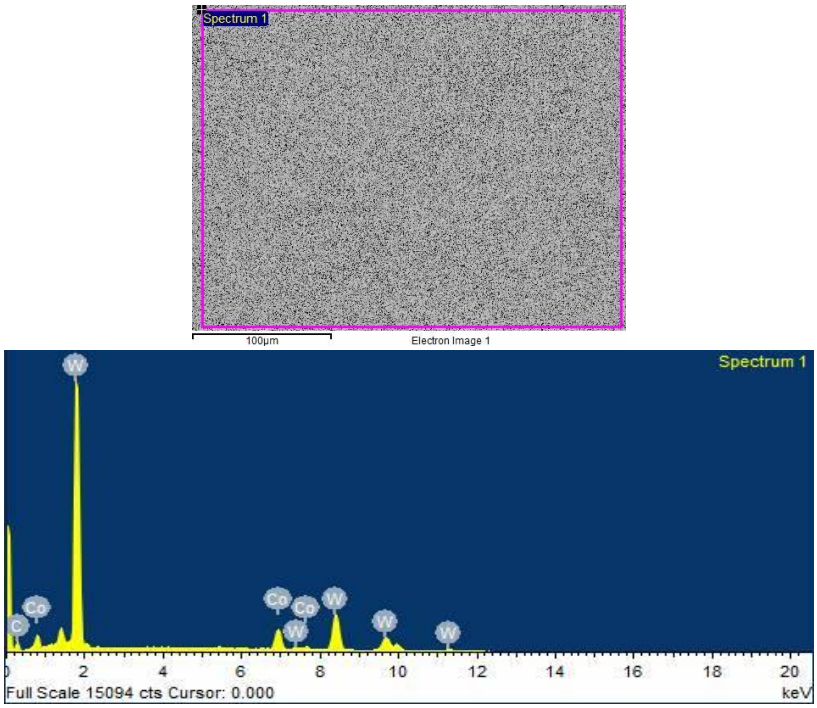

Figure 4.5: EDX spectrum of WC-10wt%Co in as-received condition.

Table 4.1 shows a summary of the EDX results. Three measurements were carried out on a selected area and an average was taken as the amount of each respective element present. There were very small differences between the analyses, and measurements were within reasonable experimental errors. The mean WC grain size was estimated by analysing the micrographs in section 4.1.1.1 using ImageJ software.

Table 4.1: Measured elemental compositions and the mean WC grain sizes of as-received WC-Co samples.

Sample	**C**	**Co**	**W**	**Mean WC grain size**
	wt%			**µm**
WC-6wt%Co	7.04±0.14	6.02±0.20	86.94±0.12	1.34±0.20
WC-10wt%Co	7.09±0.20	10.56±0.18	82.34±0.15	1.20±0.21

4.1.1.4. Mechanical and physical properties

The mechanical and physical properties of the as-received WC-Co cemented carbide rods are shown in Table 4.2. The hardness of the WC-Co samples was measured using an indentation load of 30 kgf and an indentation time of 10 seconds. An average of five indentations was taken as the hardness of each sample grade. The properties are typical of the WC-Co grades and within the supplier specifications.

Table 4.2: Mechanical and physical properties of the as received WC-Co cemented carbide rods.

Sample	**Average Hardness, HV_{30} (kgf/mm^2)**	**Density (g/cm^3)**	**Magnetic saturation ($x10^{-4}T$)**
WC-6wt%Co	1518±10	14.97±0.13	5.75
WC-10wt%Co	1676±15	14.43±0.20	9.87

Figures 4.6 and 4.7 show the surface of the WC-Co cemented carbides, with 6 wt% and 10 wt% cobalt contents, respectively. Porosity levels of the different WC-Co samples were estimated in accordance to ISO 4499-4 [92]. Both cemented carbide grades showed B04 porosity, which confirmed that the parts were adequately sintered.

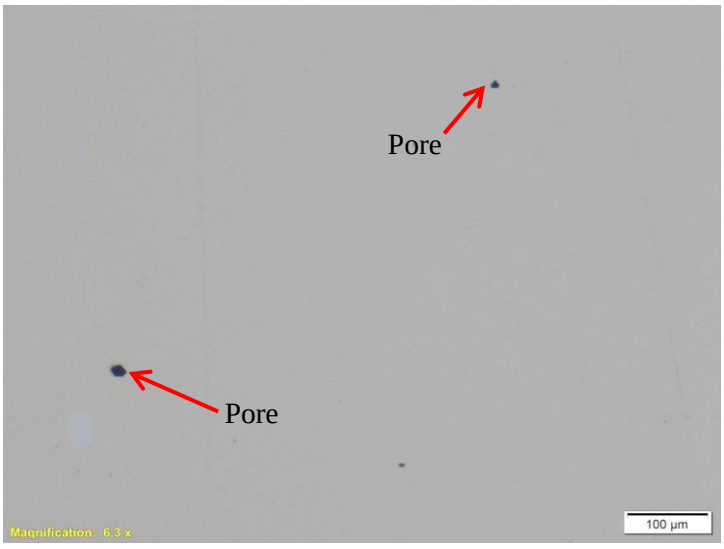

Figure 4.6: Polished surface of WC-6wt%Co cemented carbide showing B04 surface porosity.

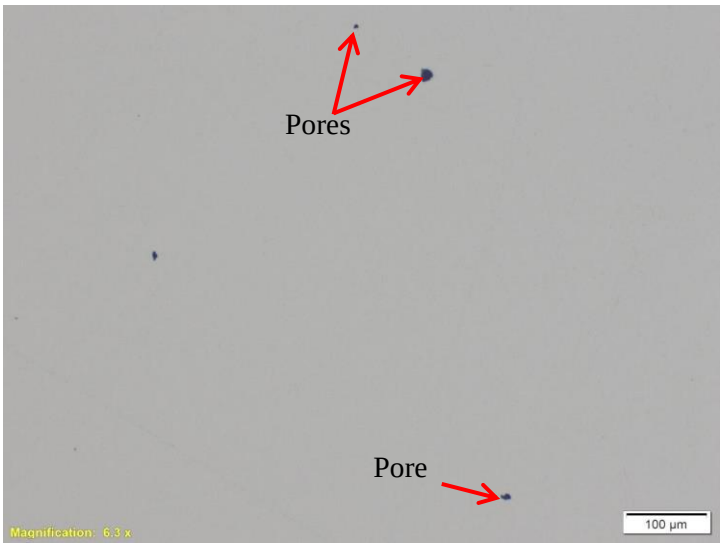

Figure 4.7: Polished surface of WC-10wt%Co cemented carbide rod showing B04 surface porosity.

4.1.2. Braze filler alloy

4.1.2.1. Microstructural analysis

At least three distinct phases could be identified in the B-Ag49CuZnMnNi filler alloy microstructure: a light grey background (A), dark grey patches (B), light grey patches (C) and dark spots (D), Figure 4.8. These phases were identified by carrying out EDX spot analyses on three different spots of each phase on the SEM image. The average composition of the phases obtained for B-Ag49CuZnMnNi from EDX is presented in Table 4.3, with the representative EDX spectra presented in Figures 4.9 - and 4.11. The overall filler alloy composition was typical of supplier specification [89]. The light grey background was α-Ag which contained high amounts of Cu and Zn, while the dark grey patches were α-Cu which high amounts of Ag and Zn. The presence of Ni in the dark grey patches confirmed that it was the α-Cu, because Ni has lower solubility in α-Ag than in the α-Cu phase. Hence, Ni was rejected from α-Ag to preferentially settle and stabilise in was α-Cu phase [81 - 83]. This was also confirmed by the EDX results in Table 4.3.

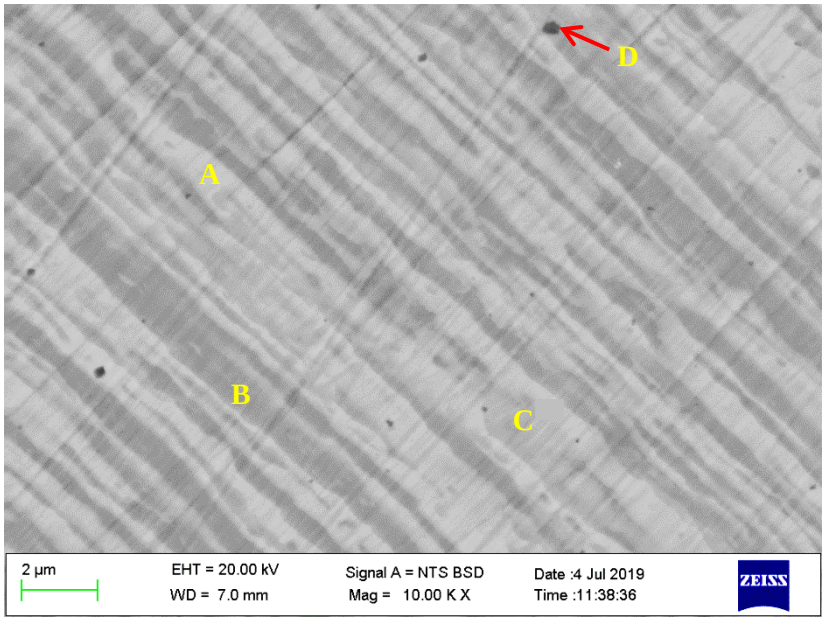

Figure 4.8: SEM-BSD microstructure of B-Ag49CuZnMnNi filler alloy showing the different phase regions.

Table 4.3: EDX analyses of the as-received BrazeTec4900A filler alloy.

Phase description	**Ag**	**Cu**	**Zn**	**Mn**	**Ni**
	wt%				
Overall	50.10±0.20	27.93±0.15	18.96±0.20	2.19±0.18	0.82±0.30
Supplier specification [89]	**49.00**	**27.50**	**20.50**	**2.50**	**0.50**
Light grey background (A)	50.81±0.20	25.05±0.18	21.58±0.20	1.71±0.15	0.85±0.20
Dark grey patch (B)	25.12±0.10	44.85±0.20	23.97±0.17	3.06±0.15	3.00±0.15
Light grey patch (C)	33.96±0.16	38.01±0.10	24.26±0.21	2.08±0.30	1.69±0.18

Figures 4.9 – 4.12 show the typical *SEM-EDX* analyses maps of the different regions on the filler alloy microstructure. Three measurements were taken at different spots, and the average chemical composition is given in Table 4.3. It is shown that the light grey areas are rich in Ag, dark grey areas rich in Cu, and Mn is present in all the different phases. These *EDX* maps are typical of the supplier specification [89] as reported in Table 4.3.

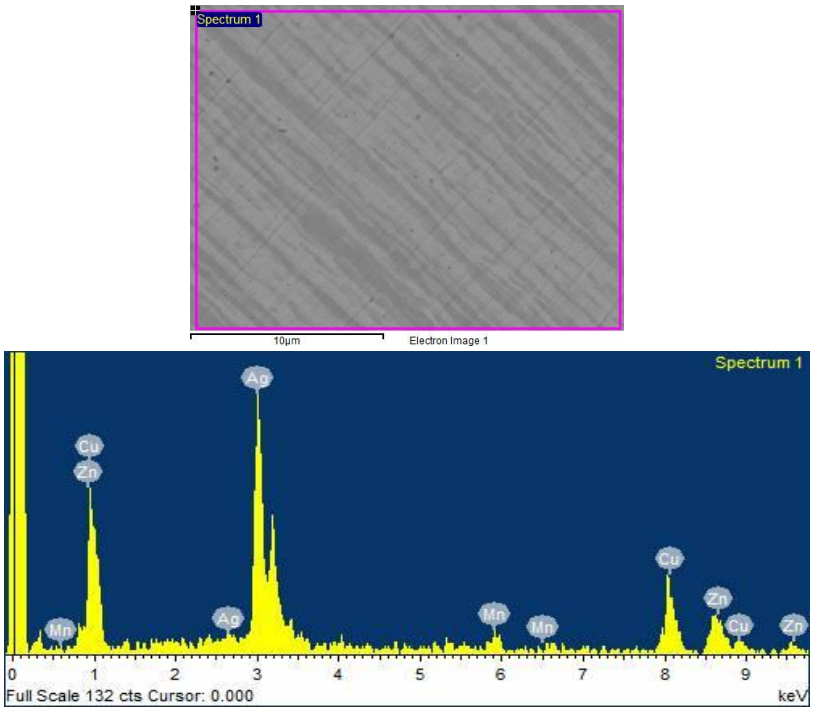

Figure 4.9: Overall SEM-EDX *spectrum* of *B-Ag49CuZnMnNi filler alloy.*

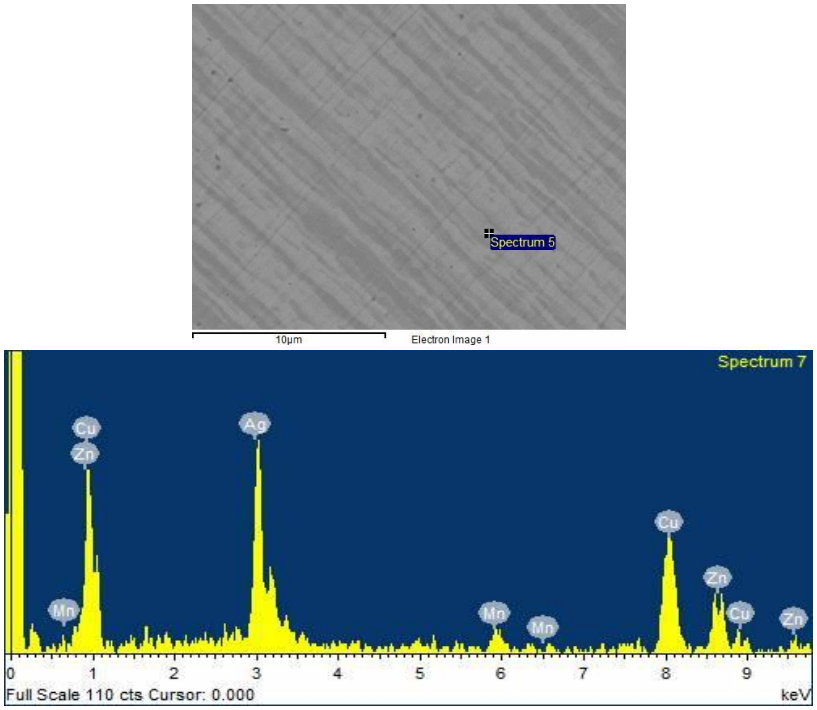

Figure 4.10: SEM-EDX spectrum of the light grey background (A) in the filler alloy.

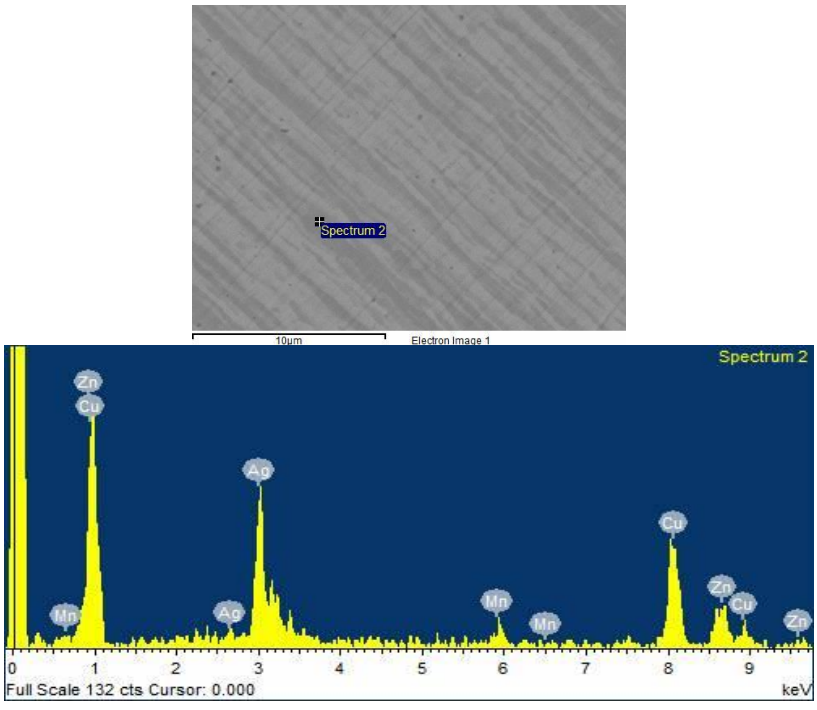

Figure 4.11: SEM-EDX spectrum of the dark grey region (B) in the filler alloy.

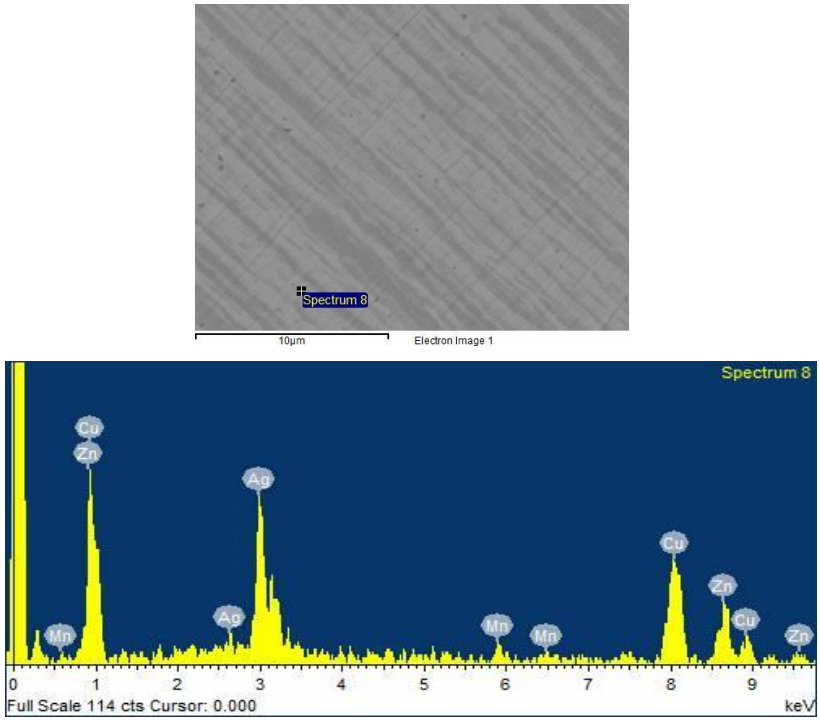

Figure 4.12: SEM-EDX pattern of the light grey region(C) in the filler alloy.

4.1.2.2. Phase analysis

Figure 4.13 shows the XRD pattern of the B-Ag49CuZnMnNi filler alloy. From the XRD results, the dominant phases in the filler alloy were α-Ag, α-Cu and CuMnNi. The light grey background (A) and the light grey patches (C) in Figure 4.8 were respectively identified as α-Ag phases, and a mixture of α-Ag and α-Cu phases rich in Zn. The dark grey patches (B) were identified as α-Cu rich in Zn. The phases were typical of the filler alloy, and supported by the SEM-EDX analyses shown in Figures 4.9 – 4.12.

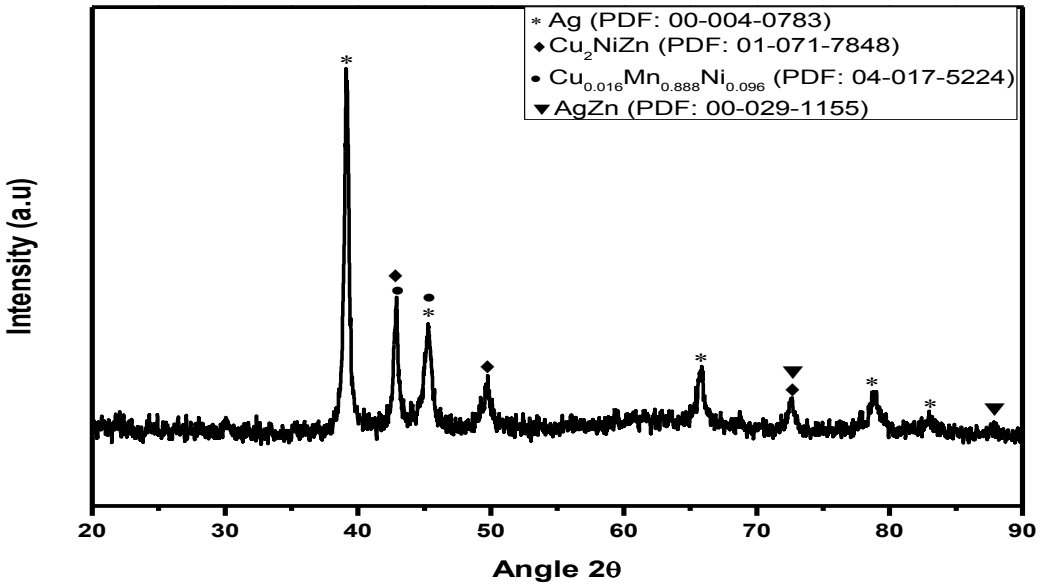

Figure 4.13: XRD pattern of B-Ag49CuZnMnNi braze filler alloy in the as-received condition.

4.1.2.3. Mechanical and physical properties

Table 4.4 shows the properties of the as-received filler alloy. Five measurements were taken for each property and the average value is given in Table 4.4. Hardness values were measured using a load of 10 kgf and a dwell time of 10 seconds. The measured density values were typical of the data provided by the supplier [89]. The supplier found shear strength of 250 - 300 MPa for carbide-to-steel brazed joints. Although this is not directly applicable to this research work, it provides a rough starting point of the potentially expected values.

Table 4.4: Material properties of the B-Ag49CuZnMnNi filler alloy.

	Average Hardness, HV_{10} (kgf/mm^2)	**Density (g/cm^3)**
Measured	181±14	8.83±0.18
Supplier specification [89]	-	8.90

4.2. Oxidation of WC-Co cemented carbides at brazing temperature

4.2.1. Oxidation behaviour characterised by mass gain

Oxidation of the WC-Co cemented carbides was studied over the temperature range 400 – 750°C, at 30, 60, 600 and 1800 seconds. A muffle furnace with chamber dimension of 200 x 230 x 210 mm^3 was used. The muffle furnace (±5°C tolerance) temperature was increased from room temperature to 400°C in 110 minutes. Figure 4.14 shows the un-oxidised sample surfaces of WC-Co cemented carbides. The sample surfaces were polished to 1 μm surface finish to eliminate surface defects that may act as preferential oxidation initiation sites. Oxidation of the WC-Co samples was highly negligible in the 25 – 400°C temperature intervals, and was thus excluded from the analysis. The oxidation temperature range was chosen to encompass the filler alloy melting temperature range of 680 – 705°C [89]. The oxidation behaviour of the WC-Co cemented carbides was measured and then plotted as mass gain against temperature, Figure 4.15. At higher holding times (i.e. 600 and 1800 seconds), WC-6wt%Co experienced higher thermal oxidation (recorded in terms of mass gain) than WC-10wt%Co. This was attributed to the preferential oxidation of WC grain and the slow formation of the protective oxide layer containing $CoWO_4$ on WC-6wt%Co samples.

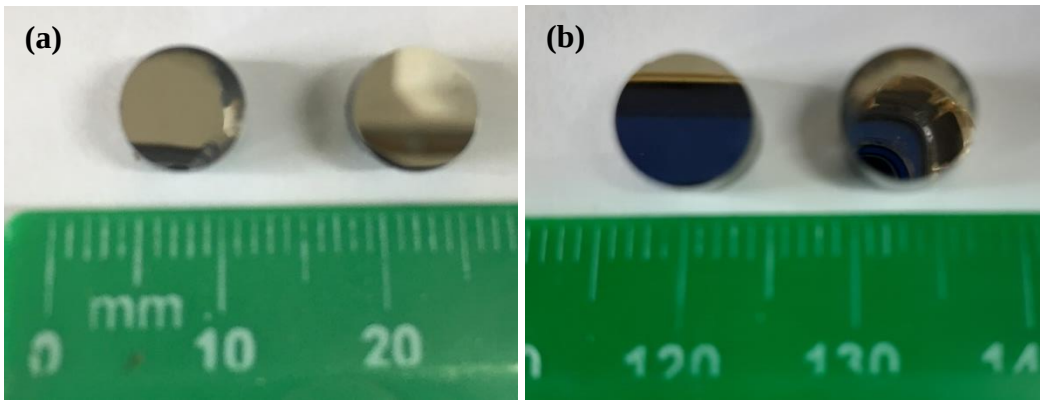

Figure 4.14: Polished surfaces of un-oxidised base materials (a) WC-6wt%Co, and (b) WC-10wt%Co.

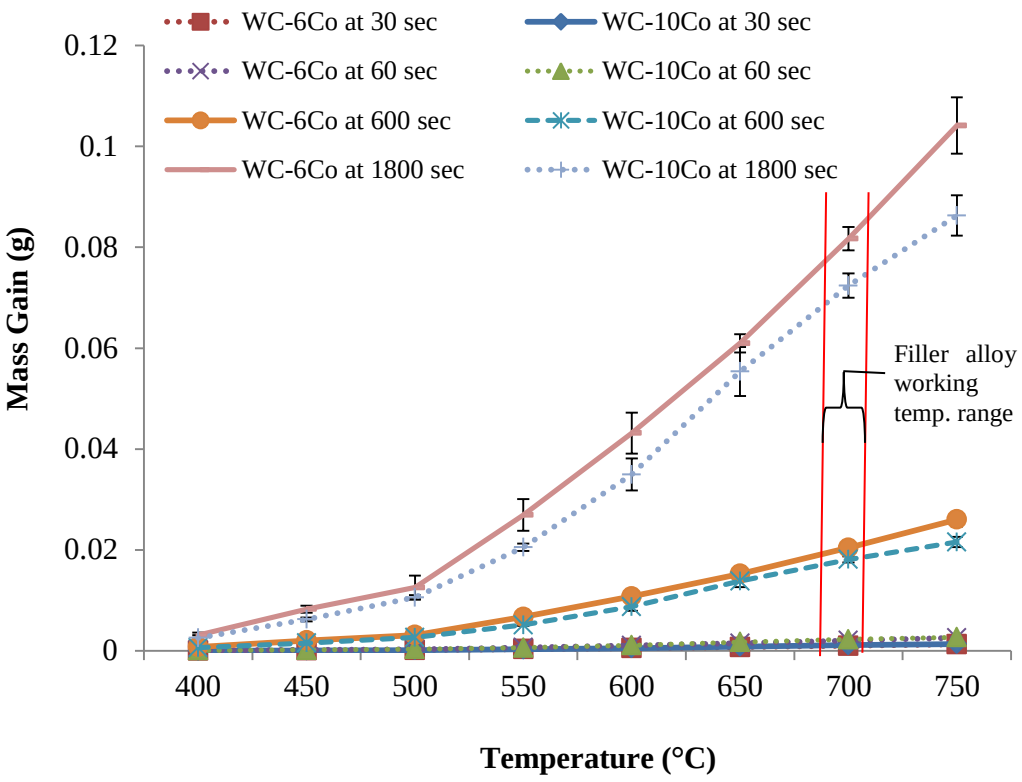

Figure 4.15: Mass gain versus temperature of WC-Co hardmetals oxidised from 400°C to 750°C, in air.

4.2.2. Analysis of the oxide layers that formed on WC-Co substrates

4.2.2.1. Optical analyses: oxide layers

Considering the working temperature of the filler alloy [89], optical analysis of the oxide layers was done on the WC-Co components that were oxidised at 700°C at different holding times. It was shown that with an increase in the holding time, at 700°C, the oxide layer changed from dull grey to a mixture of dark blue and light green, Figures 4.16 and 4.17. The oxidised WC-6wt%Co samples still showed a lot of light green oxide at 1800 seconds (Figure 4.16 (d)), due to the continued oxidation of WC grains. Comparatively, WC-10wt%Co samples showed dark blue oxide scales much earlier, at 600 seconds, because the preferential oxidation of the Co phase led to the formation of dark blue $CoWO_4$ oxide (Figure 4.17 (c)). At 1800 seconds, WC-10wt%Co samples showed traces

of light green oxides which were attributed WC oxidation. The oxide layers also showed the presence of micro-cracks, which formed as a result of the formation of CO and CO_2 at the interfaces and thermal shock experienced during thermal oxidation tests. The results were in complete concordance with the findings of Bagnall et al. [94] and Chen at al. [95].

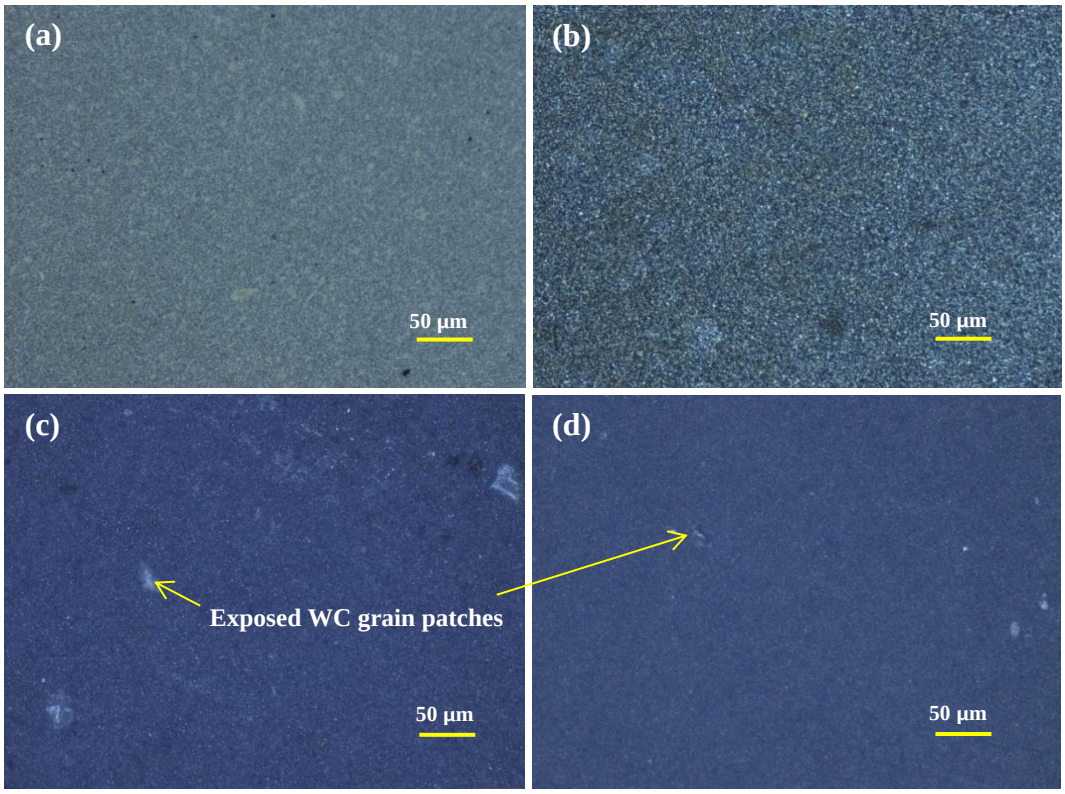

Figure 4.16: The surface oxide layer of WC-6wt%Co oxidised at 700°C for (a) 30, (b) 60, (c) 600, and (d) 1800 seconds, consisting of $CoWO_4$ (dark blue) and WO_3 (light) oxides.

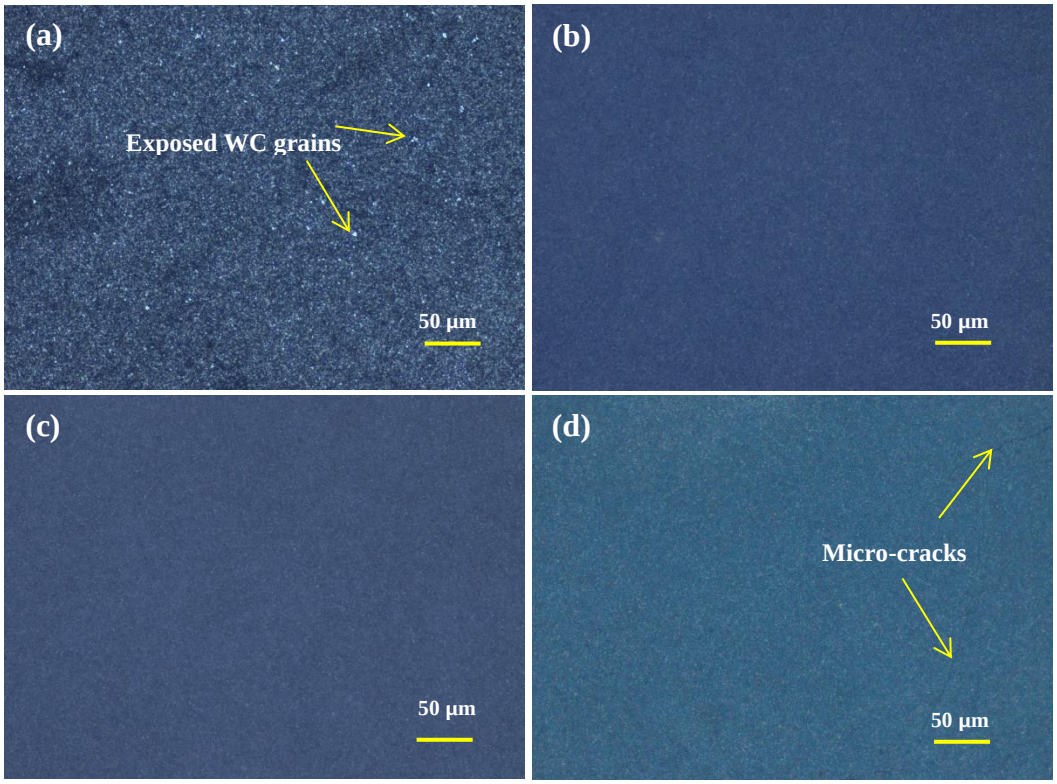

Figure 4.17: The surface oxide layer of WC-10wt%Co oxidised at 700°C for (a) 30, (b) 60, (c) 600, and (d) 1800 seconds, consisting of $CoWO_4$ (dark blue) and WO_3 (light) oxides.

4.2.2.2. Microscopic analysis of the oxide layers

Figures 4.18 and 4.19 show the corresponding SEM-BSD micrographs of the oxide layers in Figures 4.16 and 4.17. It is shown in Figures 4.18(a) and 4.19(a) that WC-10wt%Co started to oxidise much earlier than WC-6wt%Co. the oxide layer appeared mushy in WC-10wt%Co whilst WC-6wt%Co still showed the underlying 'original' WC-Co microstructure. At 60 seconds oxidation time, the oxide layers on both WC-6wt%Co and WC-10wt%Co showed protruded areas which were confirmed to be Co_3O_4 by EDS. With increasing oxidation time to 1800 seconds, these protruding phases 'grew' and coalesced to form bigger oxide phases. The bigger phases were identified as $CoWO_4$, which confirmed the dual oxidation of WC grains and the Co binder phase. Denser and thicker oxide layers were thus subsequently formed. Whilst coalescence is apparent, these oxide phases still appeared porous in WC-6wt%Co, Figure 4.18(d).

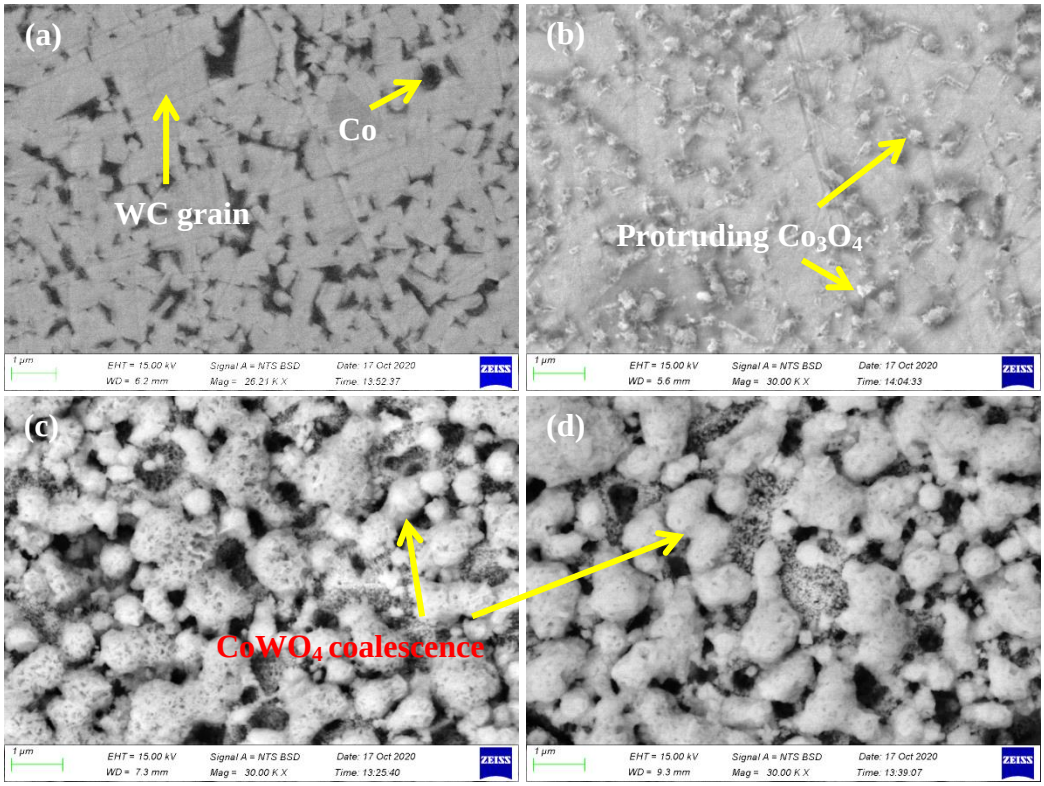

Figure 4.18: SEM-BSD micrographs showing the oxide layer surface of WC-6wt%Co oxidised at 700°C for (a) 30, (b) 60, (c) 600, and (d) 1800 seconds.

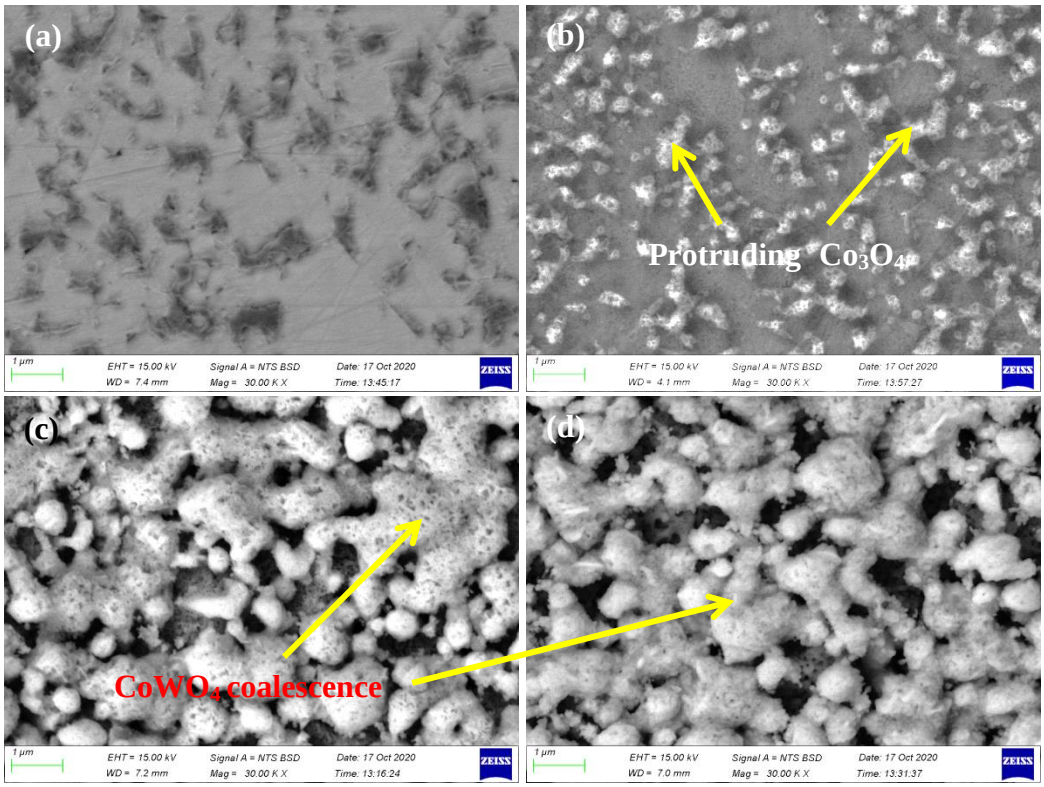

Figure 4.19: SEM-BSD micrographs showing the oxide layer surface of WC-10wt%Co oxidised at 700°C for (a) 30, (b) 60, (c) 600, and (d) 1800 seconds.

4.2.2.3. Phase analysis of the oxide layers

The XRD spectrums of the oxide layers that formed on WC-Co samples upon oxidation at 700°C are shown in Figures 4.20 and 4.21. The XRD patterns show the presence of five phases: Co, $CoWO_4$, Co_3O_4, WC and WO_3. It is shown that at oxidation time of 30 seconds, the cemented carbides consisted mainly of WC and Co phases. Upon increasing the oxidation to 1800 seconds, the cemented carbides surfaces consisted of $CoWO_4$, Co_3O_4, and WO_3, which confirmed the dual oxidation of WC and Co phases. The early formation of $CoWO_4$ and Co_3O_4 in WC-10wt%Co showed that the Co phase was priori to be oxidised. With increasing oxidation time, the intensity of the WC peaks in WC-6wt%Co decreased because of their transformation to form WO_3 and the shielding effect of the WC grains by the dense $CoWO_4$ oxide phase.

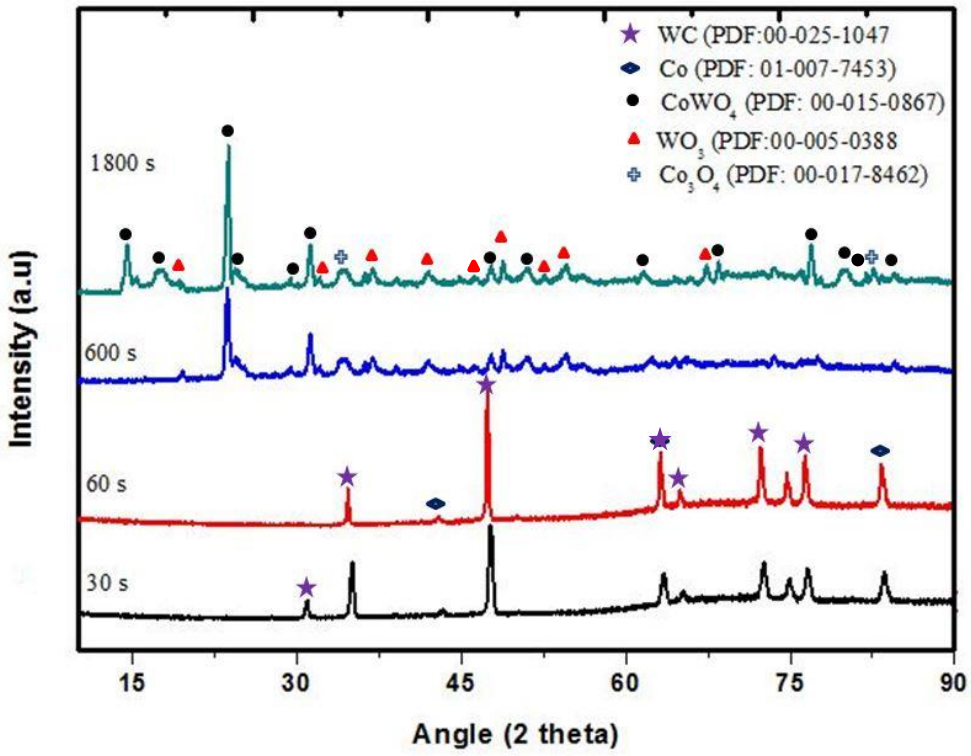

Figure 4.20: XRD patterns of oxide layers that formed on surfaces of WC-6wt%Co cemented carbides, oxidised at 700°C for (a) 30, (b) 60,(c) 600 and (d) 1800 seconds.

WC-10wt%Co showed the formation of $CoWO_4$ and Co_3O_4 when the oxidation time was increased from 30 seconds to 60 seconds. Increasing the oxidation to 1800 seconds led to an increase in the intensity of $CoWO_4$ peaks. Some of the WO_3 peaks which were observed at 600 seconds diminished when the oxidation time was increased from 600 seconds to 1800 seconds. This confirmed the formation of a protective oxide layer consisting of $CoWO_4$ and Co_3O_4, which slowed down the further oxidation of WC grains.

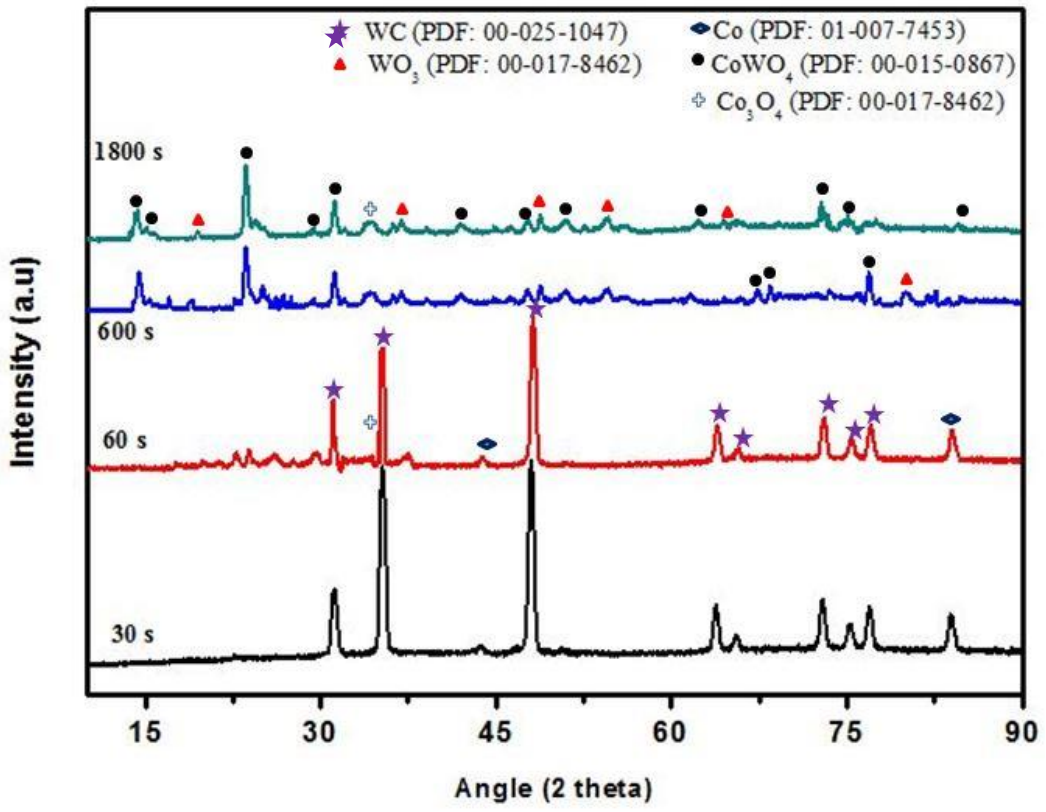

Figure 4.21: XRD patterns of oxide layers that formed on surfaces of WC-10wt%Co cemented carbides, oxidised at 700°C for (a) 30, (b) 60,(c) 600 and (d) 1800 seconds.

4.2.3. Effect of oxidation on percentage Co content of WC-Co samples

The percentage magnetic cobalt of WC-Co samples oxidised at 700°C, for 30, 60, 600 and 1800 seconds was measured. Figure 4.22 shows that the percentage magnetic cobalt of the oxidised samples generally decreased with an increase in holding time. The loss in percentage magnetic cobalt both grades, and this was

attributed to the oxidation of the Co phase to form $CoWO_4$. WC-10wt%Co samples showed the highest reduction in percentage cobalt from as early as 30 seconds due to the early formation of $CoWO_4$ [45], and this was attributed to its higher Co content compared to WC-6wt%Co samples.

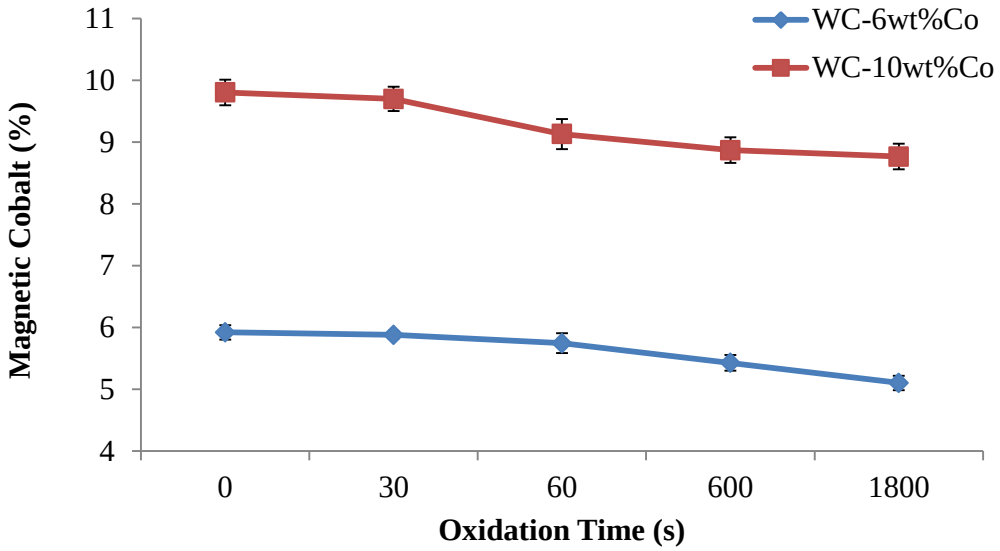

Figure 4.22: Variation of percentage magnetic cobalt of WC-Co, non-oxidised and oxidised samples, at 700°C for different holding times.

4.2.4. Effect of thermal oxidation on micro-hardness of WC-Co

Micro-hardness distributions across the oxidised surfaces at different indentation depths are shown in Figures 4.23 and 4.24. This was performed on the oxidised samples shown in 4.2.2.1 in order to measure the extent of oxidation depth from the material surface. A general increase in micro-hardness with increasing indentation depth was observed. This showed that thermal oxidation of WC-Co materials followed a shrinking-core model. For 30 seconds oxidising time, both WC-Co grades showed a slight decrease in micro-hardness on the outermost surface which was in concordance with the oxide layer formation results in Section 4.2.2.1. Increasing the oxidising time to 1800 seconds led to the highest reduction in micro-hardness of both grades, but WC-10wt%Co samples still maintained their high hardness. Generally, WC-6wt%Co showed high hardness

loss than WC-10wt%Co owing to the thermal oxidation of WC grains, in addition to Co oxidation.

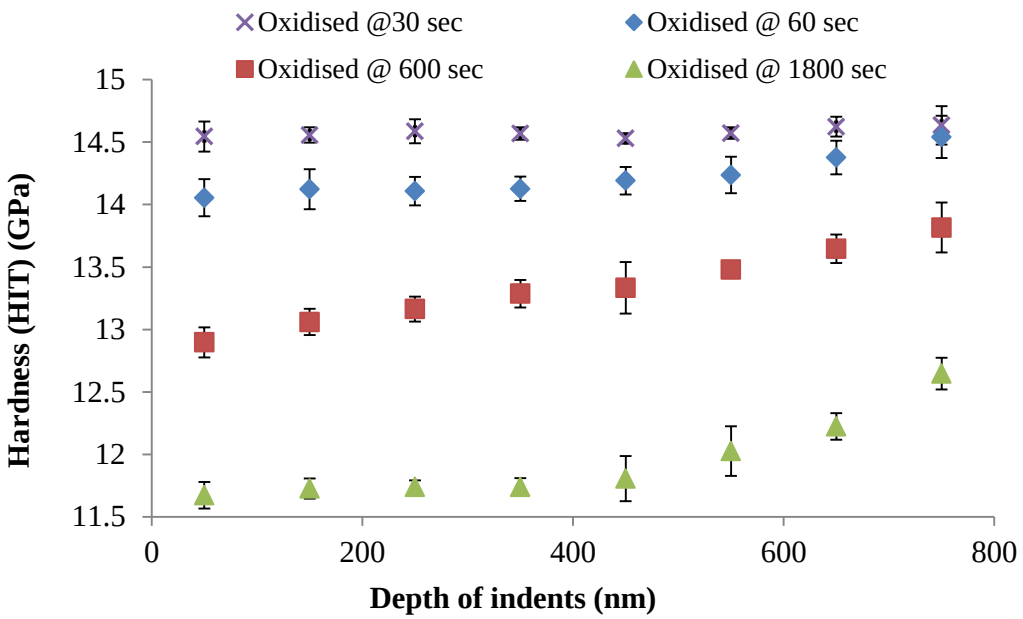

Figure 4.23: Micro-hardness variations of WC-6wt%Co samples oxidised at 700°C in air as a function of depth.

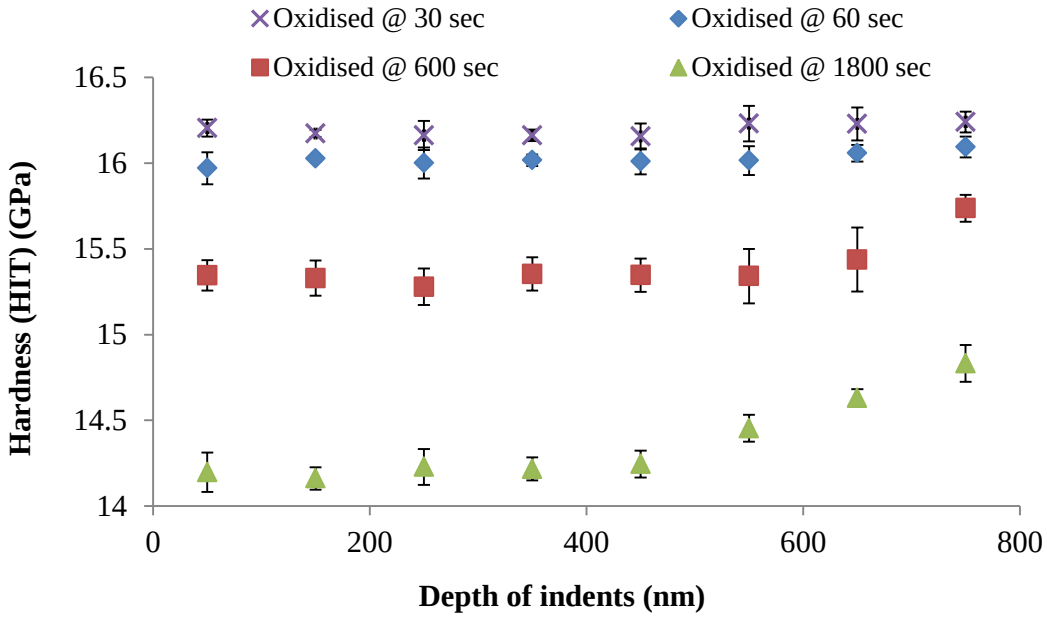

Figure 4.24: Micro-hardness variations of WC-10wt%Co samples oxidised at 700°C in air as a function of depth.

4.3. Brazing of WC-Co cemented carbides

4.3.1. Brazed joint with filler alloy thickness of 8 μm

The cross-sectional micrographs of the WC-Co brazed joints obtained at 710°C for 30s, with a filler alloy thickness of 8 μm, are respectively shown in Figures 4.25 and 4.27. At least two phases were identified in the interfacial microstructures, a light-grey phase and dark-grey phase. WC-6wt%Co brazed joints showed large interfacial α-Cu(s.s) phases, and small α-Cu(s.s) phases in the centre of the interlayer. Nucleation of interfacial α-Cu(s.s) phases started at the interfaces, with growth extending towards the interlayer centreline.

Respective SEM-EDX analyses of the phases identified in WC-6wt%Co brazed joints are shown in Table 4.5. The yellow squares indicate the area in which the analyses were done. SEM-EDX line-scan analyses were done across the interlayer/WC-Co interfaces, and selected individual elemental distributions are shown in Figure 4.26. Other elemental distributions are shown in Appendix C.

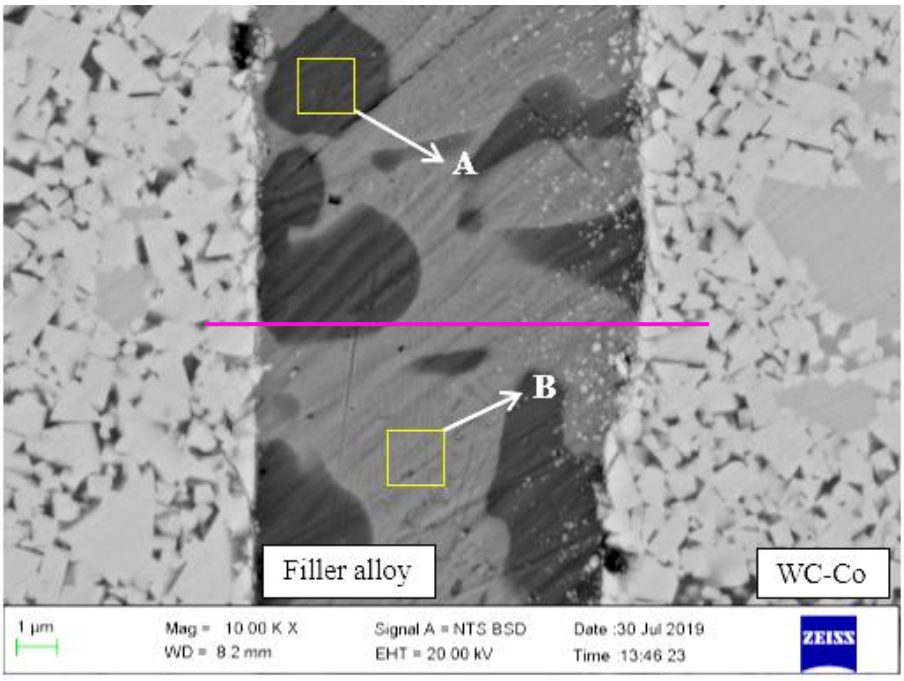

Figure 4.25: SEM-BSD micrograph of the WC-6wt%Co brazed joint at 710°C for 30s with filler alloy of 8 μm in thickness.

Table 4.5: SEM-EDX analysis of 8 µm interlayer in WC-6wt%Co brazed joint.

Element	A	B
	wt%	
Ag	9.64±0.15	71.19±0.22
Cu	52.97±0.20	10.08±0.18
Zn	19.75±0.18	12.62±0.13
Mn	0.28±0.11	0.27±0.14
Ni	3.94±0.12	1.10±0.06
W	7.43±0.18	2.36±0.12
C	4.63±0.17	1.71±0.13
Co	1.35±0.08	0.68±0.12

SEM-EDX line-scan analyses across the brazed joints showed that the concentration of Co decreased towards the interlayer centreline, while that of Ag was highest at the interlayer centreline. This was in concordance with the EDX results in Table 4.5. On the other hand, Mn and Ni was high at the braze/WC-Co interfaces which confirmed the wetting characteristics of the filler alloy [89]

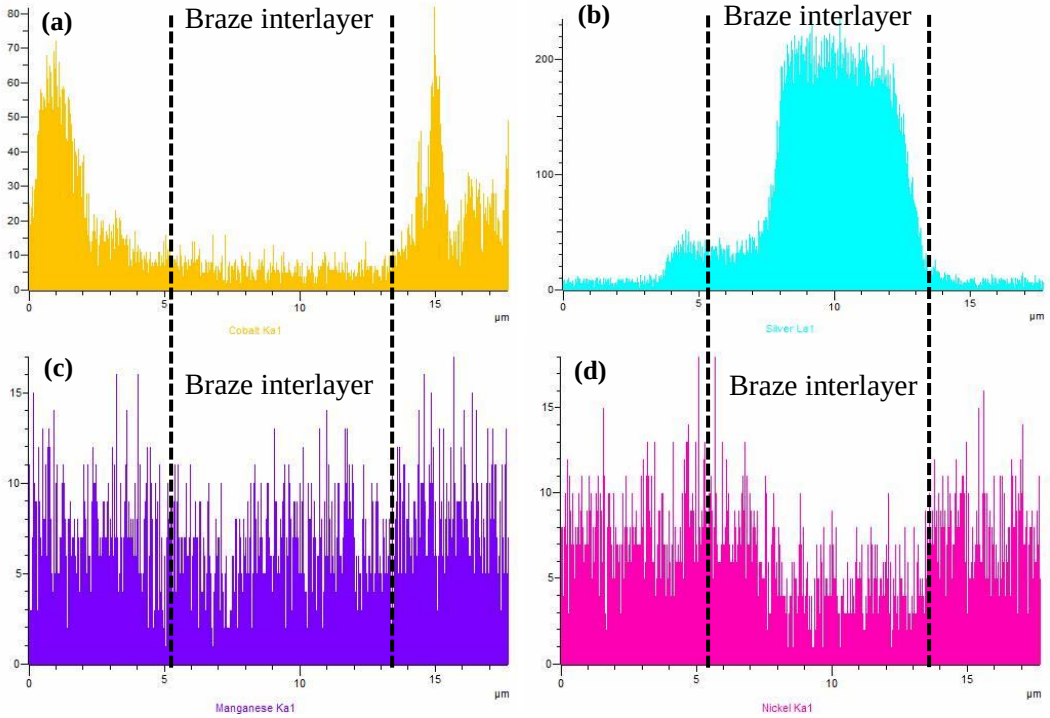

Figure 4.26: SEM-EDX line-scanning showing the distribution of (a) Co, (b) Ag, (c) Mn and (d) Ni across a WC-6wt%Co brazed joint with 8 µm filler alloy.

WC-10wt%Co showed large, well developed interfacial α-Cu(s.s) phases, even at the centre of the braze interlayer, Figure 4.27. This showed that Co controlled the interlayer solidification process, and thus the formation of α-Cu(s.s) phases. Overall, the formation of these interfacial phases suggested that nucleation started at the interfaces and growth was towards the interlayer centreline.

The SEM-EDX analyses of the respective phases identified in brazed joints are shown in Table 4.6. The yellow squares indicate the area in which the analyses were done. The inter-diffusion of Co towards the centre of the interlayer decreased from 1.57±0.18 wt% in interfacial α-Cu(s.s) phases to 0.05±0.02 wt% in α-Ag(s.s) phases found towards the centreline of the interlayer, see Figure 4.26.

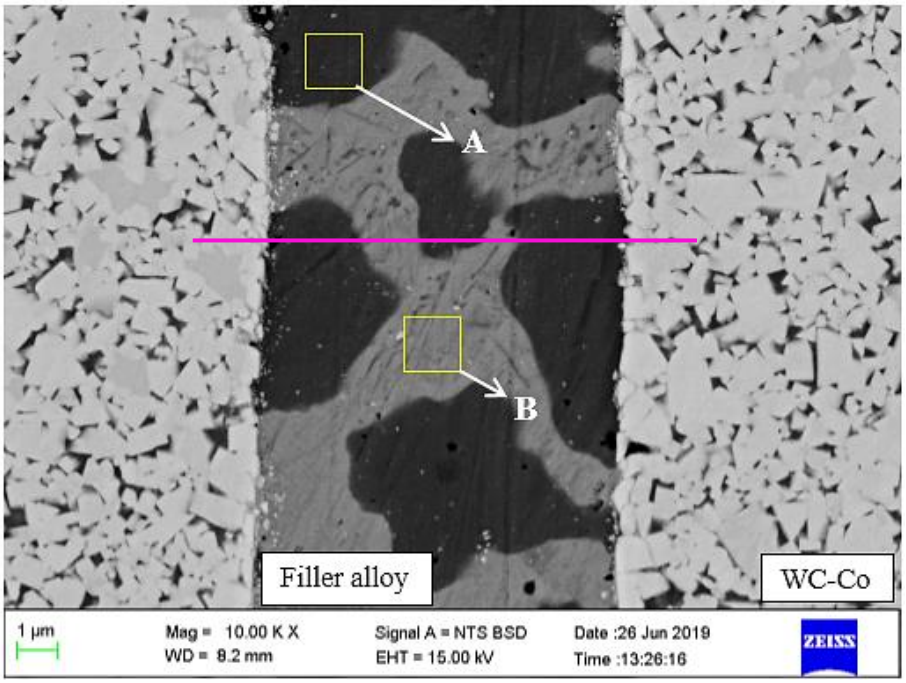

Figure 4.27: SEM-BSD image of the WC-10wt%Co brazed joint at 710°C for 30s with filler alloy of 8 µm in thickness.

Table 4.6: SEM-EDX analysis of 8 µm interlayer in WC-10wt%Co brazed joint.

Element	A	B
	wt%	
Ag	9.40±0.13	65.38±0.20
Cu	55.36±0.18	13.75±0.15
Zn	20.80±0.20	16.18±0.12
Mn	0.66±0.12	0.35±0.08
Ni	1.70±0.11	0.06±0.02
W	6.33±0.10	2.39±0.18
C	4.22±0.12	1.84±0.15
Co	1.57±0.18	0.05±0.02

Figure 4.28 shows that the concentration of Co was high at the joint interfaces, and within the dark the α-Cu(s.s) phases. This showed that the inter-diffusion of Co played a great role on the formation of α-Cu(s.s) phases and solidification of the entire interlayer. The distributions of Mn and Ni were more uniform across the brazed joints, while that of Ag increased towards the interlayer centreline.

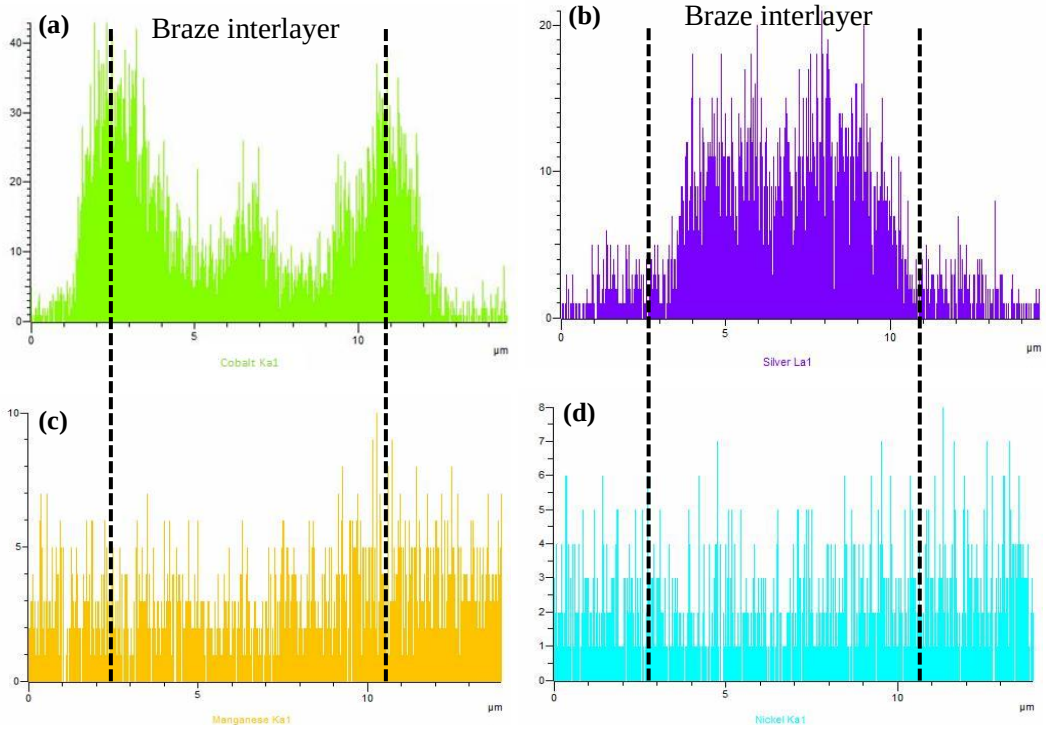

Figure 4.28: SEM-EDX line-scanning showing the distribution of (a) Co, (b) Ag, (c) Mn and (d) Ni across a WC-10wt%Co brazed joint with 8 µm filler alloy.

4.3.2. Brazed joint with filler alloy thickness of 24 µm

Figures 4.29 and 4.31 show the SEM-BSD cross-sections of the brazed joints with a filler alloy thickness of 24 µm. At least three distinct phases were identified in the interfacial microstructure. The interlayer microstructures consisted of a light-grey phase, dark-grey phase, and dark-grey feather-like eutectic phase. The estimated chemical compositions of these phases are given in Tables 4.7 and 4.8.

The interlayers in WC-6wt%Co showed the presence of lamella-like eutectic phases. The interfacial α-Cu(s.s) phases were dumbbell-shaped, with growth perpendicular to the interfaces. Table 4.7 shows that the eutectic phases (region C) were rich in Ag and Zn. Point EDX analyses were done in the marked region C.

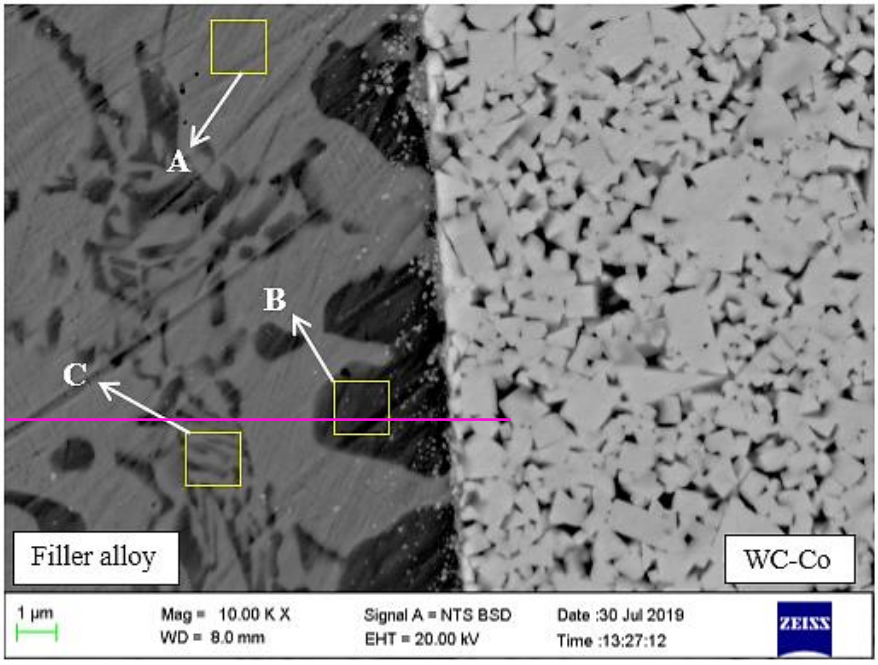

Figure 4.29: SEM-BSD micrograph of the WC-6wt%Co brazed joint at 710°C for 30 s with filler alloy of 24 µm in thickness.

Table 4.7: SEM-EDX analysis showing chemical composition of 24 µm WC-6wt%Co brazed interlayer.

Element	A	B	C
	wt%		
Ag	68.07±0.20	11.36±0.12	47.72±0.30
Cu	11.08±0.17	51.12±0.14	19.76±0.17
Zn	15.74±0.13	22.59±0.20	21.54±0.20
Mn	0.42±0.10	2.87±0.17	3.13±0.15
Ni	0.16±0.10	2.75±0.10	2.25±0.10
W	2.05±0.14	3.82±0.17	2.87±0.10
C	1.76±0.10	3.65±0.16	1.68±0.12
Co	0.09±0.04	1.84±0.10	1.05±0.10

SEM-EDX line scan analyses showed that there was an accumulation of Cu towards the interfaces. Cobalt had lower concentration within the interlayer, with an expected increase at the interface. Manganese and nickel showed marginal increases at the interfaces but were more uniform within the interior of the interlayers. EDX maps of other elements are respectively shown in Appendix D.1.

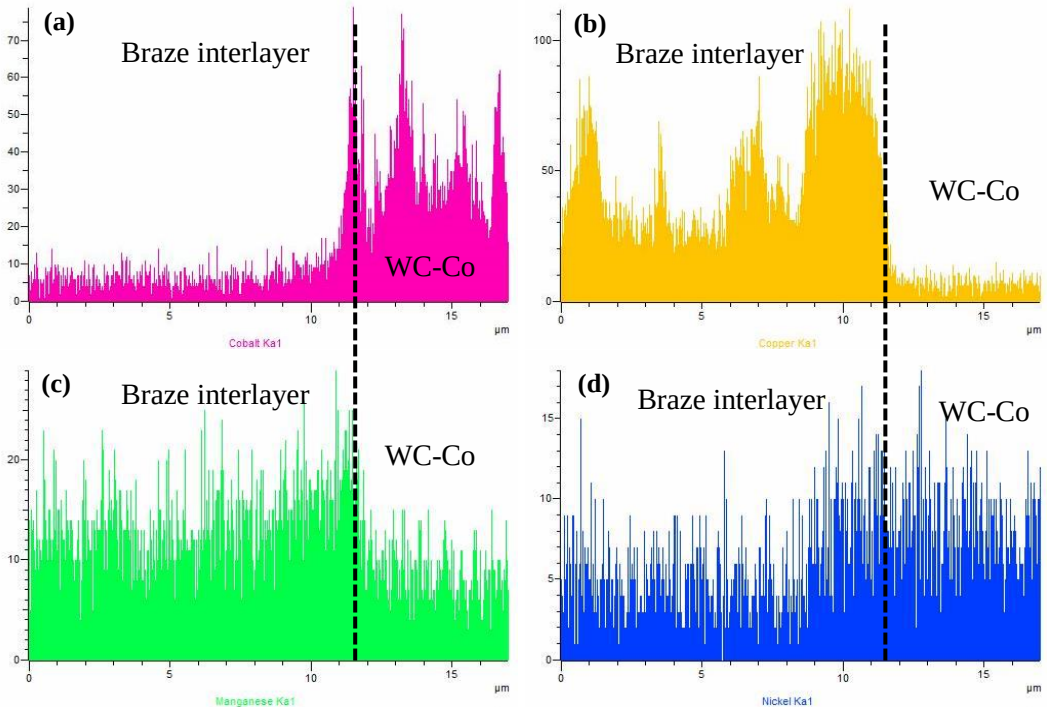

Figure 4.30: EDX line-scanning showing the distribution of (a) Co, (b) Cu, (c) Mn and (d) Ni across a WC-6wt%Co brazed joint with 24 µm filler alloy.

WC-10wt%Co brazed joints consisted of more and enlarged interfacial α-Cu(s.s) phases (region B), Figure 4.31. These interfacial α-Cu(s.s) phases showed a potential to coalesce into band-like phases along the joint interfaces. The EDX analyses of the different phase regions showed that the diffusion of Co into the interlayer decreased towards the centre of the interlayer, Table 4.8.

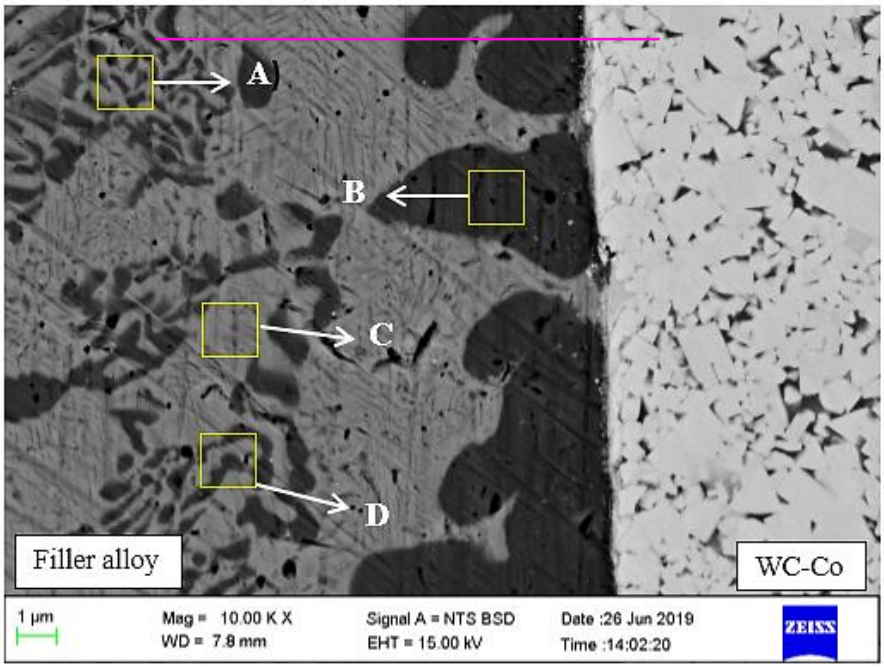

Figure 4.31: SEM-BSD micrograph of the WC-10wt%Co brazed joint at 710°C for 30 s with a 24 µm interlayer.

Table 4.8: SEM-EDX analysis showing chemical composition of 24 µm WC-10wt%Co brazed interlayer.

Element	A	B	C	D
	wt%			
Ag	49.32±0.20	11.04±0.15	62.41±0.18	42.21±0.30
Cu	20.26±0.18	50.17±0.20	12.90±0.18	26.24±0.20
Zn	21.13±0.18	22.60±0.19	17.19±0.15	19.74±0.17
Mn	2.26±0.16	3.75±0.10	1.99±0.12	1.94±0.13
Ni	0.09±0.05	2.41±0.20	-	0.42±0.10
W	3.36±0.12	3.83±0.18	3.18±0.10	3.96±0.16
C	1.74±0.20	4.31±0.13	2.32±0.11	3.83±0.10
Co	1.83±0.20	1.88±0.10	-	1.65±0.11

Figure 4.32 shows that the concentration of Co (a) was marginally uniform within the interlayer, while that of Cu (b) fluctuated but showed an apparent increase towards the interface. Similar to WC-6wt%Co, the concentrations of Mn and Ni showed marginal fluctuations within the interlayer and marginal increases towards the interfaces. EDX maps of other elements are respectively shown in Appendix D.2.

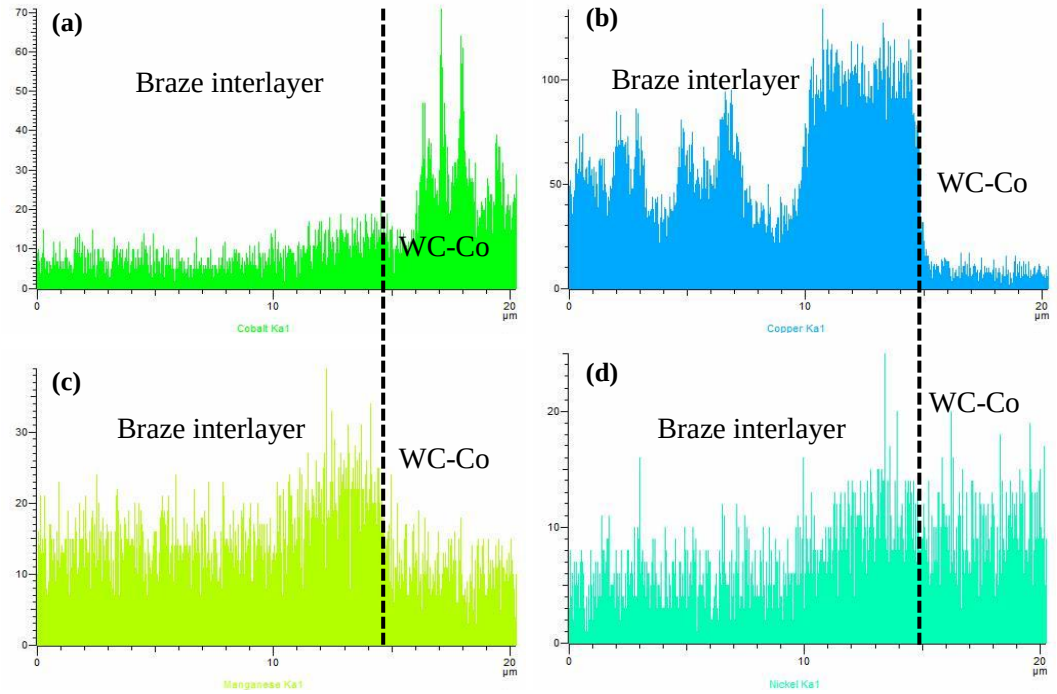

Figure 4.32: SEM-EDX line-scanning showing the distribution of (a) Co, (b) Cu, (c) Mn and (d) Ni across a WC-10wt%Co brazed joint with 24 µm filler alloy.

4.4. Mechanical behaviour of brazed joints

4.4.1. Hardness distributions across the brazed joints

Hardness measurements carried out at an indentation depth of 200 nm across the braze interlayers are shown in Figures 4.33 and 4.34. For both cemented carbide grades, the micro-hardness decreased from the WC-Co base materials into the interior of the braze interlayer. WC-10wt%Co still maintained higher hardness than WC-6wt%Co in accordance with the characterisation in Section 4.1.1.4. A considerable decrease in micro-hardness was observed when going from the WC-Co/braze interfaces towards the interior of the interlayer. Hardness at the WC-Co/braze interfaces was higher than within the interlayers, and this was mainly due to the contribution of the WC-Co base materials and the high hardness of α-Cu(s.s) phases, Figure 4.35. These profiles were used to investigate the mechanical properties of the interfaces and relate them to the bonding energy of each joint.

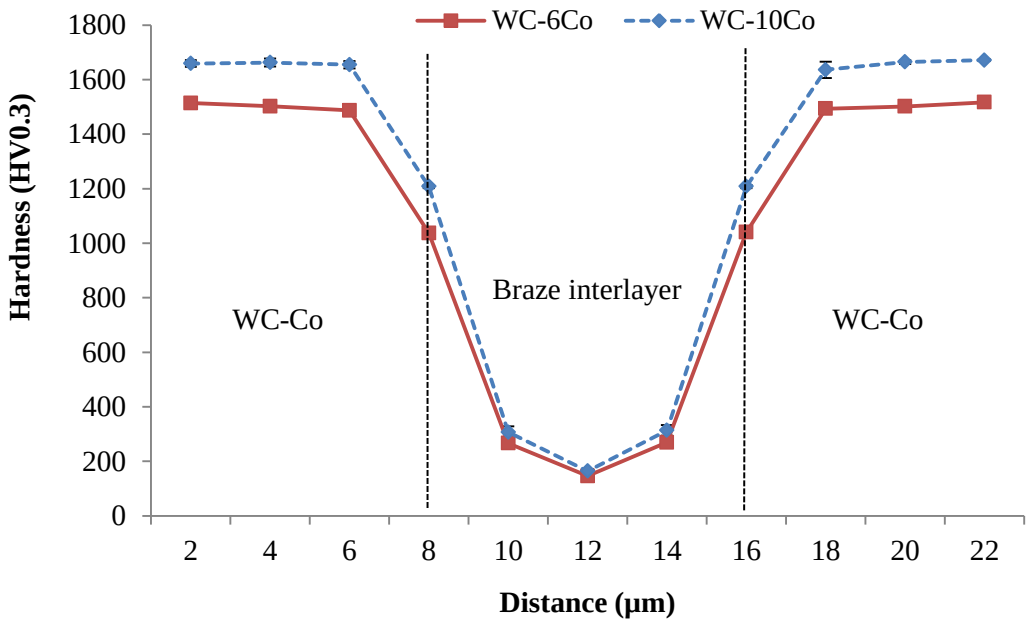

Figure 4.33: Hardness profiles for the 8 µm brazed joints made at 710°C.

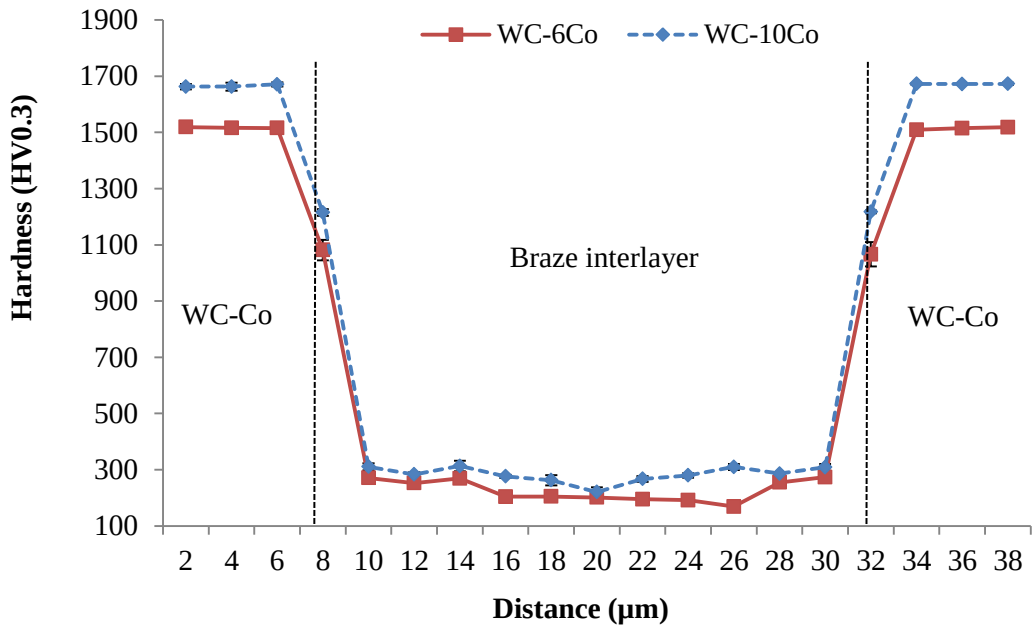

Figure 4.34: Hardness profiles for the 24 μm brazed joints made at 710°C.

The hardness of α-Cu(s.s) phases were higher than that of α-Ag(s.s) phases across all the WC-Co brazed joints. The α-Cu(s.s) phases in WC-10wt%Co brazed interlayers were harder than those in WC-6wt%Co. This showed that the amount of Co that diffused into the interlayers had an influence on the hardness of α-Cu(s.s) phases. There was marginal difference in the hardness of α-Ag(s.s) phases.

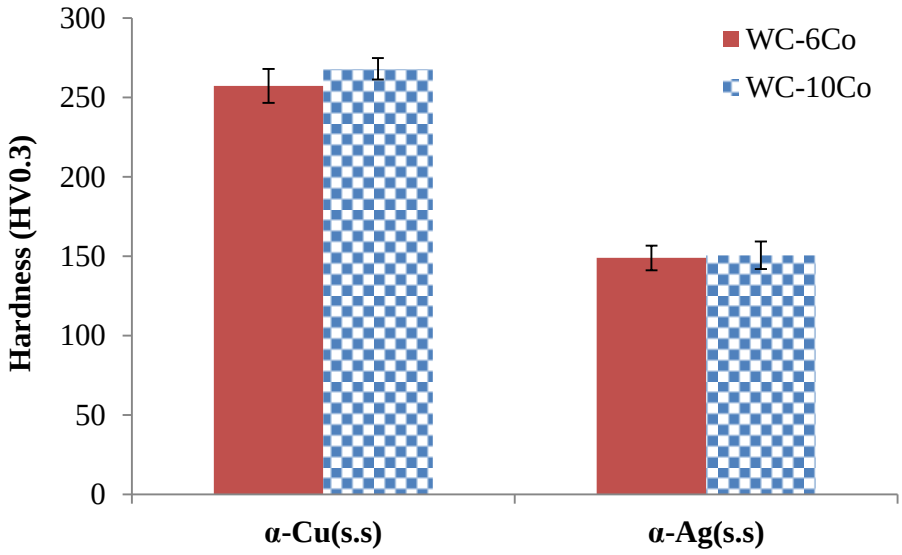

Figure 4.35: Hardness of different interlayer phases for the 8 μm brazed joints made at 710°C.

Figure 4.36 shows that α-Cu(s.s) phases still had higher hardness than α-Ag(s.s) phases when the interlayer thickness was increased to 24 μm . The phases in the interlayers in WC-10wt%Co brazed joints were generally harder than those in WC-6wt%Co. This was with the exception of α-Ag(s.s) which were marginally harder in WC-6wt%Co than in WC-10wt%Co. Overall, the hardness of the phases was ranked from highest as follows: α-Cu(s.s) > Ag-Cu-Zn eutectic > α-Ag(s.s).

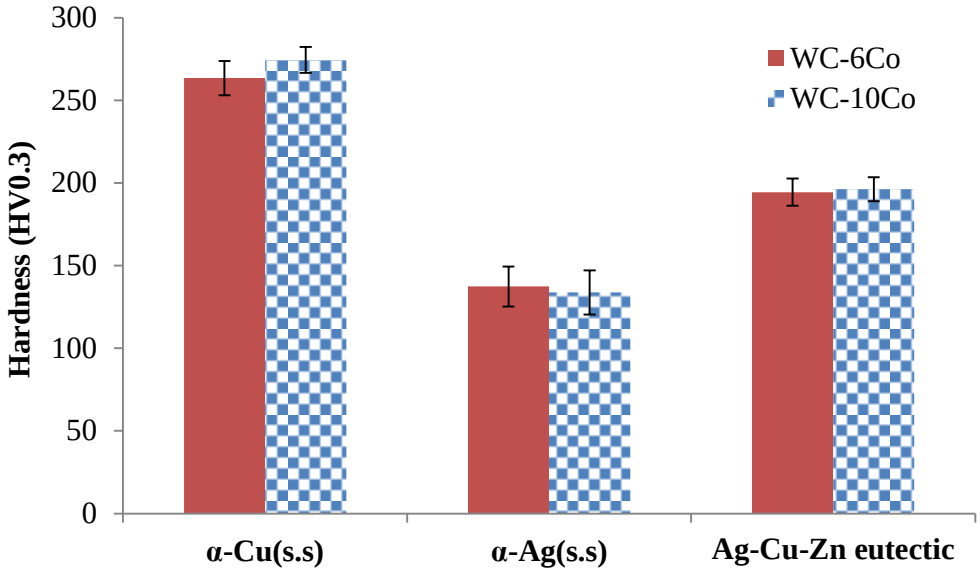

Figure 4.36: Hardness of different interlayer phases for the *24 μm* brazed joints made at 710°C.

4.4.2. Shear strength of brazed joints

Figure 4.37 shows the shear strength variations of the WC-(6 and 10 wt%)Co filler alloy brazed joints with interlayer thicknesses of 8 μm and 24 μm, respectively. It was found that brazed joints with an interlayer thickness of 24 μm had higher shear strength than those with an interlayer thickness of 8 μm. For both interlayer thicknesses, WC-10wt%Co joints had higher shear strengths than WC-6wt%Co brazed joints.

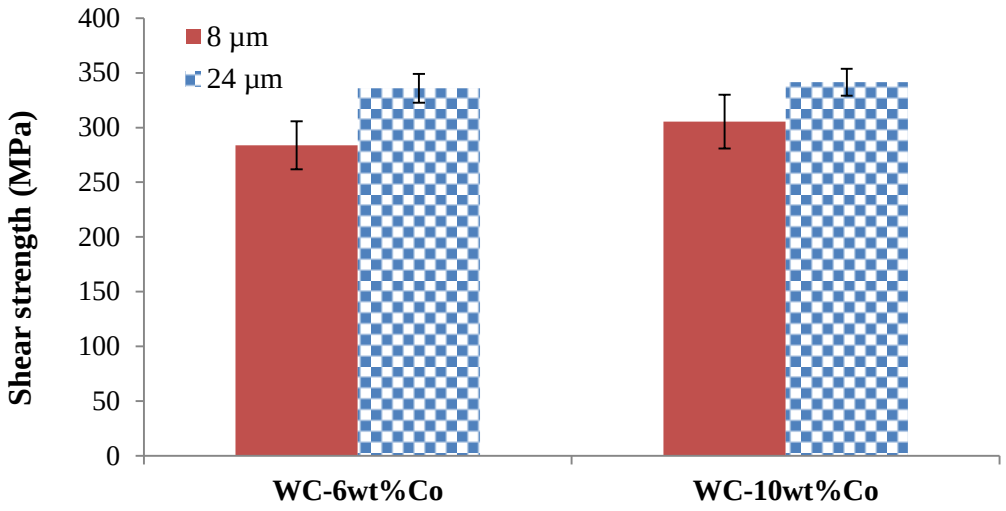

Figure 4.37: Shear strength of the joints brazed with different interlayer thicknesses at 710°C for 30 s holding time at top temperature.

4.4.3. Brazed joints fractography

Figures 4.38 and 4.39 show the fractographs obtained after the shear test for the 24 µm interlayer thickness. Typical ductile fracture modes were observed for both WC-Co alloy grades. The fracture surfaces showed that the failure was preceded by high levels of plastic deformation. This was most prevalent in brazed joints, 4.38. Micro-cracking was also observed on the fractured surface in WC-6wt%Co, Figure 4.38. This suggested that there was a distribution of shear stresses into the base materials.

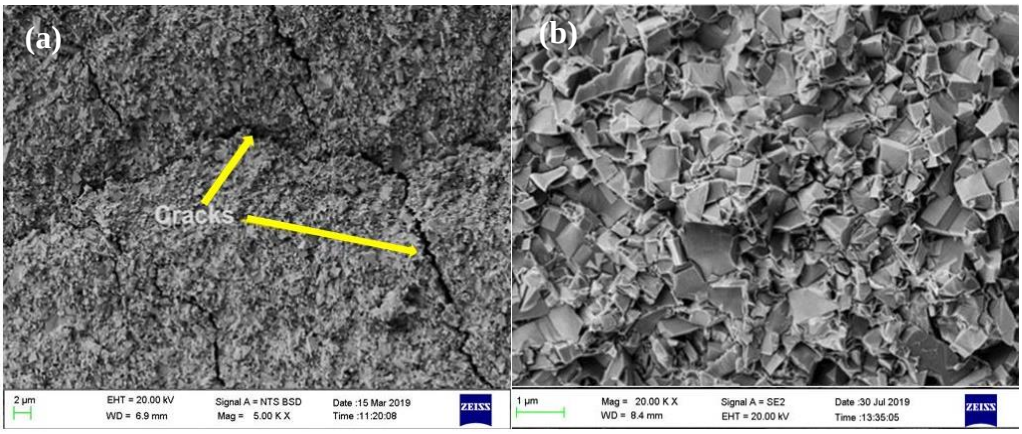

Figure 4.38: Fracture surface morphology of WC-6wt%Co brazed joints fabricated at 710°C for 30 s, with 24 µm interlayer thickness.

Comparatively, WC-10wt%Co brazed joint showed a fracture surface which had a trace of the filler alloy. This showed that WC-10wt%Co brazed joints had good bonding. Overall, the fracture surface had dimples and ridges which exposed WC grains, Figure 4.39 (a).

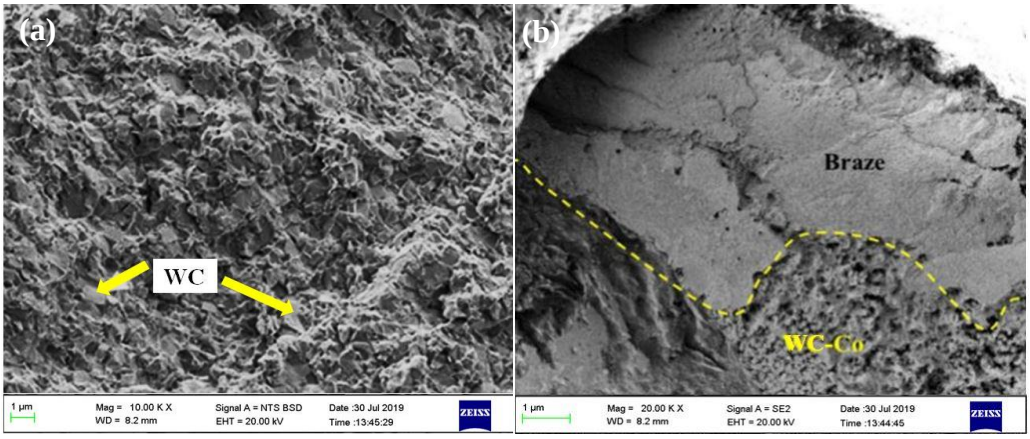

Figure 4.39: Fracture surface morphology of WC-10wt%Co brazed joints fabricated at 710℃ for 30 s, with 24 µm interlayer thickness.

5. DISCUSSIONS

The aim of this research work was to study the brazeability of WC-Co cemented carbides, with different Co binder contents, at common interfaces. This was done by investigating the possibility of oxide formation at the WC-Co/filler alloy interfaces during the brazing process. The research works also studied the effect of filler alloy thickness, and post-braze heat treatment on the evolution of interfacial microstructure and mechanical shear properties of the brazed joints. Oxyacetylene (torch) brazing method was employed to join WC-Co cemented carbides, with cobalt contents 6 wt% and 10 wt%, using a B-Ag49CuZnMnNi filler alloy.

5.1. Microstructural analysis of raw materials

5.1.1. WC-Co cemented carbides

The SEM-BSD micrographs of the WC-Co cemented carbides showed typical microstructures consisting of angular WC grains of various sizes that were cemented in a Co matrix, Figure 4.1 and 4.2. Both the microstructures showed that the WC grains were randomly arranged. As a result, the WC-Co cemented carbides had different mechanical and physical properties, as shown in Section 4.1.1.3. The WC-Co cemented carbides showed a difference in hardness values, and this was ascribed to the variation in Co binder amounts of the sintered materials. The lower hardness value for WC-6Co is due to the increase in wt% of the binder content compared to the WC-10Co sample. WC grain size was similar for both materials (see Table 4.1), thus eliminating the effect of the WC grain size on the hardness values. Hardness values of both WC-Co cemented carbides were typical of the hardness ranges expected for these cobalt contents and WC grain sizes.

The WC-Co specimens showed a difference in the level of porosity, and the porosity levels were characterised according to ISO 4499-4 [92]. Both cemented carbides respectively showed B04 porosity level. There was no A-type porosity, free carbon or eta phase (sub-stoichiometric carbon level) visible in any of the samples examined. The samples had densities, as shown in Table 4.2, which were regarded as acceptable because they were in the typically accepted ranges of the respective WC-Co grades. All the samples were above 98 percent of the theoretically fully sintered materials. This confirmed that the sintering process used to manufacture these samples was efficient as the resultant properties after sintering were typical of the respective carbide grades.

The XRD phase analyses of the WC-Co cemented carbides confirmed the typical constituents, with no undesired phases or the presence of contaminants which could negatively affect the material properties, Figure 4.3. As with the optical microscopy micrographs, no detrimental phases such as the eta (η) phase or free carbon (C) were detected using this methodology. The XRD patterns of all the WC-Co cemented carbides showed the existence of the Co phase in crystalline form.

5.1.2. B-Ag49CuZnMnNi filler alloy

Figure 4.8 shows the SEM-BSD micrograph of the B-Ag49CuZnMnNi (*BrazeTec4900A*) filler alloy. The microstructure consists of a light-grey layered phase (A) rich in Ag, dark-grey layered phase (B) rich in Cu and Zn, and dark-grey spots (D) rich in manganese (Mn) and nickel (Ni). The other light grey phase, marked (C), was found to be rich in Cu (38.01±0.10 wt%), Ag (33.96±0.16 wt%) and Zn (24.26±0.21 wt%). The typical chemical compositions of these phases were measured by carrying out three EDX spot analyses per phase. Representative EDX spectra of these phases are shown in Figures 4.9 - and 4.11. The overall EDX spectrum (Figure 4.9) was used to estimate the chemical composition of the filler alloy. The chemical composition was typical of the supplier specification [89].

The light grey background was identified as α-Ag phases which contained high amounts of Cu (25.05±0.18 wt%) and Zn (21.58±0.20 wt%), while the dark grey patches were α-Cu phases which high amounts of Ag (25.12±0.10 wt%) and Zn (23.97±0.17 wt%). The presence of Ni in the dark grey patches confirmed that it was the α-Cu, because Ni has lower solubility in α-Ag (0.85±0.20 wt%) than in the α-Cu phase (3.00±0.15 wt%). Hence, in the production of the filler alloy, Ni was rejected from α-Ag to preferentially settle and stabilise in was α-Cu phase [81 - 83]. The high content of Cu (38.01±0.10 wt%) and Ag (33.96±0.16 wt%) in the region marked (C) are typical of the phase ,especially given its light grey colour. Regions typical of (C) are evidence that there is an intermediate phase between phases (A) and (B). Hence, it would be interesting to see the evolution of the filler alloy microstructure upon brazing.

The XRD phase analysis of the filler alloy (Figure 4.12) showed the typical filler alloy elements, as provided by the supplier [89], with no undesirable phases or impurities. The results were consistent with the SEM-EDX analysis, were the different elements were detected in each of the phases. The amount of Ni was very small (0.50 wt%) in accordance with the supplier specification sheet [89], and this could be attributed to small intensity peaks of Cu_2NiZn and $Cu_{0.016}Mn_{0.888}Ni_{0.096}$, Figure 4.12. The average Vickers hardness value of the filler alloy was in accordance with the supplier specification, with the measured error being less than 1%.

5.2. Thermal oxidation behaviour of WC-Co cemented carbides

5.2.1. Effect of Co binder content

Figure 4.13 shows the plots of mass gain vs. temperature for WC-6wt%Co and WC-10wt%Co samples oxidised at 400 - 750°C in air for 30, 60, 600, and 1800 seconds, respectively. Thermal oxidation of WC-Co cemented carbides was accompanied by mass gain as a result if the formation of oxide layers. It was observed that the extent of WC-Co oxidation generally increased with increasing temperature. It was clear that increasing the Co binder content in high thermally oxidising atmospheres leads to a decrease in the oxidation of WC-Co components. This indicated that under these conditions, the diffusion of air through the oxide layer was rate controlling. The thermal oxidation behaviour was found to be linear in the temperature range 400 - 500°C and parabolic then after. This showed that substantial oxidation of the samples began at temperatures around 500°C, for both sample types. However, the oxidation behaviour was almost linear for shorter holding times, i.e. 30 and 60 seconds. These results were in concordance with the study carried out by Newkirk [93], which stated that rapid oxidation of WC grains occurred at temperatures as low as 500°C.

WC-6wt%Co showed a higher mass gain than WC-10wt%Co at higher temperatures, for almost all the holding times. Of interest was the thermal oxidation at temperatures around 700°C at different holding times. Figure 4.13 shows that at temperatures above 650°C, both WC-Co sample types showed a rapid mass gain which corresponded to the substantial oxidation of both WC and Co phases. In trying to characterise the effect of Co binder content on the oxidation of WC-Co cemented carbides, the current study focused on the formation of $CoWO_4$ and how this could affect the brazed joint properties. The formation of $CoWO_4$ can occur according to Reactions 5.1 – 5.3 [39, 45]. According to earlier studies [39 - 47], Reaction 5.1 represents the oxidation of the Co phase; Reaction 5.2 represents the oxidation of the Co phase with the diffusion of tungsten from the adjacent WC grains; and Reaction 5.3 represents the oxidation of the Co phase with the adjacent WC phase.

$$\mathrm{Co} + \mathrm{W} + \mathrm{C} + 3O_2 = CoWO_4 + CO_2 \qquad \textit{Equation 5.1}$$

$$\mathrm{Co} + [\mathrm{W}] + 2O_2 = CoWO_4 \qquad \textit{Equation 5.2}$$

$$\mathrm{Co} + \mathrm{WC} + 3O_2 = CoWO_4 + CO_2 \qquad \textit{Equation 5.3}$$

Figure 4.13 clearly shows that Co binder content and thermal oxidation behaviour are inversely correlated, especially at temperatures above 500°C, in complete concordance with the results found by Basu and Sarin [42]. Hence, the higher mass gain in WC-6wt%Co at temperatures above 500°C could be attributed to the formation of higher volumes of the dense $CoWO_4$ phase, as compared to the pore-containing WO_3. The formation of the dense $CoWO_4$ phase in WC-10wt%Co occurred much earlier than in WC-6wt%Co, blocking the pores on the oxide layers. This then slowed down the diffusion of air through the oxide layer to the oxide/substrate interface, leading to a retard in oxidation of WC-10wt%Co samples as shown by the slowing slope in Figure 4.13.

The decrease in oxidation of WC-10wt%Co samples was due to the fact that its early rapid oxidation caused the surface area of the unreacted WC-Co sample to decrease appreciably. This is clearly shown in Figure 5.1, at low oxidation times. In general, both grades were found to be stable and oxidation resistant up to 600°C, but at higher temperatures and longer holding times serious degradation were initiated in the form of oxide layer growth. The growth of the oxide layers was typified by cracking and spalling, Figures 4.14 and 4.15.

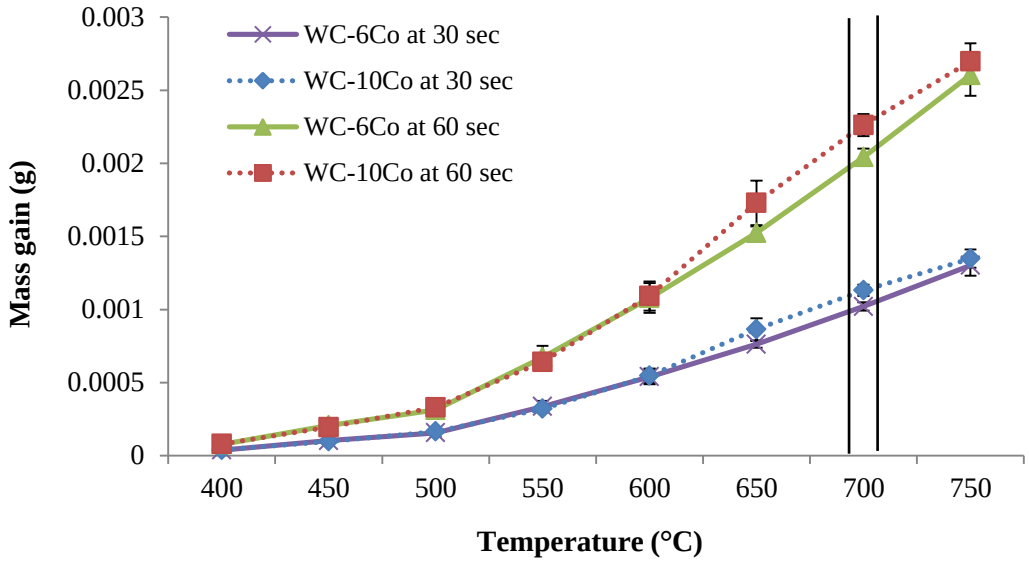

Figure 5.1: Redrawn mass gain versus temperature of WC-Co hardmetals oxidised from 400°C to 750°C, in air for 30 and 60 seconds.

Figures 4.14 and 4.15 show the oxide layer formation on WC-Co samples when oxidised at 700°C at different holding times. With increasing holding time, the oxide layers became thick and dense consisting mainly of mainly of $CoWO_4$ and WO_3 oxides. Oxidised WC-10wt%Co samples showed a clear mixture of WO_3 and $CoWO_4$ oxides much earlier than WC-6wt%Co samples. This phenomenon is shown quite clearly in Figures 4.16 and 4.17. The continued growth of the oxide layers in WC-10wt%Co samples was attributed to the preferential oxidation of the Co binder phase to form $CoWO_4$. This was expected given the Co volume fraction available for oxidation in WC-10wt%Co samples. Whilst the dense $CoWO_4$ retarded the further oxidation of the WC-Co substrate, micro-cracks began to form at 600 seconds holding time and greater.

The formation of micro-cracks on the oxide layers at 1800 seconds was attributed to the high-temperature stresses (due to thermal shock) and the generation of CO_2 and CO at the oxide/WC-Co interface during the oxidation process. Since the generation of CO_2 and CO occurred at the oxide/WC-Co interface, the escape of these gases caused stress at the interface leading to micro-cracking. Micro-cracking and spalling of the oxide layers occurred due to the difference in coefficients of thermal expansion (CTE) between the oxide layers and the WC-Co

substrate materials. For example, the CTE of WO_3 (12×10^{-6}) is about three times that of the WC-6wt%Co materials (4.3×10^{-6}) [32]. Hence, oxide growth at the oxide/substrate interface would take place under compressive stress, and thus the oxide layer will contract more rapidly and separate from the substrate upon cooling. Wang et al. [32] also found that CTE of WC-Co materials strongly depend on the cobalt binder content; hence WC-6wt%Co had less cracking when oxidised at 700°C for 1800 seconds, as compared to WC-10wt%Co.

5.2.2. Phase analysis of oxide layers

Figures 4.20 and 4.21 show the XRD spectrums of the oxide layers that formed on WC-Co samples upon oxidation at 700°C, at different holding times. It is shown that the oxide layers consisted of Co, $CoWO_4$, Co_3O_4, WC and WO_3. At oxidation time of 30 seconds, both cemented carbides grades consisted mainly of WC and Co phases. This showed that at 30 seconds there was insignificant oxidation of the WC-Co substrates. Upon increasing the oxidation to 1800 seconds, the cemented carbides surfaces consisted of $CoWO_4$, Co_3O_4, and WO_3, which confirmed the dual oxidation of WC and Co phases.

At 60 seconds, only WC-10wt%Co showed the presence of $CoWO_4$ and Co_3O_4 in the oxide layers. This confirmed that the Co phase was priori to be oxidised as reported by Bhaumik et al [39] and Chen et al. [45]. The intensity of the WC peaks, on the other hand, decreased with increasing oxidation time owing to the transformation of WC to form WO_3. This phenomenon was observed in both WC-Co alloys. With further increase in oxidation time, the intensity of the WC peaks diminished due to the formation of the dense $CoWO_4$ oxide phase. The dense $CoWO_4$ oxide phases formed a protective layer to the substrates as shown in Figures 4.18 (c & d) and 4.19 (c & d).

The intensities of the $CoWO_4$ peaks, for WC-6wt%Co, at 1800 seconds were higher than those at 600 seconds. Increasing the oxidation holding time led to appreciable oxidation of the Co binder phase in WC-6wt%Co. This was in

concordance with the observation in Figures 4.18 (c) and (d), which showed the growth and coalescence of $CoWO_4$ phases. These $CoWO_4$ phases were porous at 1800 seconds, and thus the further oxidation of the Co binder to form $CoWO_4$ and Co_3O_4 was still permitted. WC-10wt%Co, on the other hand, showed similar peak intensities for $CoWO_4$ at 600 and 1800 seconds. This showed that there was no further apparent oxidation of the Co binder owing to the formation of a considerably thick, protective oxide layer.

Increasing the oxidation time from 600 to 1800 seconds led to an increase in the intensities of WO_3 peaks in WC-6wt%Co. At 1800 seconds, the intensity of the XRD peaks from most intense to less intense was: $CoWO_4 > WO_3 > Co_3O_4$. This confirmed the dual oxidation of the WC grain and the Co binder phase. The oxidation of WC grains was mainly driven by the heat and O_2 diffusion through the porous $CoWO_4$ oxide layer. Comparatively, the XRD spectrum for WC-10wt%Co at 600 and 1800 seconds show that the intensity of WO_3 peaks decreased, with some of the peaks not detected at 1800 seconds. This confirmed that the formation of a protective oxide layer slowed down the further oxidation of WC grains.

5.2.3. Effect of thermal oxidation on WC-Co properties

5.2.3.1. Percentage magnetic cobalt content

Figure 4.19 shows that the percentage magnetic Co of the WC-Co cemented carbides gradually decreased with increasing oxidation time at 700°C. The marginally high reduction in percentage Co in WC-10wt%Co between 0 and 60 seconds was attributed to the preferential oxidation of the Co phase, which was prevalent in WC-10wt%Co than in WC-6wt%Co. This was in concordance with the oxide layer formation in WC-10wt%Co where early formation of $CoWO_4$ was observed, Figure 4.16. WC-10wt%Co showed a slow rate in loss of percentage Co at oxidation times greater than 60 seconds. This was attributed to the formation of the protective $CoWO_4$ oxide scale which slowed the diffusion of O_2 to the oxide/substrate interface.

Magnetic saturation decreases with an increase in the amount of tungsten and carbon that dissolves in the Co binder phase. During the oxidation tests, some tungsten from the base materials formed the oxide scale whilst some diffused and dissolved into the Co binder phase thus decreasing the magnetic saturation. WC-6wt%Co showed a higher loss in magnetic saturation with increasing oxidation time, Figure 4.19. This could mainly be due to the continued thermal oxidation and the delayed formation of the protective $CoWO_4$ oxide layer. Hence, there was continued oxidation of WC grains which may have released tungsten and carbon into the Co binder phase. The formation of the protective $CoWO_4$ oxide scale in WC-10wt%Co worked against the effect of its high coefficient of thermal expansion, which may have increased the tungsten and carbon diffusion into the Co binder phase. The magnetic saturation, however, cannot be clearly related to the weight gain experienced by the samples. This is because complex analysis of chemical reactions that take place during thermal oxidation would need to be carried out to monitor the diffusion of the different elements, including the oxidation products, into the Co binder phase and this equipment was not readily available.

WC-6wt%Co and WC-10wt%Co recorded a decrease of 0.69% and 1.07% at 30 seconds oxidation time, respectively. On one hand, this meant that some trace amounts of Co would diffuse into the interlayer during brazing and thus strengthen the joint strength. On the other hand, the microstructural integrity of the WC-Co base materials would be least compromised as small amounts of Co would be lost. Otherwise, it would be expected that the amount of Co that diffuses into the braze interlayer would be higher in WC-10wt%Co than in WC-6wt%Co brazed joints.

5.2.3.2. Surface micro-hardness

The oxide layers were ground off, very carefully so as not to affect the underlying material, to allow for micro-hardness measurements of the oxidised WC-Co samples. Figures 4.22 and 4.23 show that thermal oxidation led to a general

decrease in surface micro-hardness. The decrease in hardness can be attributed to the oxidation of both the WC grain and the Co binder phase. Marginal growth of the surface WC grains was also observed when the samples were oxidised at 700°C for 1800 seconds, Figures 4.20(d) and 21(d). Both WC-Co grades showed a slight decrease in micro-hardness on the outermost surface, at 30 seconds oxidising time, which was in concordance with the oxide layer formation results presented in Section 4.2.2.1. It was shown that a porous oxide layer was formed due to the partial oxidation of WC and the Co binder phase. Tungsten carbide grains began to substantially oxidise at temperatures around 500°C [82], and this increased with oxidation time. Additionally, the cobalt matrix was also oxidised to form $CoWO_4$. This resulted in a weakened surface microstructure thus the loss in surface hardness.

The micro-hardness distributions also show that the oxidation started on the outermost layer and proceeded to the innermost layers, following a shrinking-core model. This is shown by the general increase in hardness at indentation depths beyond 450 nm. At 700°C and 60 seconds, WC-10wt%Co showed a higher resistance to hardness loss than WC-6wt%Co. The actual reason for this could not be established as WC-10wt%Co recorded a higher mass gain than WC-6wt%Co as seen in Figure 5.1. WC-6wt%Co showed a less resistance to thermal oxidation than WC-10wt%Co when the oxidation time was increased to 600 seconds. This means that surface micro-hardness of WC-6wt%Co samples was mainly governed by the hardness of WC grains. Tungsten carbide (WC) grain in WC-6wt%Co got largely oxidised due to the slow formation of the protective oxide scale. The porous oxide scales on WC-6wt%Co substrates showed the presence of underlying WC grains when oxidised for 600 seconds, Figure 4.15(c). It can thus be inferred that the oxidation of WC grains and the Co matrix during the brazing process could result in a loss of hardness near the brazed joint. Hence, a brazing holding time of 30 seconds was chosen for the brazing tests.

5.3. Brazing behaviour of WC-Co cemented carbides with different Co contents

Brazing can be explained in terms of the reactions that occur at the joint interfaces and the phase changes that take place in the interfacial alloy. The B-Ag49CuZnMnNi filler alloy was allowed to melt and flow into the joint by capillary action upon reaching its melting temperature (690°C). As expected, the filler alloy wet the WC-Co surfaces and formed a braze joint. SEM-BSD micrographs showing the cross-sections of the different joint interfacial microstructures were used to evaluate the brazeability of the different WC-Co cemented carbides.

Brazeability of the cemented carbides was measured by the evolution of the interfacial microstructures with changes in Co content in the WC-Co alloys and the potential to form oxides at the joint interfaces. The joint strength and integrity were also be used to assess the brazeability of the WC-Co materials Interlayer thickness was varied from 8 µm to 24 µm using a Ni630 (VitroBraze) foil with thicknesses of 10 µm and 25 µm, respectively. A small compressive force was applied to the joint to maintain proper alignment of the assemblies. In order to minimise the effect of potential oxidation at the brazed joint interface, for commercial application purposes, holding time of 30 seconds was chosen for the oxyacetylene tests at 710°C. The current study was concerned with the influence of Co content, and thus the thermal conductivity of WC-Co samples, on the interfacial microstructure of oxyacetylene brazed joints. XRD analysis of brazed joints was not performed as the results would not be reliable, given the masking-effect of the filler elements by WC-Co base materials because of the size of the joints. Brazeability of the WC-Co base materials was characterised based on SEM and mechanical tests of the joints.

5.3.1. Brazing of WC-Co with a filler alloy thickness of 8 μm

Figures 4.24 and 4.25 show the SEM-BSD cross-sections of the joints brazed at 710°C for 30 seconds, with a filler alloy thickness of 8 μm. From these micrographs it was observed that successful metallurgical bonding without cracks or voids was achieved. The micrographs also showed that appropriate wetting of the WC-Co surfaces by the filler alloy, and sufficient inter-diffusion of elements under the study conditions, were achieved. Metallurgical reactions and/or diffusion occurred between the filler alloy and the WC-Co composites, resulting in the formation of ribbon-shaped alpha copper solid solution (α-Cu(s.s)) phases along the joint interfaces. The small WC particles found in front of the braze/WC-Co interface and inside the braze interlayer were formed during the metallographic sample preparation steps, i.e. cutting, grinding and polishing. Attachment of WC particles to the braze interlayer was driven by the forces involved during grinding/polishing, and the soft, ductile nature of the braze interlayer in comparison with WC-Co alloys.

The brazed joints contain at least two distinctive regions, i.e. the light grey region and ribbon-shaped dark-grey patches. The light grey region was identified as a silver solid solution (α-Ag(s.s)), and the ribbon-shaped dark-grey patches were identified as α-Cu(s.s). The extent of growth of the dark-grey α-Cu(s.s) patches increased with increasing cobalt content in the cemented carbides. The growth of interfacial α-Cu(s.s) phases was proportional to the size of WC grains. In both brazed joints, there were large dark-grey α-Cu(s.s) islands along the interfaces, and showed growth from the interfaces towards the centre of the interlayers.

The process of solidification played a role in the formation of α-Cu(s.s) islands. The formation of the α-Cu(s.s) islands in the brazed joint occurred during the cooling cycle. The nucleation of the α-Cu crystals started from the cooler surfaces (interlayer/WC-Co interfaces) and propagating towards the centre of the interlayer. This directional solidification of the interlayer was governed by the solubility of cobalt, nickel and copper into each other. The SEM-EDX results show that the Co diffusion into the interlayer decreased towards the centreline of

the braze interlayer. This was mainly due to the migration of Ni towards the interfaces for the purpose of wetting the cemented carbides. Otherwise, Co has good solubility in Ni [61], and controls the thermal conductivity of the WC-Co alloys.

Since the WC-Co materials had similar WC grain sizes, the effect of mean free path on the diffusion of Co into the interlayers could not be established. Instead, the diffusion of Co was controlled by its available amount in the WC-Co base materials. Thus the diffusion of Co was mainly driven by the thermal conductivity of the WC-Co. It was found that increasing the amount of Co binder in WC-Co resulted in an increase in the available Co for inter-diffusion. This consequently led to maximised formation of interfacial α-Cu(s.s) phases. The tendency to form eutectic phases towards the centre of the interlayer suggested a delay in the filler alloy solidification mechanism due to low thermal conductivity. Hence, it was shown that the formation of α-Cu(s.s) phases was governed by both the thermal conductivity of the WC-Co samples and the diffusion of cobalt into the interlayer.
Tables 4.5 and 4.6 show that the amount of cobalt that diffused into the interfacial α-Cu(s.s) phases increased with increasing Co binder content. The amounts of Co that diffused into the interfacial α-Cu(s.s) phases was 1.35±0.08 wt% and 1.57±0.18 wt% for WC-6wt%Co and WC-10wt%Co, respectively. Notwithstanding the varied Co concentration in the interfacial α-Cu(s.s) phases, the amount of Cu that reacted with Co increased with the amount of Co in the WC-Co base materials. Figure 5.2 shows that the reaction regiment between Co and α-Cu decreased when the amount of Co binder in the WC-Co base materials was increased. It is also shown that the amount of Cu in the α-Cu(s.s) phases increased by about 2.39 wt% when the Co binder content was increased from 6 to 10 wt%. This shows that the formation of the dark α-Cu(s.s) phases increased with the amount of Co available for reaction, upon diffusion from the base materials.

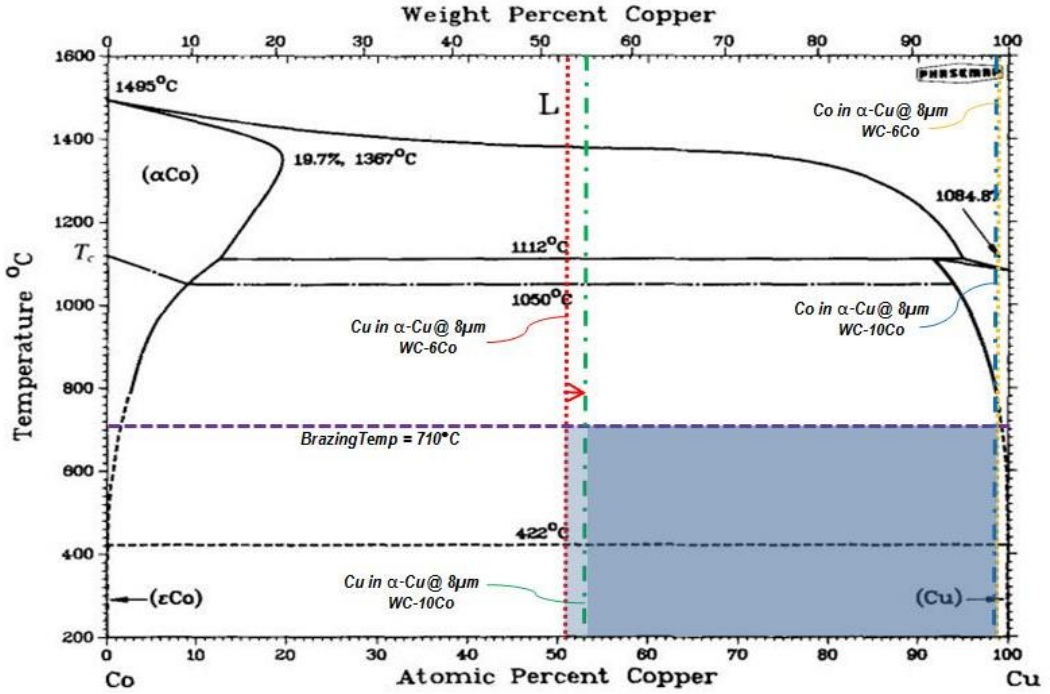

Figure 5.2: Co-Cu phase diagram showing the elemental interaction in the dark interfacial α-Cu(s.s) phases, brazed at 8 μm interlayer thickness (Nishizawa & Ishida, 1984).

Comparatively, the amounts of Co that dissolved in the α-Ag(s.s) phases was very low owing to the low chemical affinity between Co and Ag [15]. Figure 5.3 shows that the lighter α-Ag(s.s) phases in WC-10wt%Co (Figure 4.27) had less Co (0.05±0.02 wt%) than the WC-6wt%Co which had about 0.68±0.12 wt%. It is further shown that when the Co binder in the base materials was increased from 6 to 10 wt% resulted in Co-depleted α-Ag(s.s) phases. This was cause by the preferential of Co in the darker α-Cu(s.s) phases due to its high affinity to Cu than to Ag. Hence, the amount of Ag in the α-Ag(s.s) phases decreased from 71.19±0.22 wt% to 65.38±0.20 wt% when the Co binder content was increased from 6 to 10 wt% in the WC-Co base materials. It is important to note that this process is governed by Co diffusion, which in this case is driven by the amount of Co available for diffusion at the brazing temperature. Overall, this suggested that Co had a significant impact on the formation and solidification mechanism(s) of the α-Cu(s.s) phases than α-Ag(s.s) phases.

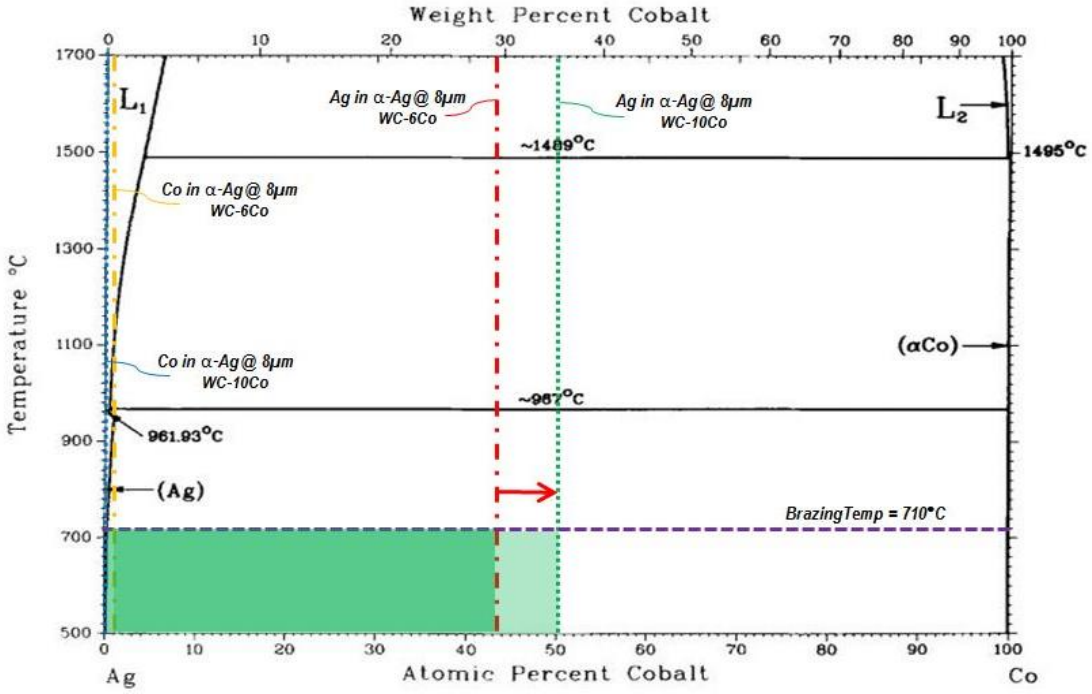

Figure 5.3: Adapted Ag-Co phase diagram showing the elemental interaction in the dark interfacial α-Ag(s.s) phases, brazed at 8 μm interlayer thickness (Karakaya & Thompson, 1986).

SEM-EDX line scan analyses (Figures 4.26. and 4.28) were also carried out across the joint to track the diffusion of elements between the WC-Co base materials and the braze interlayer. It was observed that the concentration of diffused Co decreased from the braze/WC-Co interfaces towards the interlayer centreline, where there were fewer α-Cu(s.s) phases. This showed that there was preferential diffusion of Co into α-Cu(s.s) than into α-Ag(s.s) phases. The α-Ag(s.s) phases, in the interlayers of both WC-Co grades, had high amounts of Zn which was due to the appreciable solubility of Zn in Ag, Figure C.1 (e) in Appendix C.1. Similar observations of high amounts of Zn in the α-Ag(s.s) were made by Jiang et al. [15] and Cheniti et al. [58].

The concentration of Mn and Ni was marginally higher at the braze/WC-Co interfaces than within the interior of the interlayers, in both WC-6wt%Co and WC-10wt%Co. See Figures 4.26 (c & d). and 4.28 (c & d).This was because Mn and Ni possess good solubility in Co [61, 96], hence the accumulation of these elements at the interfaces, and in the interfacial α-Cu(s.s) phases. This further

confirmed the good wetting properties of the filler alloy for WC-Co alloys [89]. Other elemental distributions are shown in Appendix C.1, and it was observed that the amount of W and C that diffused into the interfacial α-Cu(s.s) phases were similar for both grades. This gave an indication that W and C have minimal direct influence on the microstructural evolution of the interlayer, outside of influencing the thermal conductivity of the WC-Co alloys.

5.3.2. Brazing of WC-Co with a filler alloy thickness of 24 μm

In order to study the effect of joint gap size on the microstructural evolution of the braze interlayer and possible interface oxidation, the interlayer thickness was increased to 24 μm. Figures 4.29 and 4.31 show the cross-sectional SEM-BSD micrographs of the joints brazed at 710°C for 30s. Sufficient metallurgical bonding between the filler alloy and the WC-Co samples at a braze thickness of 24 μm, without any structural defects was achieved. Similar to the 8 μm braze joint the formation of ribbon-shaped α-Cu(s.s) phases at the interfaces suggested the occurrence of metallurgical reactions and diffusion during the brazing process. In all the brazed joints, there were fewer large α-Cu(s.s) phases and well developed Ag-Cu-Zn eutectic phases.

The size of the α-Cu(s.s) patches increased with increasing Co binder content of the WC-Co samples. The braze interlayer in WC-10wt%Co had larger α-Cu(s.s) phases in the interlayer than WC-6wt%Co. In both grades, the formation of α-Cu(s.s) phases suggested that the phases formed during the cooling cycle, with the nucleation starting from the interfaces and growing towards the centre of the interlayer. The formation of darker α-Cu(s.s) phases was influenced by the diffusion of cobalt, as previously discussed in Section 5.3.1. Figure 5.4 shows that at an interlayer thickness of 24 μm the immiscibility of Co into the α-Cu solution increased when the WC-Co cobalt grade increased from 6 to 10 wt%. Increasing the filler gap between the WC-Co surfaces to 24 μm was equivalent to increasing the diffusion path. Hence, it could then be predicted that less inter-diffusion occurred hence the formation of some interfacial eutectic phases. This

phenomenon was most prevalent in WC-6wt%Co. The amount of Co in α-Cu(s.s) phases increased when the Co binder content was increased from 6 to 10 wt%, but overall decreased when the diffusion path was increased by increasing the interlayer thickness to 24 µm. Otherwise, the brazed interlayer in WC-10wt%Co still had more α-Cu(s.s) phases at the interfaces than in WC-6wt%Co brazed joints. This shows that the Co binder content of WC-Co materials can thus be used to predict their brazing behaviour for Ag-based filler alloys containing copper.

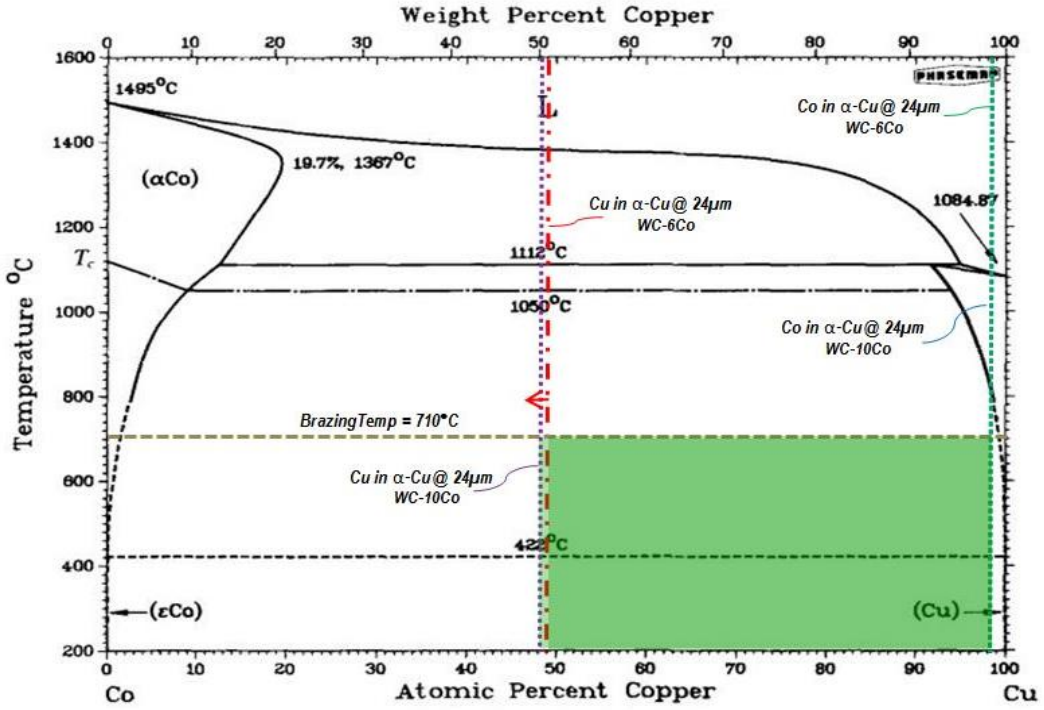

Figure 5.4: Adapted Ag-Co phase diagram showing the elemental interaction in the dark interfacial α-Cu(s.s) phases, brazed at 24 µm interlayer thickness (Nishizawa & Ishida, 1984).

The cross-sectional SEM-BSD of the brazed joints suggested that the growth of the α-Cu(s.s) phases was as a result of the coalescence of the Ag-Cu-Zn eutectic phases. The braze interlayer in WC-6wt%Co joints showed arranged eutectic phases and fewer interfacial α-Cu(s.s) phases. And, the formation of these micro-sized, needle-like eutectic phases suggested that nucleation and growth was from the interfaces towards the interior of the interlayers. Jia et al. [82] suggested that the addition of about 20 wt% Zn in the filler alloy could decrease the eutectic

temperature to 675°C hence the formation of eutectic phases at the 700°C braze temperature. Hence, the Zn content in the filler alloy [89], coupled with an increase in the interlayer thickness, could be said to have promoted the formation of the eutectic phases.

EDX analyses were also done to further monitor the inter-diffusion or the accumulation of elements at the interfaces. Figures 4.30 – 4.32 show the EDX line-scans obtained for the different elements. It was observed that there was an accumulation of Cu towards the braze/WC-6wt%Co interfaces. This could be explained by its appreciable solubility in Co, which showed high concentration at the interface. Hence, the dark interfacial α-Cu(s.s) phases had high Co which contributed in their formation process. Similarly, WC-10wt%Co brazed joints showed a marginally uniform concentration of Co within the interlayer, Figure 32 (a), while that of Cu fluctuated but showed an apparent increase towards the interface, Figure 32 (b). The α-Ag(s.s) and eutectic phases were also found to contain appreciable amounts of Co.

Manganese and nickel showed marginal increases at the interfaces but were more uniform within the interior of the interlayers. This supported the claim that Mn and Ni played a wetting role of the filler alloy onto the WC-C surfaces. The filler alloy had good wetting properties due to the presence of nickel in the interfacial α-Cu(s.s) phases. Chen et al. [61] found that the accumulation of Mn andNi at the interfaces reduced the stresses caused by cooling and could actually strengthen the brazed joint. Hence, successful metallurgical bonding between the filler alloy and the WC-Co cemented carbides was achieved. EDX maps of other elements are respectively enclosed in Appendix D.

5.4. Mechanical behaviour of brazed joints

5.4.1. Hardness distribution across brazed joints

The micro-hardness distributions across the brazed joints for different interlayer thicknesses are shown in Figures 4.33 and 4.34. Both distributions show that the

hardness decreased when going from the WC-Co/braze interface line towards the interior of the braze interlayer. For the 8 μm interlayer, the hardness at the WC-Co/braze interfaces was around 1039±7 HV and 1208±6 HV for WC-6wt%Co and WC-10wt%Co, respectively. The hardness values were higher than those in the interior of the braze owing to the dual hardness contribution of the WC-Co base materials and interfacial α-Cu(s.s) phases.

The hardness in the interior of the braze was mainly controlled by the distribution of α-Cu(s.s) phases which had high hardness compared to α-Ag(s.s) phases, Figure 4.35. These α-Cu(s.s) phases were found to contain higher amounts of diffused Co (1.35±0.08 wt% for WC-6wt%Co and 1.57±0.18wt% for WC-10wt%Co), which was attributed to the appreciable solubility of cobalt in copper [61]. Hence, the inter-diffusion of Co into the braze interlayer could be said to have strengthening effect of the α-Cu(s.s) phases. In addition, the hardness curves corresponding to WC-6wt%Co and WC-10wt%Co exhibited maximum hardness peaks of about 1514 HV and 1662 HV, respectively. These hardness values were slightly lower than those of the un-brazed materials, i.e. 1518±10 HV for WC-6wt%Co and 1676±15 HV for WC-10wt%Co. This can be related to the slight WC rearrangement as a result of Co diffusion and thermal shock during the brazing process.

Figure 4.34 shows that there was a slight increase in micro-hardness of the braze interlayer when the interlayer thickness was increased to 24 μm. This was attributed to the formation of the Ag-Cu-Zn eutectic phases which had higher hardness than the α-Ag(s.s) phases, Figure 4.35. The high hardness of the Ag-Cu-Zn eutectic phases was probably due to the ductile nature of the elements present, coupled with the diffusion of Co in these phases. The amount of Co that diffused into the Ag-Cu-Zn eutectic phases which formed in WC-6wt%Co and WC-10wt%Co were 1.05±0.10 wt% and 1.83±0.20 wt%, respectively. This showed that the inter-diffusion of Co also played a role in the formation of these eutectic phases.

In comparison to the 8 μm interlayer joints, a strong increase in hardness was observed at the 24 μm braze/WC-Co interface. Hardness values of about 1066 HV and 1218 HV were achieved for braze/WC-6wt%Co and braze/WC-10wt%Co, respectively. This could be attributed to two factors: (1) the presence of high concentration of α-Cu(s.s) phases in this region, and the high diffusion of Ni from the braze interlayer and Co from WC-Co towards the braze/WC-Co interface. Lee et al. [10] and Jiang et al. [15] reported that the presence of these elements at the braze/WC-Co interface causes a strong increase in hardness. It was also observed that the hardness in the braze interlayer closer to the WC-Co base materials was higher in WC-10wt%Co than in WC-6wt%Co. This was attributed to the large range diffusion of Ni and Co from the Ni-insert and the WC-10wt%Co base materials, respectively. WC-10wt%Co samples still maintained their high hardness despite the high amounts of diffused Co from the base materials into the braze interlayer.

5.4.2. Shear strength

Figure 4.37 shows the variation in the shear strengths of WC-Co brazed joints obtained using B-Ag49CuZnMnNi filler alloy with a filler alloy thickness of 8 μm and 24 μm, respectively. The supplier found shear strength of 250 - 300 MPa for carbide-to-steel brazed joints [89]. The results showed that the different WC-Co grades can be well brazed at a common interface using Ag-based filler alloy at a brazing temperature of 710°C, with 30 seconds holding time. For a filler alloy thickness of 8 μm, the maximum shear strengths achieved were 284±15 MPa and 336±13 MPa for WC-Co cemented carbides with Co contents of 6 wt% and 10 wt%, respectively.

Comparatively, higher shear strengths were achieved for joints brazed with a filler alloy thickness of 24 μm. WC-6wt%Co and WC-10wt%Co reached maximum shear strengths of 305±12 MPa and 341±15 MPa, respectively. This evolution is in good accordance with the results of the nano-indentation testing presented in Section 5.4.1. It is suspected that further increasing the interlayer thickness and

holding time may lower the shear strength due to thermally activated stresses and the effect of oxidation.

The joint shear strengths generally increased with increasing the amount of available cobalt (Co binder content) for diffusion. The SEM-BSD brazed joint cross-sections in Section 4.3 showed that the formation and development of the interfacial α-Cu(s.s) phases was promoted by increasing cobalt content of the WC-Co base materials. The formation of eutectic and α-Cu(s.s) phases increased with increasing interlayer thickness from 8 to 24 µm, Figures 4.29 and 4.31. This resulted in an overall increase in the shear strength of the joints.

The quantity of α-Cu(s.s) phases and their distribution within the interlayers had a great influence on the shear strengths of the WC-Co brazed joints. The α-Ag(s.s) phases had good plasticity [15], whilst the α-Cu(s.s) phases enhanced the strength of the joints. For the interlayer thickness 8 µm interlayer thickness, the maximum micro-harness of the α-Cu(s.s) phases in WC-6wt%Co and WC-10wt%Co were 257±11 HV and 268±7 HV, respectively. The lower hardness in WC-6wt%Co was attributed to the slow homogenisation of α-Cu(s.s) phases as they contained some undeveloped traces of α-Ag(s.s) phases, Figure 4.25. Hence, the high standard deviation (11 HV) in the α-Cu(s.s) phases of WC-6wt%Co brazed joints. The hardness of the α-Ag(s.s), on the other hand, was lower at 149±8 HV and 151±9 HV for WC-6wt%Co and WC-10wt%Co, respectively. There was marginal difference in the hardness of α-Ag(s.s) phases between the two grades, showing that the formation of the α-Ag(s.s) phases is not Co dependant.

Increasing the interlayer thickness to 24 µm led to the redistribution of these phases, with the formation of Ag-Cu-Zn eutectic phases. Again, the micro-hardness of the different phases was measured, and there was a general increase in hardness across the identified phases. The micro-hardness of the of the α-Cu(s.s) phases were 264±10 HV and 275±8 HV, for WC-6wt%Co and WC-10wt%Co, respectively. This was followed by the Ag-Cu-Zn eutectic phases at 195±8 HV and 196±7 HV, and α-Ag(s.s) phases at 137±12 HV and 134±13 HV for WC-6wt%Co and WC-10wt%Co, respectively.

Attributed to the higher hardness of the α-Cu(s.s) phases, which enhanced the strength of the braze joints, was the increased inter-diffusion of Co and Ni during the formation of α-Cu(s.s) phases. This was shown by the decrease in hardness of the α-Ag(s.s) phases, which had decreased amounts of diffused Co and Ni, Tables 4.7 and 4.8. Hence, α-Cu(s.s) and Ag-Cu-Zn eutectic phases that formed in the braze joints with a filler alloy thickness of 24 μm could be said to have a dispersion strengthening effect. Jiang et al. [15] found that the dispersion strengthening effect of α-Cu(s.s) weakened with an increase in the size of α-Cu(s.s) phases. This was in concordance with the results in the current study which showed an increase in the amount of interfacial α-Cu(s.s) phases. Otherwise, the brazed joints with a filler alloy thickness to 8 μm achieved lower shear strength due to enlarged interfacial α-Cu(s.s) phases.

The dual diffusion of manganese and nickel into the interfacial α-Cu(s.s) phases also enhanced the strength of the joints. The enriched content of Mn and Ni in these α-Cu(s.s) phases assisted in reducing the residual stresses [53, 61] that may have been caused by the rapid cooling inherent to oxyacetylene brazing. Otherwise, joints with no structural defects such as voids and cracks were consistently obtained for both interlayer thicknesses. Therefore, it can be deduced that the mutual solubility of manganese and nickel into cobalt, as shown by the EDX line-scans in Section 4.3, also enhanced the joints strength.

It was generally assumed that thinner braze interlayers offer better shear strength [53], however, the current study has shown that an interlayer thickness of 24 μm can achieve higher shear strengths than the 8 μm. Willingham [97] observed that thinner filler alloy can provide better capillary action at the joint interface. Hence, it would be important to explore interlayer thicknesses higher than 24 μm to determine the point at which the shear strength may drop. It is suspected that beyond a particular interlayer thickness, the joint shear strength may also start to decrease as a result of the changes in interlayer microstructure. Hence, brazing conditions that lead to the formation of interfacial microstructures which consists

of dispersed α-Cu(s.s) and Ag-Cu-Zn eutectic phases are desirable, due to their strengthening effect.

5.4.3. Brazed joints fractography

The fractographs obtained after the shear tests for the WC-6wt%Co and WC-10wt%Co brazed joints, with 24 μm thick interlayer, are respectively shown in Figures 4.38 and 4.39. In both cases, the fracture surfaces illustrated a ductile fracture mode, which showed that before failure there was high amounts of plastic deformation. WC-6wt%Co brazed joints exhibited the presence of dimples and micro-cracks which indicated ductile fracture. Since the braze interlayer contained fewer α-Cu(s.s) and Ag-Cu-Zn eutectic phases, this means the α-Ag(s.s) phases were the determining factor in the shear failure of WC-6wt%Co brazed joints.

Wang et al. [14] and Jang et al. [15] reported that α-Ag(s.s) phases cannot duly sustain shear stresses and would thus act as fracture initiation points, with the potential of transferring the stresses to the base materials. This was observed in the current study with the formation of micro-cracks in the WC-6wt%Co base materials, Figures 4.38 (a). The lower shear strength values for WC-6wt%Co brazed joints can be attributed to the interlayer microstructures and the more rapid transfer of shear stresses to the WC-Co base materials.

Figure 4.39 (a) shows that WC-10wt%Co brazed joints had a mixture of ductile and brittle fracture modes, showing the presence of dimples and cleavage regions exposing WC grains. This could be clearly seen in Figure 4.39 (b) where failure occurred in the region of the braze interlayer close to the WC-Co base materials. The mixed fracture mode gave a good indication that WC-10wt%Co had good metallurgical bonding with the B-Ag49CuZnMnNi filler alloy under the brazing conditions investigated. This was in concordance with the shear strength results discussed in Section 5.4.2.

The ductile fracture mode is clearly illustrated in Figure 4.39 (b) with the part of the braze interlayer still attached to the WC-Co base material. Here, the fracture occurred from within the braze interlayer to the WC-Co hence the brittle fracture in the WC-Co base material. The braze interlayers consisted of larger α-Cu(s.s) phases and well-dispersed Ag-Cu-Zn eutectic phases. This resulted in higher shear strength owing to the dual contribution of the braze interlayer and the WC-10wt%Co. From a maintenance perspective, this mixed fracture mode would be desirable as less WC-Co base material is lost and the failure could be detected much earlier.

5.5. Assessing the brazeability of WC-Co cemented carbides

Brazeability of the cemented carbides was measured by the evolution of the interfacial microstructures, the joint integrity and the potential of oxide formation at the interfaces, with changes in Co content in the WC-Co base materials. Good metallurgical bonding, free of defects such as cracks or voids, between the filler alloy and WC-Co alloys was achieved. See Section 4.3. Analysis of the brazed joint cross-sections showed that there was no apparent oxide formation at the interfaces. Instead, the inter-diffusion of elements between the filler alloy and the WC-Co base materials occurred. The main element (Co) responsible for oxide layer formation diffused into the interlayer, playing a great role in the formation of α-Cu(s.s) phases. Figure 5.2 shows a schematic representation of the phenomenon of oxide layer formation and inter-diffusion. Since it was shown that there is minimal oxidation at 30 seconds, potential oxides that could form at the interfaces could be at a nano scale, making it difficult to be properly detected and analysed using normal SEM. Instead, other techniques such as variable-pressure SEM, atomic-force microscopy and laser-scanning confocal microscopy, which could not be accessed, could be used to analyse nano-scale oxides.

Increasing the Co amount in WC-Co alloys led to increased amounts and sizes of α-Cu(s.s) phases in the braze interlayers. Hence, the brazed interlayers in WC-10wt%Co had more α-Cu(s.s) phases than in WC-6wt%Co. Solidification of the α-Cu(s.s) phases was influenced by Co, Ni and Mn, which played a great role in

the wetting characteristics of the filler alloy. This was largely driven by the high affinity between Co and Ni. The number of α-Cu(s.s) phases gave an indication of good joint formation. WC-10wt%Co brazed joints showed a prevalence of this phenomenon; further suggesting that WC-10wt%Co was more brazeable than WC-6wt%Co for both interlayer thicknesses.

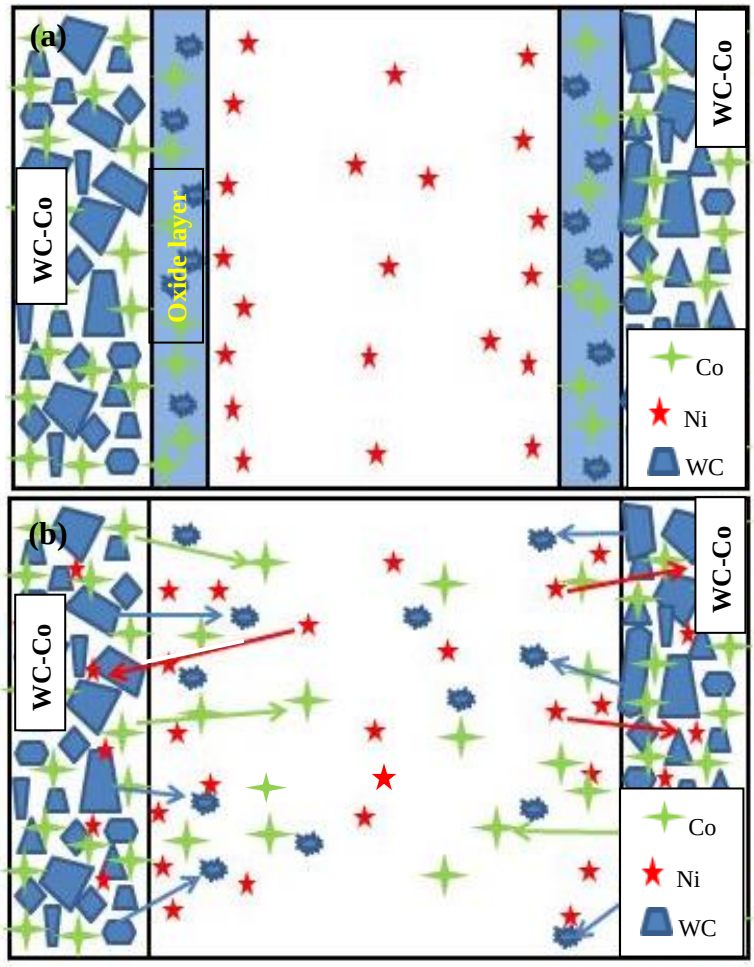

Figure 5.52: Schematic diagram showing (a) oxide layer formation at the interface, and (b) inter-diffusion of Co, WC and Ni.

WC-6wt%Co brazed joints still showed good potential. Interfacial microstructures at 24 μm suggested that WC-6wt%Co could have improved microstructure with considerable process changes such as longer holding times and higher brazing temperatures. This is owing to the formation of well dispersed α-Cu(s.s) and Ag-Cu-Zn eutectic phases in the brazed interlayer. However, careful considerations would need to be taken to keep the potential for oxide formation at a minimum.

The shear strength results were acceptable (within the supplier specifications [89]) and corresponded with the brazed interlayer microstructures. And, it was shown that WC-10wt%Co achieved higher shear strength than WC-6wt%Co in both interlayer thicknesses. This was mainly due to the increase in the size and amount of the ductile α-Cu(s.s) phases which had a dispersion strengthening effect. Fractographic investigations revealed that WC-6wt%Co showed a ductile fracture mode while WC-10wt%Co showed a mixture of ductile and brittle fracture modes.

6. CONCLUSIONS

The conclusions from this research study include the following:

1. Oxidation, measured by the weight gain, increased significantly with temperatures above 600°C and with a decrease in Co content, to form oxide layers mainly containing WO_3 and $CoWO_4$, and traces of Co_3O_4. WC-6wt%Co recorded the highest reduction in Vickers hardness than WC-10wt%Co after oxidation owing to increased dual oxidation of WC grains and the Co binder to respectively form WO_3 and $CoWO_4$, and the minimal tendency to form a protective oxide layer.

2. The quality of brazed joints, measured in terms of the amount and size of interfacial α-Cu(s.s) phases, showed an improvement with the increase in Co content of the WC-Co alloys. Instead of interfacial oxide formation, there was distinguishable inter-diffusion of metallic elements across the braze/WC-Co interfaces.

3. Interlayer thickness of 8 μm showed the formation of large α-Cu(s.s) phases with increasing Co content in WC-Co alloys. Joints with an interlayer thickness of 24 μm showed an improvement in brazed joint quality due to the formation of hard α-Cu(s.s) and Ag-Cu-Zn eutectic phase structures.

4. The joint shear strengths increased with an increase in interlayer thickness from 8 to 24 μm. Shear strength was shown to be largely dependent on the dispersion strengthening effect of α-Cu(s.s) phases, which were widely distributed throughout the interlayer microstructure, in particular at an interlayer thickness of 24 μm. Upon shear tests, WC-6wt%Co showed a ductile-to-brittle fracture mode while WC-10wt%Co showed a mixture of ductile and brittle fracture modes.

7. RECOMMENDATIONS

Potential future studies, originating from this research:

1. The current research was based on cemented carbides with cobalt as the only binder phase material. Different WC-Co grades, with Ni binder or binder strengthening material additions, such as NbC or TiC can be used to further study their surface oxidation.

2. Comparative studies on the brazeability of WC-Co cemented carbides, measured by the formation of oxides in the interlayer, of the different Co grades and WC grain size, using longer holding times and Ag-based filler alloys with an added Co content.

3. Investigating the effect of longer brazing holding time, larger braze joint thicknesses, and post-braze heat treatments on the possible evolution of the interlayer microstructure using Ag and Cu-based filler alloys.

8. REFERENCES

[1] P. Schwarzkopf, Powder Metallurgy: Its Physics and Production, Macmillan, New York, 1947.

[2] G. S. Upadhyaya, Cemented Tungsten Carbides: Production, Properties, and Testing, New Jersey: Noyes Publications, 1998.

[3] H. Exner, "Physical and chemical nature of cemented carbide," *International Matals Reviews*, vol. 243, no. 4, pp. 149-173, 1979.

[4] G. Q. Shao, X. L. Duan, J. R. Xie, X. H. Yu, W. F. Zhang and R. Z. Yuan, "Sintering of nanocrystalline WC-Co composite powder," *Reviews on Advanced Materials Science*, vol. 5, no. 4, pp. 281-283, 2003.

[5] A. Upadhyaya and D. W. G. Sarathy, "Advances in sintering of hard metals," *Material Design*, vol. 22, no. 6, pp. 499-506, 2001.

[6] British Geological Survey (BGS), "World Minerals Statistics - Risk List 2015," 2015. [Online]. Available: http://www.bgs.ac.uk. [Accessed 20 February 2019].

[7] I. Northrop, "The joining of tungsten carbide hardmetal to steel," *Journal of the South African Institute of Mining and Metallurgy*, vol. 87, no. 5, pp. 125-135, 1987.

[8] J. Bosch, *The effects of brazing on cemented tungsten carbide*, Johannesburg: University of the Witwatersrand, 1965.

[9] C. Barbatti, J. Garcia, G. Liedl and A. Pyzalla, "Joining of cemented carbides to steel by laser beam welding," *Materials Science and Engineering Technology*, vol. 38, no. 11, pp. 907-914, 2007.

[10] W. Lee, B. Kwon and S. Jung, "Effect of bonding time on joint properties of vacuum brazed WC-Co hard metal/carbon steel using stacked Cu and Ni alloy as insert metal," *Materials Science Technology*, vol. 20, no. 11, pp. 1474-1478, 2004.

[11] L. Chiu, H. Wang, C. Huang, C. Hsu and T. Chen, "Effect of brazing temperature on the microstructure and property of vacuum brazed WC-Co and carbon steel joint," *Advanced Materials Research*, vol. 47, pp. 682-

685, 2008.

[12] Y. Li, Z. Zhu, Y. He, H. Chen, C. Jiang, D. Han and J. Li, “WC particulate reinforced joint by ultrasonic-associated brazing of WC-Co/35CrMo,” *Journal of Materials Processing Technology*, vol. 238, pp. 15-21, 2016.

[13] C. Jiang, H. Chen, X. Zhao, S. Qiu, D. Han and G. Gou, “Microstructure and mechanical properties of brazing bonded WC-15Co/35CrMo joint using AgNi/CuZn/AgNi composite interlayers,” *International Journal of Refractory Metals and Hard Materials*, vol. 70, pp. 1-8, 2018.

[14] H. Wang, D. Yang, X. Zhao, C. Chen and Q. Wang, “Microstructure and bend strength of WC-Co and steel joints,” *Science and Technology of Welding and Joining*, vol. 10, no. 2, pp. 167-168, 2005.

[15] C. Jiang, H. Chen, Q. Wang and Y. Li, “Effect of brazing tempearature and holding time on joint properties of induction brazed WC-Co/carbon steel using Ag-based alloy,” *Journal of Materials Processing Technology*, vol. 229, pp. 562-569, 2016.

[16] K. Brookes, Hardness and Other Hard Materials, 3rd ed., International Carbide Data, 1998.

[17] K. Brookes, World Directory and Handbook of Hardmetals, 2nd ed., Engineers' Digest Publication, 2001.

[18] J. L. Prakash, “Application of fine grained tungsten carbide based cemented carbides,” International Journal of Refractory Metals & Hard Materials, vol. 13, no. 5, pp. 257-264, 1995.

[19] G. Spriggs, “A history of fine grained hardmetal,” *International Journal of Refractory Metals and Hard Materials*, vol. 13, no. 5, pp. 241–255, 1995.

[20] U. Beste and S. Jacobson, “A new view of the deterioration and wear of WC/Co cemented carbide rock drill buttons,” *Wear*, vol. 264, no. 1-2, pp. 1129–1141, 2008.

[21] J. T. Black and R. A. Kohser, DeGarmo's Materials and Processes in Manufacturing, 12th ed., Hoboken, NJ: John Wiley & Sons, Inc., pp. 320-321, 2017.

[22] S. Luyckx, *The hardness of tungsten carbide-cobalt hardmetal in: Riedel, R.*, vol. 2, WILEY-VCH, pp. 946-964, 2000.

[23] R. M. German, Sintering Theory and Practice, New York: John Wiley & Sons Inc, 1996.

[24] S. Luyckx, "The Preparation and Properties of Hardmetals," (University of the Witwatersrand Course Literature), Sandvik, 1997.

[25] D. O'Quigley, *The properties and relationships between properties of a wide range of WC-Co hardmetals*, Johannesburg: University of the Witwatersrand, 1996.

[26] X. Han, *On the plastic deformation of WC-Co alloys at high temperature*, Johannesburg: University of the Witwatersrand, 2006.

[27] J. Martin, Materials science for engineering, the institute of materials, 1996.

[28] J. Gurland, "Microstructural aspects of the strength and hardness of cemented tungsten carbide.," in *Conference on Materials for Metal Cutting*, 1970.

[29] ISO Standard, Hardmetals - Metallographic determination of microstructure - Part 4: Characterisation of porosity, carbon defects and eta-phase content, 2016.

[30] ASTM, Standard Test Method for Apparent Porosity in Cemented Carbides, ASTM International, 2015.

[31] K. Chang-Soo, "Microstructural-Mechanical Property Relationships in WC-Co composites," PhD Thesis, Materials Science and Engineering Department, Carnegie Mellon University, Pittsburgh, 2004.

[32] H. Wang, T. Webb and J. W. Bitler, "Study of thermal expansion and thermal conductivity of cemented WC–Co composite," *International Journal of Refractory Metals and Hard Materials*, vol. 49, pp. 170-177, 2015.

[33] D. E. Gray, American Institute of physics handbook, 3rd ed., New York: McGraw-Hill, 1972.

[34] H. O. Pierson, Handbook of refractory carbides and nitrides: properties, characteristics, processing and applications, Westwood: William Andrew

Noyes Publishing, 1996.

[35] B. Schultrich and W. Poeβnecker, "Thermal conductivity of cemented carbides," *Journal of Thermal Analysis,* vol. 33, no. 1, pp. 305-310, 1988.

[36] W. F. Gale and T. C. Totemeier, Smithells metals reference book, 8th ed., Waltham, MA: Elsevier, 2004.

[37] A. J. Moses, Practicing scientist's handbook, New York: Van Nostrand Reinhold, 1978.

[38] J. F. Shackelford and W. Alexander, CRC materials and engineering handbook, 3rd ed., Boca Raton: CRC Press, 2000.

[39] S. K. Bhaumik, R. Balasubramaniam, G. S. Upadhyaya and M. L. Vaidya, "Oxidation behaviour of hard and binder phase modified WC-10Co cemented carbides," *Journal of Material Science Letters,* vol. 11, no. 21, pp. 1457-1459, 1992.

[40] P. Kindermann, P. Schlund, H. G. Sockel, M. Herr, W. Heinrich and K. Gorting, "High-temperature fatigue of cemented carbides under cyclic loads," *Refractory Metals and Hard Materials,* vol. 17, no. 1-3, pp. 55-68, 1999.

[41] B. Casas, X. Ramis, M. Anglada, J. Salla and L. Llanes, "Oxidation-induced strength degradation of WC-Co hardmetals," *International Journal of Refractory Metals and Hard Materials,* vol. 19, no. 4-6, pp. 303-309, 2001.

[42] S. N. Basu and V. K. Sarin, "Oxidation behavior of WC-Co," *Materials Science and Engineering A,* vol. 209, no. 1-2, pp. 206-212, 1996.

[43] F. Lofaj and Y. S. Kaganovskii, "Kinetics of WC-Co oxidation accompanied by swelling," *Material Science,* vol. 30, no. 7, pp. 1811-1817, 1995.

[44] V. B. Voitovich, V. V. Sverdel, R. F. Voitovich and E. I. Golovko, "Oxidation of WC-Co, WC-Ni and WC-Co-Ni hard metals in the temperature range 500-800°C," *International Journal of Refractory Metals and Hard Materials*, vol. 14, no. 4, pp. 289-295, 1996.

[45] L. Chen, D. Yi, B. Wang, H. Liu and C. Wu, “Mechanism of the early stages of oxidation of WC–Co cemented carbides,” *Corrosion Science*, vol. 103, pp. 75–87, 2016.

[46] W. Acchar, U. U. Gomes, W. A. Kaysser and J. Goring, “Strength degradation of a tungsten carbide-cobalt composite at elevated temperatures,” *Materials Characterization*, vol. 43, no. 1, pp. 27-32, 1999.

[47] X. Shi, H. Yang, G. Shao, X. Duan and S. Wang, “Oxidation of ultrafine-cemented carbide prepared from nanocrystaline WC-10Co composite powder,” *Ceramics International*, vol. 34, no. 8, pp. 2043-2049, 2008.

[48] T. Iamboliev, S. Valkanov and S. Atanasova, “Microstructure embrittlement of hard metal–steel joint obtained under induction heating diffusion bonding,” *International Journal of Refractory Metals and Hard Materials*, vol. 37, pp. 90-97, 2013.

[49] M. I. Barrena, J. M. Gómez de Salazar and L. Matesanz, “Interfacial microstructure and mechanical strength of WC–Co/90MnCrV8 cold work tool steel diffusion bonded joint with Cu/Ni electroplated interlayer,” *Materials and Design*, vol. 31, no. 7, pp. 3389-3394, 2010.

[50] Y. J. Guo, B. X. Gao, G. W. Liu, T. T. Zhou and G. J. Qiao, “Effect of temperature on the microstructure and bonding strength of partial transient liquid phase bonded WC–Co/40Cr joints using Ti/Ni/Ti interlayers,” *International Journal of Refractory Metals and Hard Materials*, vol. 51, pp. 250-257, 2015.

[51] D. M. Jacobson and G. Humpston, Principles of Brazing, Ohio: ASM International, pp. 106-133, 2005.

[52] A. M. Saeed, Z. H. Hussain, A. B. Ismail and T. Ariga, “The effects of welding parameters on the weldability of different materials using brazing alloy fillers,” *Materials and Design*, vol. 31, no. 7, pp. 3339-3345, 2010.

[53] M. Hasanabadi, A. Shamsipur, H. Najafi Sani, H. Omidvar and S. Sakhaei, “Interfacial microstructure and mechanical properties of tungsten carbide brazed joints using Ag-Cu-Zn+Ni/Mn filler alloy,” *Transactions of Nonferrous Metals Society of China*, vol. 27, no. 12, pp. 2638−2646, 2017.

[54] J. Nowacki and M. Kawiak, “Microstructure and characteristics of high dimension brazed joints of cermets to steel,” *Journal of Manufacturing Science and Engineering,* vol. 37, pp. 448−457, 2009.

[55] W. D. Hawkins, “Review: Physical Chemistry of Surface Films,” *Journal of Polymer Science,* vol. 10, no. 2, pp. 1–413, 1952.

[56] D. Moncayo, G. Buitrago and N. Algecira, “The surface properties of biopolymer-coated fruit: A review,” *Engineering and Research,* vol. 33, no. 3, pp. 11-16, December 2013.

[57] M. M. Schwartz, Brazing, 2nd ed., Ohio: *ASM International*, pp. 30-38, 2003.

[58] B. Cheniti, D. Miroud, R. Badji, D. Allou, T. Csanádi, M. Fides and P. Hvizdoš, “Effect of brazing current on microstructure and mechanical behavior of WC-Co/AISI 1020 steel TIG brazed joint,” *International Journal of Refractory Metals and Hard Materials*, vol. 64, pp. 210-218, 2016.

[59] A. Amirnasiri, N. Parvin and M. Shafieihaghshenas, “Dissimilar diffusion brazing of WC-Co to AISI4145 steel using RBCuZn-D interlayer,” *Journal of Manufacturing Processes,* vol. 28, no. 1, pp. 82-93, 2015.

[60] I. Voiculescu, V. Geanta, H. Binchiciu, D. Iovanas and R. Stefanoiu, “Dissimilar brazed joints between steel and tungsten carbide,” *Materials Science and Engineering,* vol. 209, no. 1, pp. 1-8, 2017.

[61] H. S. Chen, K. Q. Feng, S. F. Wei, J. Xiong, Z. X. Guo and H. Wang, “Microstructure and properties of WC-Co/3Cr13 joints brazed using Ni electroplated interlayer,” *International Journal of Refractory Metals and Hard Materials* , vol. 33, pp. 70-74, 2012.

[62] C. Rhyne, “Factors controlling the strength of brazed joint from Final Report N.R.C. 560,” *The Welding Journal,* vol. 25, no. 7, pp. 599-602, 1946.

[63] J. Hinnuber and C. Hilbes, “Soldering and grinding problems in carbide application,” *Workshop Technology and Mechanical Engineering,* vol. 41, pp. 413-416, 1951.

[64] Z. Mirski and T. Piwowarczyk, “Wettability of hardmetal surfaces

prepared for brazing with various methods," *Archives of Civil and Mechanical Engineering,* vol. 11, no. 2, pp. 411−419, 2011.

[65] W. Feduska, "High temperature brazing alloy - Base metal wetting reactions," *Welding Research Supplement,* vol. 3, pp. 122, 1952.

[66] F. Sui, W. Long, S. Liu, G. Zhang, L. Bao, H. Li and Y. Chen, "Effect of calcium on the microstructure and mechanical properties of brazed joints using Ag-Cu-Zn brazing filler alloy," *Journal of Materials and Design,* vol. 46, pp. 605-608, 2013.

[67] D. Moncayo, G. Buitrago and N. Algecira, "The surface properties of biopolymer-coated fruit: A review," *Journal of Engineering and Research,* vol. 33, no. 3, pp. 11-16, December 2013.

[68] L. Zhang, J. Feng, B. Zhang and X. Jing, "Ag–Cu–Zn alloy for brazing TiC cermet/steel," *Materials Letters*, vol. 59, no. 1, pp. 110-113, 2005.

[69] M. Way, J. Willingham and R. Goodall, "Brazing filler metals," *International Materials Reviews*, 2019.

[70] X. Z. Zhang, G. W. Liu, J. N. Tao, H. C. Shao, H. Fu, T. Z. Pan and G. J. Qiao, "Vacuum brazing of WC-8Co cemented carbides to carbon steel using pure Cu and Ag-28Cu as filler metal," *Journal of Materials Engineering and Perfomance,* vol. 26, no. 2, p. 488-494, 2017.

[71] K. Schröter and H. Wolff, Tool and method of making the same, *U.S. Patent US2019934,* 29 May 1930.

[72] R. G. Gilliland and C. M. Adams, "Improved brazing methods for tungsten carbide tool bits," *Welding Journal,* vol. 50, pp. 267-274, 1971.

[73] N. C. Cole, R. G. Gilliland and G. M Slaughter, "Weldability of tungsten and its alloys," *Welding Journal,* vol. 49, pp. 419-426, 1971.

[74] A. Pieczara, T. Piotrowski, W. Le´sniewski, M. Wawrylak and P. Wieliczko, "The impact of brazing parameters on the strength of a WC/Co-filler metal-steel joint," *Problemy Eksploatacji*, vol. 3, 59-64, 2015.

[75] M. Amelzadeh and S. E. Mirsalehi, "Influence of braze type on microstructure and mechanical behavior of WC-Co/steel dissimilar joints," *Journal of Manufacturing and Processing*, vol. 36, pp. 450-458, 2018.

[76] M. I. Barrena, J. M. G. de Salazar and M. Gómez-Vacas, "Numerical simulation and experimental analysis of vacuum brazing for steel/cermet." *Ceramics International*, vol. 40, pp. 10557-10563, 2014.

[77] L. Pintschovius, B. Schreieck, B. Eigenmann and D. Lohe, "Residual stresses in brazed joints of cemented carbide and steel with complex geometry," ECR5: *Proceedings of the Fifth European Conference on Residual Stresses*, pp. 652-657, 2000.

[78] J. Zhang and L. Y. Jin, "Numerical simulation of residual stress in brazing joint between cemented carbide and steel," *Materials Science and Technology*, vol. 21, no. 12, pp. 1455-1459, 2005.

[79] W.B. Lee, B.D. Kwon and S.B. Jung, "Effects of Cr_3C_2 on the microstructure and mechanical properties of the brazed joints between WC-Co and carbon steel," *International Journal of Refractory Metals and Hard Materials*, vol. 24, no. 3, pp. 215-221, 2006.

[80] L. Zhang, J. Feng, B. Zhang and X. Jing, "Ag–Cu–Zn alloy for brazing TiC cermet/steel," *Materials Letters*, vol. 59, no. 1, pp. 110-113, 2005.

[81] S. Schittny, "Silver – Copper – Zinc," in *Ag-Cu-Zn phase diagram*, H. L. Lukas, Ed., *Landolt-Börnstein*, pp. 156-166, 2006.

[82] Q. Z. Jia, H. T. Zhang, M. Li and H. Dong, "Study of influence of holding time on weld property of hi-frequency induction brazing of polycrystalline diamond compact," *Journal of Dalian University of Technology*, vol. 53, no. 3, pp. 370-375, 2013.

[83] J. Lemus-Ruiz, L. Ceja-Cardenas, J. A. Verduzco and O. Flores, "Joining of tungsten carbide to nickel by direct diffusion bonding and using Cu-Zn alloy," *Journal of Materials Science*, vol. 43, no. 18, pp. 6296-6300, 2008.

[84] Global Engineer Harry, The theory of oxy-acetylene equipment, *Material science*, 2012.

[85] ASTM E92-17, Standard Test Methods for Vickers Hardness and Knoop Hardness of Metallic Materials, *ASTM International*, 2017.

[86] W. D. Callister, Fundamentals of Materials Science and Engineering, 5th ed., *Wiley and Sons Inc.*, 2001.

[87] M. Elsherbiny, R. Hegazy, M. Ibrahim and A. Abuelezz, "The influence

of geometrical tolerances of Vickers indenter on the accuracy of measured hardness," *International Journal of Metrology and Quality Engineering*, vol. 3, no. 1, pp. 1-6, 2012.

[88] [Online]. Available: http://www.dcu.ie/sites/default/files/mechanical_engineering/pdfs/manuals/DensityDeterminationManual.pdf . [Accessed 21 April 2018].

[89] Saxonia Technical Materials, "Saxonia Technical Materials," *BrazeTec*, [Online]. Available: https://www.saxonia-tm.de [Accessed 10 May 2018].

[90] ISO 3327:2009 Hardmetals - Determination of transverse rupture strength, *International Organization for Standardization*, 2009.

[91] ASTM B390-92(2010), Standard practice for evaluating apparent grain size and distribution of cemented tungsten carbides, West Conshohocken, PA: *ASTM International*, 2010.

[92] ISO 4499-4:2016 Hardmetals - Metallographic determination of microstructure - Part 4: Characterisation of porosity, carbon defects and eta-phase content, *International Organization for Standardization*, 2016.

[93] A. E. Newkirk, "The oxidation of tungsten carbide," *American Chemical Society*, vol. 77, no. 17, pp. 4521-4522, 1955.

[94] C. Bagnall, J. Capo and W. J. Moorhead, "Oxidation behavior of tungsten carbide-6% cobalt cemented carbide," *Metallography, Microstructure, Analysis*, vol. 7, pp. 661-679, 2018.

[95] L. Chen, D. Yi, H. Liu and C. Wu, "Mechanism of the early stages of oxidation of WC-Co cemented carbides," *Corrosion Science*, vol. 103, pp. 75-87, 2016.

[96] S. Yaoita, T. Watanabe and T. Sasaki, "Effects of Ni and Co elements in filler alloy metals inAg brazing of cemented carbide," *Materials Research Innovations*, vol. 17, pp. 142-147, 2013.

[97] J. Willingham, "Filler metals and fluxes for brazing tungsten carbide," *Johnson Matthey Metal Joining brochure*, 2008.

9. APPENDICES

Appendix A: Vickers hardness data

This section shows the Vickers hardness test data that was used to calculate the average hardness of the WC-Co cemented carbides and the BrazeTec4900A filler alloy. The hardness data for the cemented carbides is given in Tables A.1 and A.2. Table A3 shows the hardness data of the braze filler alloy. The dimensions of the indentation diagonals are represented by D1 and D2.

Table A.1: Vickers hardness data for the WC-6wt%Co cemented carbides.

Indentation	**D1(µm)**	**D2(µm)**	**HV_{30}**
1	188.1	193.7	1547.4
2	193.0	184.9	1557.1
3	187.6	195.3	1546.9
4	188.2	191.0	1520.8
5	188.5	192.7	1549.3
Average hardness			**1544.30**
Standard deviation			13.77

Table A.2: Vickers hardness data for the WC-10wt%Co cemented carbides.

Indentation	**D1(µm)**	**D2(µm)**	**HV_{30}**
1	180.6	178.2	1681.5
2	179.5	189.7	1672.5
3	180.8	183.4	1645.5
4	179.6	183.2	1674.8
5	181.4	178.0	1678.9
Average hardness			**1670.64**
Standard deviation			14.48

The hardness of the filler alloy was determined using a 10kgf load and a 10 seconds dwell time.

Table A.3: Vickers hardness data for the BrazeTec4900A filler alloy samples.

Indentation	**D1(µm)**	**D2(µm)**	**HV_{10}**
1	320.7	320.8	182.5
2	319.9	319.2	183.1
3	319.9	315.0	183.3
4	324.5	321.4	181.9
5	317.0	322.0	181.5
Average hardness			**182.46**
Standard deviation			0.77

Appendix B: Density data

This appendix provides the density data that was used to calculate the average densities of the WC-Co cemented carbides and the *BrazeTec4900A* filler alloy. The densities were determined using Archimede's principle.

Table B.1: Density data for the WC-6wt%Co cemented carbide samples.

Suspended weight (g)	**Wet weight (g)**	**Dry weight (g)**	**Density (g/m^3)**
10.485	11.236	11.235	14.9700
10.486	11.236	11.235	14.982
10.485	11.236	11.235	14.974
10.486	11.236	11.235	14.974
10.486	11.236	11.235	14.984
Average density (g/m^3)			**14.977**
Standard deviation			**0.126**

Table B.2: Density data for the WC-10wt%Co cemented carbide samples.

Suspended weight (g)	**Wet weight (g)**	**Dry weight (g)**	**Density (g/m^3)**
10.479	11.259	11.258	14.443
10.479	11.259	11.258	14.446
10.479	11.259	11.258	14.433
10.478	11.259	11.258	14.424
10.479	11.259	11.258	14.445
Average density (g/m^3)			**14.439**
Standard deviation			**0.211**

Table B.3: Density data for the BrazeTec4900A samples.

Suspended weight (g)	**Wet weight (g)**	**Dry weight (g)**	**Density (g/m^3)**
4.547	5.308	5.306	8.763
4.548	5.308	5.305	8.826
4.547	5.303	5.302	8.824
4.578	5.305	5.287	8.662
4.547	5.308	5.273	8.925
Average density (g/m^3)			**8.830**
Standard deviation			**0.175**

Appendix C: Elemental distributions across 8 µm interlayer

This appendix provides the individual elemental distributions, obtained by EDX line-scans, across the WC-Co/filler alloy interfaces, with a filler alloy thickness of 8 µm. The EDS line-scan analyses were conducted to understand the inter-diffusion of elements from the filler alloy and the WC-Co cemented carbide rods.

C1. Elemental distributions across 8 µm braze/WC-6wt%Co interface.

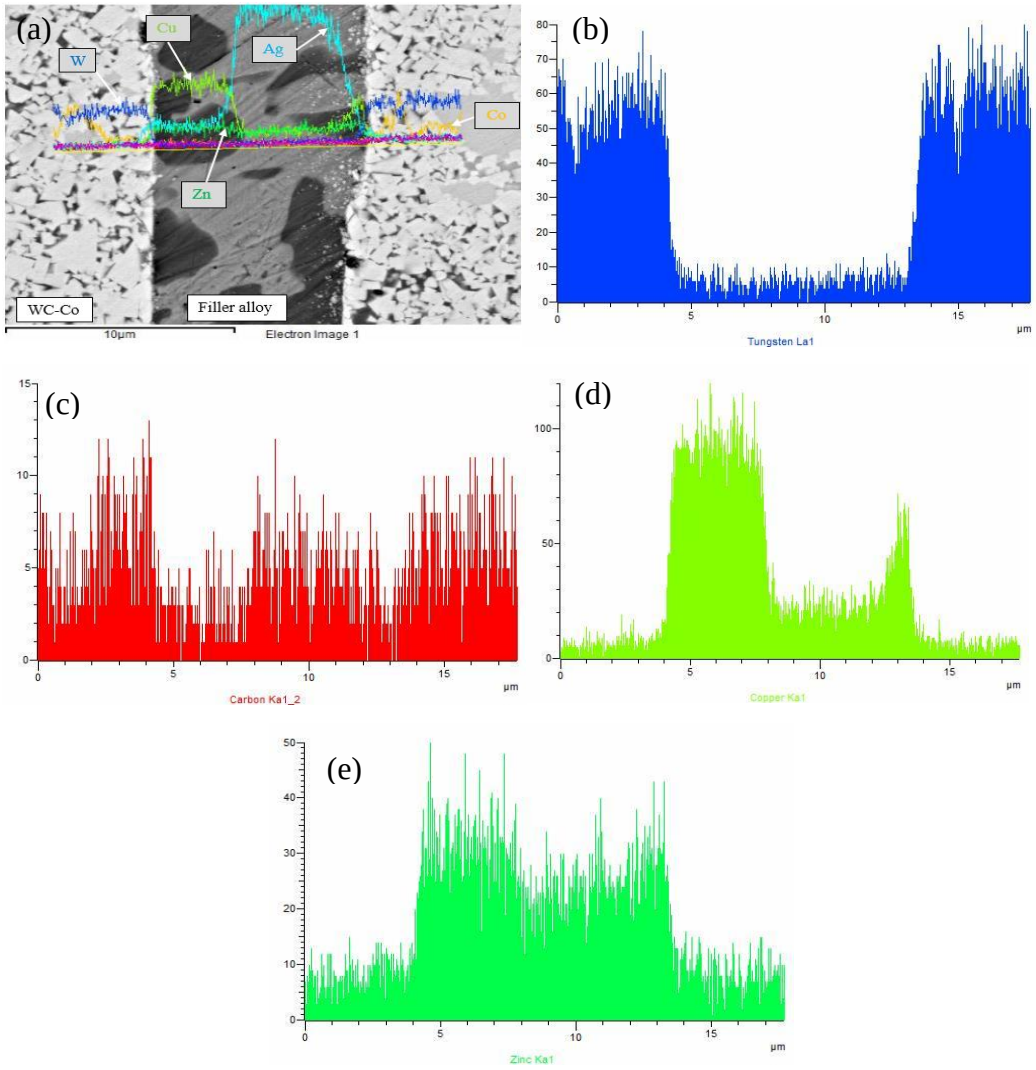

Figure C.1: SEM-EDX line-scanning showing the elemental distribution: (a) overall (b) W, (c) C, (d) Cu and (e) Zn, across the WC-6wt%Co brazed joint with a filler alloy thickness of 8 µm.

C2. Elemental distributions across 8 µm braze/WC-10wt%Co interface.

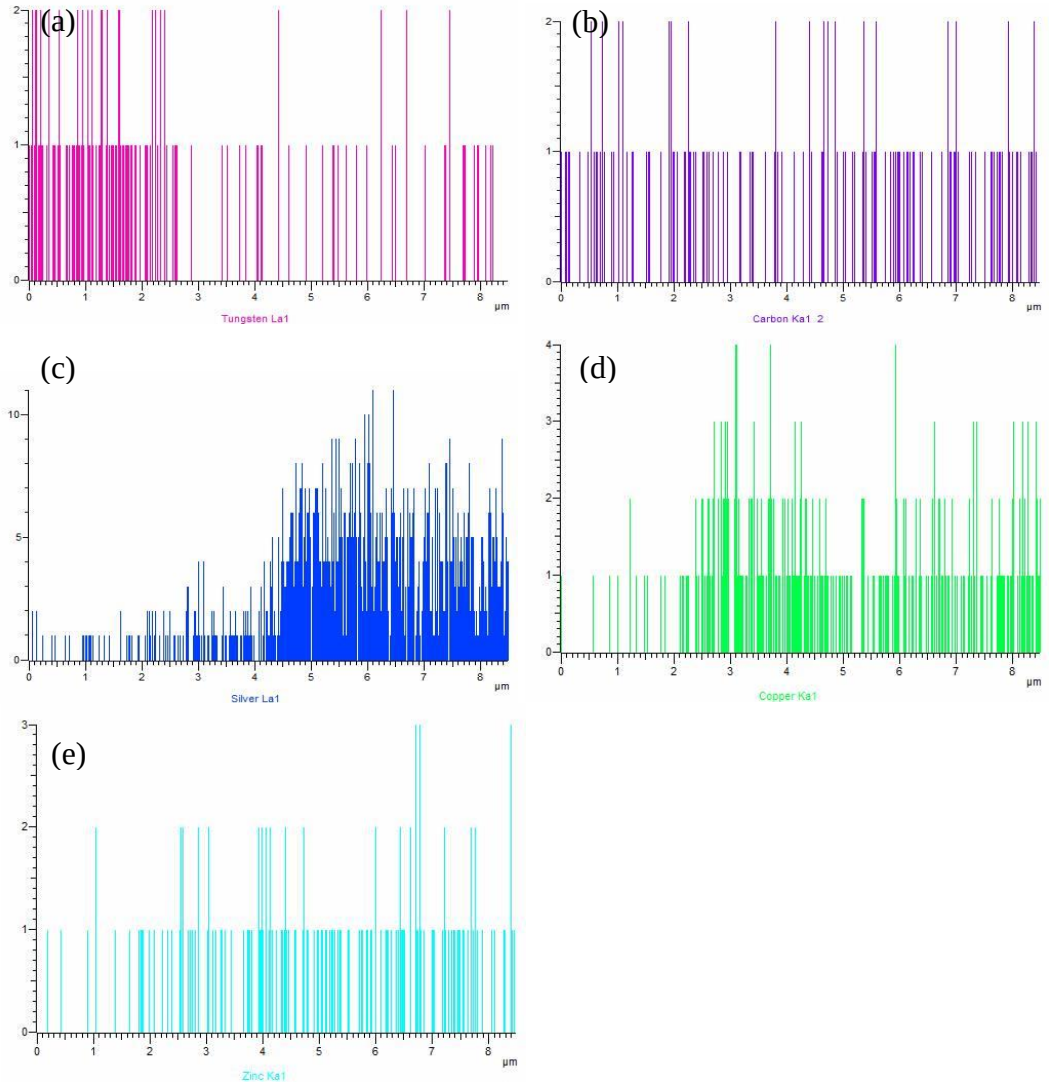

Figure C.2: SEM-EDX line-scanning showing the elemental distribution: (a) overall (b) W, (c) C, (d) Cu and (e) Zn, across the WC-10wt%Co brazed joint with a filler alloy thickness of 8 µm.

Appendix D: Elemental distribution across 24 μm interlayer

This appendix provides the individual elemental distributions across the WC-Co/filler alloy interfaces, with an interlayer of 24 μm in thickness. The EDS line-scan analyses were conducted to understand the inter-diffusion of elements between the filler alloy and the WC-Co cemented carbides.

D1. Elemental distribution across 24 μm braze/WC-6wt%Co interface.

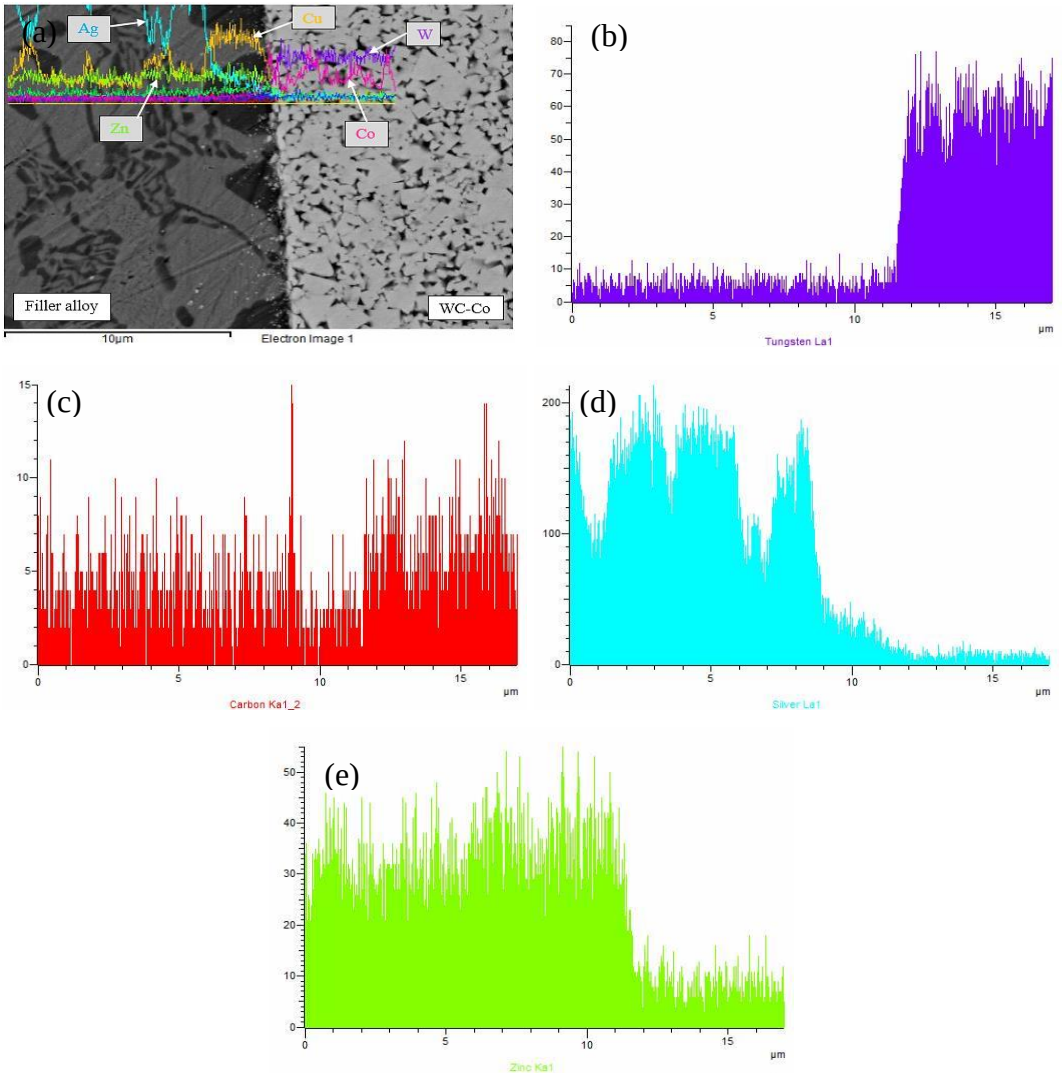

Figure D.1: SEM-EDX line-scanning showing the elemental distribution: (a) overall (b) W, (c) C, (d) Ag and (e) Zn, across the WC-6wt%Co brazed joint with a filler alloy thickness of 24 μm.

D2. Elemental distribution across 24 µm braze/WC-10wt%Co interface.

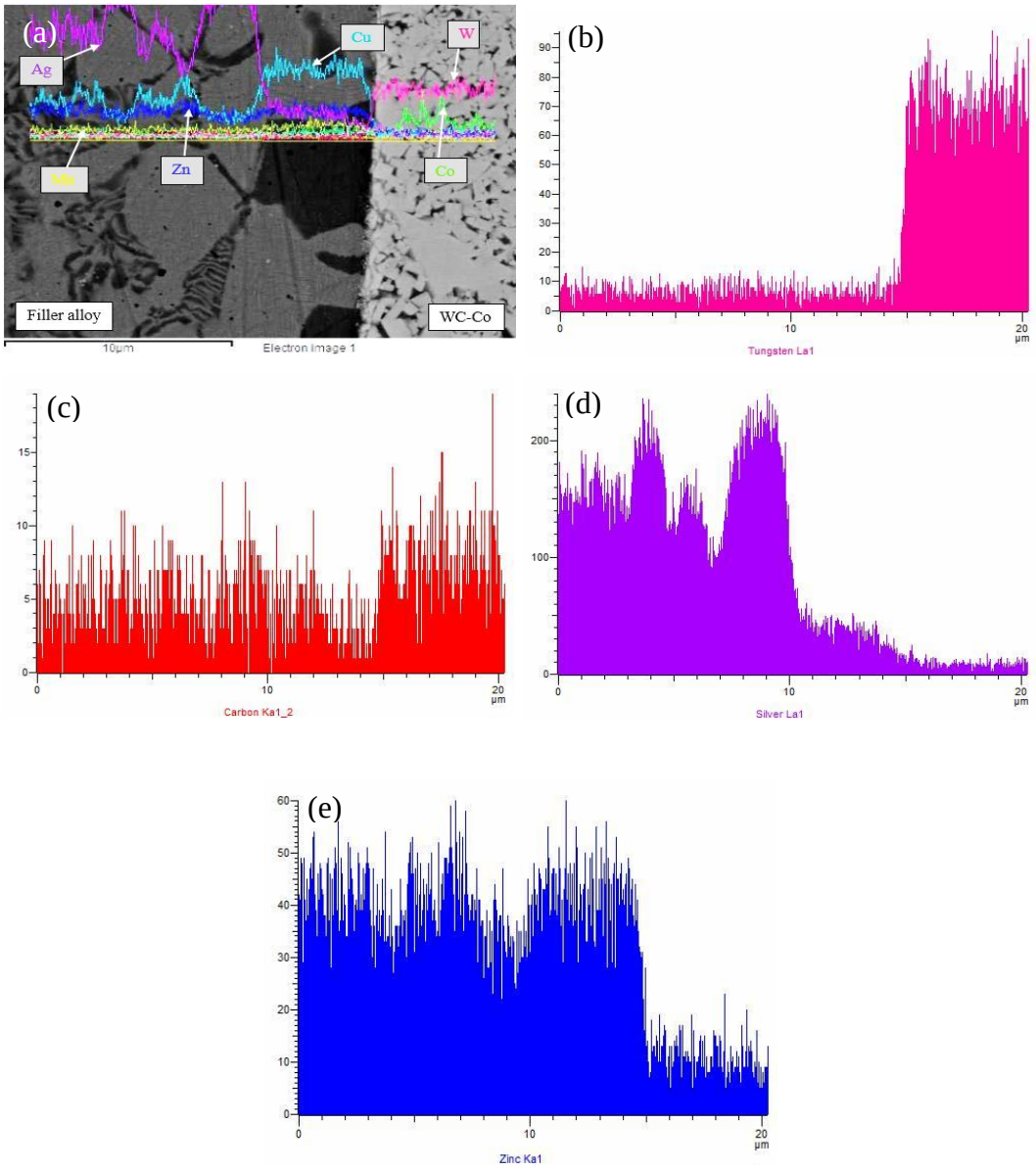

Figure D.2: SEM-EDX line-scanning showing the elemental distribution: (a) overall (b) W, (c) C, (d) Ag and (e) Zn, across the WC-10wt%Co brazed joint with a filler alloy thickness of 24 µm.

Appendix E: Work published

1. N.P Mphasha and D.J Whitefield, The effect of Co content and WC grain size on the thermal oxidation behaviour of WC-Co cemented carbides, 36th Global Conference on Smart Materials and Nanotechnology 2019, (Book of) Abstracts of papers presented at the conference, Journal of Powder Metallurgy & Mining, Vol. 08, pp. 17, Rome, Italy, 18th - 19th November 2019.
2. N.P Mphasha and D.J Whitefield, Interfacial microstructure of WC-6wt%Co torch brazed joints using Ag-based filler alloy, Proceedings of Microscopy Society of Southern Africa (MSSA), Vol. 48, pp. 27, Club Mykonos, Western Cape, South Africa, 1st - 5th December 2019.

Nthape. P. Mphasha, J Journal of Powder Metallurgy & Mining 2019, ISSN: 2168-9806

conferenceseries.com

Joint Event on

25th International conference on MATERIALS SCIENCE AND NANOTECHNOLOGY

&

32nd International Conference on NANOSCIENCE, NANOTECHNOLOGY AND NANOENGINEERING

&

36th Global Conference on SMART MATERIALS AND NANOTECHNOLOGY

&

International conference on SATELLITE AND SPACE COMMUNICATIONS

November 18-19, 2019 | Rome, Italy

The effect of Co content and WC grain size on the thermal oxidation behaviour of WC-Co cemented carbides

Nthape. P. Mphasha
University of the Witwatersrand, South Africa

Thermal oxidation of WC-Co cemented carbides is a key factor in determining the materials' performance during high temperature joining processes as well as establishing an idea of their expected performance in application. The high temperature oxidation behaviour of WC-Co cemented carbides with different Co (6–15wt.%) binder contents and WC grain sizes (sintered size 0.5–5um) were investigated. This investigation explored the feasibility of brazing different WC-Co grades and what effect this thermal process had on the WC grain size and the surface properties of the material. The results show that there was moderate oxidation of the WC-Co samples up to 600°C, and a significant acceleration in oxidation was observed above 600°C. The oxidation behaviour of WC-Co cemented carbides improved with decreasing WC grain size and increasing Co content. After heating the samples to temperatures in the region of 700-750°C, the Vickers hardness and magnetic saturation of the samples decreased, as expected. It was further found that, at all oxidation temperatures, the finer grained alloys preserved their hardness better than coarser grained alloys, at all cobalt contents. It was then determined that the working temperature for brazing WC-Co cemented carbides should be lower than 700°C in air to ensure that the surface of the WC-Co does not substantially oxidise and adversely affect the brazeability of the WC-Co alloys.

Biography

Mr Nthape Mphasha is a second-year MSc Engineering student in the field of carbides and cermets at the University of the Witwatersrand, Johannesburg, South Africa, who focuses on cemented carbides innovation and refurbishment technologies using high-temperature processes. He is affiliated with the DST-NRF Centre of Excellence in Strong Materials hosted by the same university. He has interest in finding novel ways for making economically-viable improvements in hardmetal materials. His current research mainly deals with characterizing the brazing of the different WC-Co grades using different braze alloys. He holds a BSc (with Honours) in Metallurgy and Materials Engineering from the same university.

673306@students.wits.ac.za

INTERFACIAL MICROSTRUCTURE OF WC-6wt.%Co TORCH BRAZED JOINTS USING Ag-BASED FILLER ALLOY

N.P. Mphasha[1,2] and D.J. Whitefield[1,2]

[1]School of Chemical and Metallurgical Engineering, University of the Witwatersrand, Johannesburg, [2]DST-NRF Centre of Excellence in Strong Materials, hosted by University of the Witwatersrand, Johannesburg

In recent years, brazing has received great attention for joining cemented carbides together or to a base material due to its simplicity, high joint strength, good repeatability and low cost[1,2]. Jiang et al.[3] and Hasanabadi et al.[4] obtained sound WC-Co/carbon steel furnace brazed joints using Ag-based filler alloys. Hence, there is potential of brazing at a common interface.

In order to study the effect of filler alloy thickness on the interfacial microstructural evolution, WC-6wt.%Co hardmetals were brazed at a common interface using a Ag-Cu-Zn-Mn-Ni filler alloy. The samples were torch braze under atmospheric conditions at 710 ℃, held for 30 seconds and then cooled in air. Brazed samples were then sectioned across the joint, mounted, ground and polished. Samples were analysed using a Zeiss SEM equipped with energy dispersive X-ray spectroscopy to identify the microstructures and to determine the phase compositions. XRD was conducted using the Bruker D2.

Cross-sectional morphologies of the brazed joints show that metallurgical bonding between the cemented tungsten carbides and the filler alloy were achieved without any voids or cracks. Dark island-like α-Cu (s.s) phases nucleated along the WC-6wt.%Co/filler alloy interfaces (Fig. 1), suggesting the occurrence of metallurgical reaction and diffusion of metallic elements during the brazing process. In addition to the the α-Cu phases, the brazed joint is composed of a light α-Ag (s.s) phase. The micrographs suggest that the nucleation of the α-Cu phases started from the interface towards the center of the interlayer.

Increasing the filler alloy thickness to 18 µm (Fig. 2) promoted the diffusion of metallic elements across the WC-6wt.%Co/filler alloy interface, and decreased the formation of the α-Cu (s.s) phases. Hence, the formation of a leaf-like Ag-Cu-Zn eutectic phase which was confirmed by XRD. From EDS line-scan analysis, across the interfaces, there is a tendency of the α-Cu (s.s) phases rich in Mn and Ni migrating towards the interface due to the good solubility of Ni in Co[4]. This suggested good wettability of the WC-Co surfaces by the filler alloy. Further, the EDS analysis shows that Co diffused from WC-Co base samples into the interlayer. Future research work will include studying the effect of longer holding times and post-braze heat treatment on the properties of the brazed joints.

References:
1. Jacobson, D.M. and Humpston, G. (2005) Principals of Brazing, Ohio, ASM International Materials Park.
2. Saeed, A.M. et al. (2010) Mater. Des. 31(7), 3339.
3. Jiang, C. et al. (2016) Mater. Process. Technol. 229, 562.
4. Hasanabadi, M. et al. (2017) Trans. Nonferrous Met. Soc. China 27, 2638.

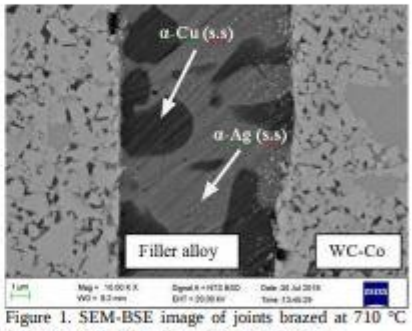

Figure 1. SEM-BSE image of joints brazed at 710 ℃ for 30 sec with filler alloy of 9 µm in thickness.

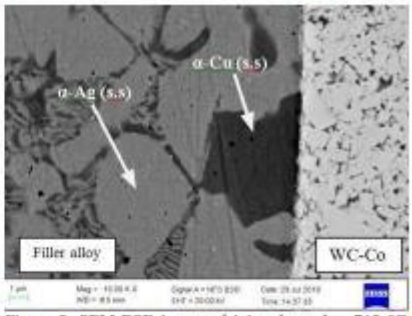

Figure 2. SEM-BSE image of joints brazed at 710 ℃ for 30 sec with filler alloy of 18 µm in thickness.

Corresponding author: 673306@students.wits.ac.za